

Sheffield Hallam University

A charge coupled device based optical tomographic instrumentation system for particle sizing.

IDROAS, Mariani.

Available from the Sheffield Hallam University Research Archive (SHURA) at:

<http://shura.shu.ac.uk/19855/>

A Sheffield Hallam University thesis

This thesis is protected by copyright which belongs to the author.

The content must not be changed in any way or sold commercially in any format or medium without the formal permission of the author.

When referring to this work, full bibliographic details including the author, title, awarding institution and date of the thesis must be given.

Please visit <http://shura.shu.ac.uk/19855/> and <http://shura.shu.ac.uk/information.html> for further details about copyright and re-use permissions.

SHEFFIELD HALLAM UNIVERSITY
LEARNING CENTRE
CITY CAMPUS, POND STREET,
SHEFFIELD S1 1WB.



Fines are charged at 50p per hour

REFERENCE

ProQuest Number: 10697161

All rights reserved

INFORMATION TO ALL USERS

The quality of this reproduction is dependent upon the quality of the copy submitted.

In the unlikely event that the author did not send a complete manuscript and there are missing pages, these will be noted. Also, if material had to be removed, a note will indicate the deletion.



ProQuest 10697161

Published by ProQuest LLC (2017). Copyright of the Dissertation is held by the Author.

All rights reserved.

This work is protected against unauthorized copying under Title 17, United States Code
Microform Edition © ProQuest LLC.

ProQuest LLC.
789 East Eisenhower Parkway
P.O. Box 1346
Ann Arbor, MI 48106 – 1346

**A CHARGE COUPLED DEVICE BASED OPTICAL
TOMOGRAPHIC INSTRUMENTATION SYSTEM
FOR PARTICLE SIZING**

By

Mariani Idroas

A thesis submitted in partial fulfilment of the requirement of the
Sheffield Hallam University for the degree of Doctor of
Philosophy in the School of Engineering

July 2004

ACKNOWLEDGEMENTS

My heartiest thanks are dedicated to my supervisor, Emeritus Professor Bob Green for his tremendous patience and invaluable guidance, who showed that every single part of the project was worth doing. His commitment and encouragement are tremendously superb for the last three years.

I would like to express my appreciation to my Director of Studies, Dr Ken Dutton, for his assistance, comments and suggestions especially in dealing with the Matlab software. To Mr Karl Evans and Dr Alan Goude, thank you for the support and help with the PIC Microcontroller. My deepest appreciation also goes to the technicians in the Workshop, especially Mr B.Didsbury who helped me with the fabrication of the tomography rig. Thank you also to Dr J.A.R Stone from the Mathematics Department for his effort and sincere help in making me understand the mathematical background in the inverse problem.

This success is nothing without blessings from Nasir, Nasyrah, Atiqah, Aqil, and Syafeeqah. Thank you for being so understanding, supporting and helpful especially during those difficult years.

ABSTRACT

This research investigates the use of charge coupled device (abbreviated as CCD) linear image sensors in an optical tomographic instrumentation system used for sizing particles. Four CCD linear image sensors are configured around an octagonal shaped flow pipe for a four projections system. The measurement system is explained and uses four CCD linear image sensors consisting of 2048 pixels with a pixel size of 14 micron by 14 micron. Hence, a high-resolution system is produced.

Three main mathematical models based on the effects due to particles, light sources and diffraction are discussed. The models simulate the actual process in order to understand the limitations of the designed system.

Detailed design of the optical tomography system is described, starting from the fabrication of the 'raybox' of the lighting system, the design of the driving circuit in the detection system, the timing and synchronisation in the triggering system based on the PIC microcontroller and the data acquisition system.

Image reconstruction for a four-projection optical tomography system is also discussed, where a simple optical model is used to relate attenuation due to variations in optical density, $[R]$, within the measurement section. Expressed in matrix form this represents the forward problem in tomography $[S][R]=[M]$. In practice, measurements $[M]$ are used to estimate the optical density distribution by solving the inverse problem $[R]=[S]^{-1}[M]$. Direct inversion of the sensitivity matrix, $[S]$, is not possible and two approximations are considered and compared – the transpose and the pseudo inverse sensitivity matrices.

The designed instrumentation system is calibrated using known test pieces and tested for accuracy, repeatability and consistency among measurements from different projections. The accuracy of the particle size measurement using the system is within 1 pixel i.e. ± 14 micron (the maximum absolute error of 8.5 micron), with the maximum percentage error of 1.46%. Moreover, the system has a good repeatability and consistency – within 1.25 pixel. The range of particle size that has been tested using the system is between 0.18 mm up to 11 mm diameter. A spherical shaped and an irregular shaped particle are tested on the designed system to complete analysis of the overall performance of the system.

This thesis is concluded with achievements of objectives of the research, followed with suggestions for future work.

TABLE OF CONTENTS

ACKNOWLEDGEMENTS	i
ABSTRACT	ii
LIST OF FIGURES	vi
LIST OF TABLES	v
CHAPTER 1: INTRODUCTION	
1.1 Background	1
1.2 Aim of project	3
1.3 Objectives of project	3
1.4 Organisation of the thesis	4
CHAPTER 2: OVERVIEW OF PARTICLE CHARACTERISATION	
2.1 Introduction	5
2.2 Literature review on particle characterisation	6
2.3 Particle characterisation by means of tomographic techniques	12
2.4 Discussions	13
CHAPTER 3: MATHEMATICAL MODELLING	
3.1 The optical system	14
3.2 Models on the effects due to particles	15
3.2.1 When there is no particle	18
3.2.2 With a circular/spherical particle	22
3.2.3 Modelling for the image reconstruction process	30
3.3 Effects due to light sources	31
3.4 Effects due to diffraction	35
3.4.1 Diffraction at a straight edge	37
3.4.2 Diffraction by a circular obstacle	39
3.4.3 Diffraction in the optical tomography system	40
3.5 The scan rate	43
3.6 Discussions	45

CHAPTER 4: DESIGN OF THE OPTICAL TOMOGRAPHY SYSTEM

4.1 Overview of the system	46
4.2 Experimental set-up	49
4.2.1 The illumination system	51
4.2.2 The CCD detection	55
4.2.2.1 Driver for the CCD linear image sensor	56
4.2.2.2 Hardware of the CCD driver	58
4.2.2.3 Triggering circuit: PIC16F84	61
4.3 Switching the laser module	65
4.4 Discussions	66

CHAPTER 5: OPTICAL TOMOGRAPHIC IMAGE RECONSTRUCTION

5.1 Introduction	67
5.2 Image reconstruction process	70
5.2.1 Forward problem	71
5.2.2 Inverse problem	76
5.2.2.1 3x3 array of pixels (three projections)	78
5.2.2.2 7x7 array of pixels	80
5.2.2.3 21x21 array of pixels	82
5.2.2.4 101x101 array of pixels	83
5.3 Discussions	85

CHAPTER 6: EXPERIMENTAL RESULTS

6.1 The calibration process	86
6.1.1 Accuracy	87
6.1.2 Repeatability	90
6.1.3 Repeatability in projections reading (consistency)	93
6.1.4 The tomographic images of the test pieces	94
6.2 The measurements of a 3-mm sphere bead	95
6.2.1 The tomographic images of the bead	99
6.2.2 Filtered tomographic images of the bead	104
6.3 The measurements of an irregular shaped nut	106
6.3.1 The tomographic images of the nut	113
6.3.2 Filtered tomographic images of the nut	118

6.4 Analysis of results on tomographic reconstructed images	120
6.4.1 Without filtering	120
6.4.2 With filtering	121
6.5 Discussions	122

CHAPTER 7: CONCLUSION AND RECOMMENDATIONS FOR FUTURE WORK

7.1 Conclusions	123
7.2 Research objectives	124
7.3 Suggestions for future work	127
7.3.1 Improvements of the existing system	127
7.3.2 Future applications of the system	129

REFERENCES	130
-------------------	------------

APPENDIX A

APPENDIX B

APPENDIX C

APPENDIX D

CHAPTER 1

INTRODUCTION

1.1 Background

Industrial processes are often controlled using process measurements at one or more points. The amount of information contained in such measurements is often minimal, and in some cases (multiphase flow) there are no adequate sensors [Scott DM, 1995]. To understand better certain chemical processes, a more sophisticated approach is needed. Process tomography is a means of visualising the internal behaviour of industrial processes, where tomographic images provide valuable information about the process for assessment of equipment designs and on-line monitoring [Peyton AJ *et al*, 1996].

There are several modalities used in process tomography such as electrical (impedance, capacitance, inductance), radiation (optical, x-ray, positron electromagnetic (PET), magnetic resonance) and acoustic (ultrasonic) [Beck MS and Williams RA, 1996]. Electrical tomography has relatively poor spatial resolution of about 10% of diameter of cross section [Xie CG, 1993]. The X-ray computed tomography method is well known, but specific safety procedures need to be followed by the operator. PET needs operator intervention and radioactive particles. Ultrasonic tomography is complex to use due to spurious reflections and diffraction effects and may therefore require a high degree of engineering design [Beck MS and Williams RA, 1995].

Optical techniques are desirable because of their inherent safety (the transducer does not require direct physical contact with the measurand), high efficiency [Kostov Y and Rao G, 2000] and could improve manufacturing in the chemical industries [Leutwyler K, 1994]. For processes handling transparent fluids and where optical access is possible, optical techniques can provide high-resolution images [Beck MS and Williams RA, 1995] i.e. 1% spatial resolution [Abdul Rahim R, 1996].

Particle sizing is very important for many industrial processes and has led to much research. Typical problems relate to pulverised coal for combustion and liquid fuels, spray characterisations, analysis and control of particulate emissions, industrial process control, manufacture of metallic powders and the production of pharmaceuticals [Black DL *et al* 1996]. The following diagram summarises the major techniques used in particle-size measurements [Snowsill WL, 1995].

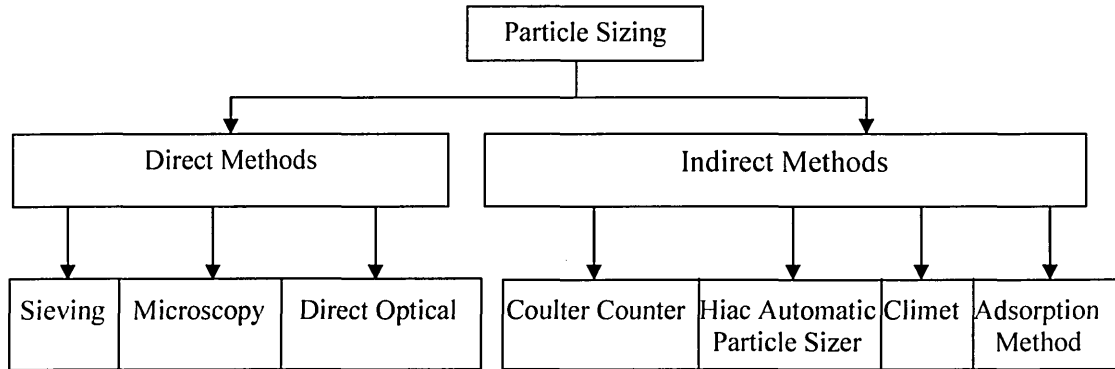


Figure 1.1. A block diagram of particle sizing techniques.

The majority of the techniques are off-line, with direct optical providing the only truly on-line measurement [Black DL *et al*, 1996]. The existing on-line optical methods use Fraunhofer diffraction to determine positions or angles of optical emission spectra generally within a limited measurement volume, which sets a limit on the quality of images produced by optical systems [Elliot KH and Mayhew CA, 1998]. Morikita *et al* (1994) used the Fraunhofer response curve (size-intensity relationship) to measure equivalent diameter of non-spherical particles ranging from 20 - 200 μm ; both these methods are inferential.

Horbury *et al* (1995b) investigated transparent slurries with particle sizing and flow profiles using optical fibres. An optical tomography system that uses optical fibre bundles has problems in ensuring every fibre has similar optical characteristics [Ramli N *et al*, 1999]. Thus, a system based on CCD devices is proposed which may provide very high resolution (better than 1%), on-line measurement over the full measurement cross section and high speed data acquisition based on proprietary items [Coufal H, 1995].

1.2 Aim of project

Particle characterisation, mainly particle size, is of great importance in many chemical processes. The aim of this project is to investigate the feasibility of designing an on-line optical tomographic instrumentation system for measuring particle size and to reconstruct an image of the particle of interest based on the four projections of the system in lightly loaded slurry conveyors i.e. solid/liquid flows.

1.3 Objectives of the project

1. Investigate the use of a CCD linear image sensor to obtain measurements in solid/liquid flow for a range of particle sizes from 10.5 mm down to 400 micron.
2. Model the system in order to understand the effects due to particle size and transmissivity, light sources and diffraction.
3. Design a light projection system based on the models in Objective 2.
4. Investigate the use of four CCD linear image sensors that will be configured in four projections around the pipe.
5. Design and build a complete four-projection measurement system.
6. Calibrate the four projections instrumentation system for measuring particle sizes using known diameters between 400 micron and 10.5 mm.
7. Investigate the range of particle size which can be measured by the system and the limitations imposed by the instrumentation system.
8. Design, implement and test a linear back projection algorithm based on four projections to produce tomographic images. Two methods of solving the inverse problem based on transpose and pseudo inverse matrices are used and compared.
9. Test the four projections instrumentation system for measuring a spherical particle and an irregular shaped particle.
10. Discuss the system and the results, and make suggestions for future work.

1.4 Organisation of the thesis

Chapter 1 of this thesis presents briefly the background of process tomography and particle sizing in the industry. The aim and the objectives of the research are defined, followed by the outline of the thesis.

Chapter 2 discusses an overview of particle sizing by literature review of other techniques used in particle size measurement. The relevance of using optical tomography in sizing particles concludes the chapter.

Chapter 3 describes the mathematical models of the prototype system based on three main effects – due to particle, light sources and diffraction.

Chapter 4 describes in detail the optical tomographic instrumentation system. The experimental set-up consists of the illumination system, the test cell, the CCD detection and the data acquisition system; all are discussed in depth.

Chapter 5 presents the forward and inverse problems in tomographic image reconstruction. Two image reconstruction methods are used – transpose and pseudo inverse. Optical tomographic reconstructed images are presented based on simulated data. This chapter concludes by discussing the significance of using transpose and psuedo inverse in the image reconstruction process.

Chapter 6 presents the experimental results based on the calibration measurement and the diameter measurement. The tomographic images based on the measured data are presented, followed by the analysis of the result and discussion.

Chapter 7 presents the overall conclusions and the recommendations for future work.

CHAPTER 2

OVERVIEW OF PARTICLE CHARACTERISATION

2.1 Introduction

Particle characterisation plays an important role in industrial applications, especially particle-size measurements. Examples include combustion of pulverised coal and liquid fuels, spray characterisations, analysis and control of particulate emissions, industrial process control, manufacture of metallic powders, and the production of pharmaceuticals [Black DL *et al*, 1996]. Demands for high efficiency in processes whilst maintaining the necessary product quality can be met by using on-line measurements [Lech M *et al*, 1998]. Table 2.1 shows some examples of industrial applications, which use particle-sizing technology.

Table 2.1. Applications of particle-sizing technology [Black DL *et al*, 1996].

Uses of particle-size analysis	Applications area
Combustion	Size and velocity measurements
Sprays	Characterisations and descriptions of nozzles
Medicine / Pharmaceuticals	Control of manufacturing processes
Paints	Control of pigment size distribution
Metallic powders	Control of manufacturing processes
Agriculture	Control of pesticide application
Pollution control	Monitoring and analysis of emissions
Foods and consumer products	Control of taste and texture

There are many techniques and methods involved in particle-size measurements, in response to different situations encountered in sizing particles [Black DL *et al*, 1996]. The next sections focus on optically based systems used in particle-size measurement, including an optical tomography system.

2.2 Literature review on particle characterisation

There are three important factors in particle characterisation – composition, size and shape. Particle composition will determine properties such as density and conductivity. Particle size is important as it affects the surface area, volume or flow rate of the particle. Particle shape can be in a form of regular (such as a sphere) or irregular shape.

On an industrial scale, large quantities of particles are handled. In place of particle size, one needs to know the distribution of particle sizes in the mixture and be able to define a mean size, which in some way represents the behaviour of the particulate mass as a whole (Coulson JM and Richardson JF, 1991).

The simplest shape of a particle is a sphere as it is symmetrical i.e. it has the same size when viewed from different directions. The size of an irregular shaped particle is usually defined in terms of the size of an equivalent sphere (Coulson JM and Richardson JF, 1991). Some of the important sizes of equivalent spheres are as follows:

- a) Sphere of the same volume as the particle.
- b) Sphere of the same surface area as the particle.
- c) Sphere of the same surface area per unit volume as the particle.
- d) Sphere of the same area as the particle when projected on to a plane perpendicular to its direction of motion.
- e) Sphere of the same projected area as the particle, as viewed from above, when lying in its position of maximum stability (e.g. on microscope slide).
- f) Sphere which will just pass through the same size of square aperture as the particle (as on a screen).
- g) Sphere with the same settling velocity as the particle in a specified fluid.

Figure 2.1 shows a summary of methods used in the particle-size measurements. The methods can be divided into two basic methods: direct and indirect methods.

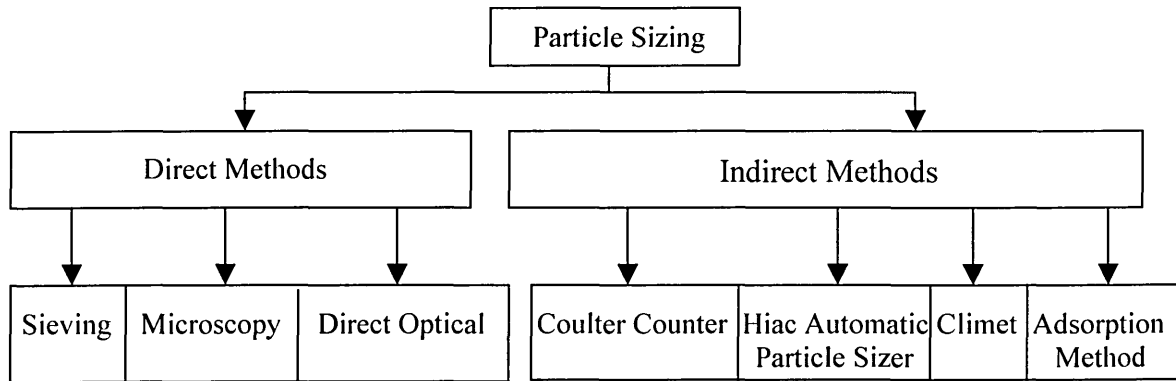


Figure 2.1. Methods used in particle-size measurements.

The size of the particle using the direct methods is obtained straight away whilst in the indirect methods the measured value is inferred by means of another parameter.

1. Sieving

Sieving is a technique where the particles are sorted into categories on the basis of size alone, independently of their other properties such as density and surface properties. It is considered as the simplest and most widely used method of particle sizing. It is used for particle sizes ranging from 20 micron to 125 mm [Allen T, 1990].

A basic sieve is made of woven material, with punched plate or wire mesh. Sieves are often referred to by their mesh size, which is the number of wires per linear inch. For particles smaller than 20micron, micromesh sieves are used, whereas the punched plate sieves are used for larger particles.

Sieving may be done off line to determine the particle size distribution by using a set of sieves. It may also be used on-line to ensure larger particles do not progress further in the manufacturing process. Sieves may also be used to remove unwanted small particles such as dust.

2. Microscopy

Microscopic analysis is performed on small particles ranging from 1 to 100 micron. It is an absolute method of particle size analysis since it is the only method in which the individual particles are observed and measured [Allen T, 1990]. This technique allows an examination of the shape and size of particles with sensitivity far greater than any other technique.

Optical microscopy is used for analysing particles down to 0.8 micron in size. For smaller particles it is necessary to use electron microscopy such as Transmission Electron Microscopy (TEM).

Measurements based on this technique are carried out on minute quantities, and hence sampling techniques and sample preparation should be handled carefully. Microscopy is usually an off-line monitoring technique.

3. Direct Optical

The direct optical method is based on light scattering, where information on particle size is obtained when a beam of radiation is interrupted by the presence of a particle. Light scattering methods are most effective for particles of the same order of size as the wavelength of the incident radiation (Mie theory). However, the Rayleigh scattering model is used for very small particles (approximately less than a twentieth of the wavelength of light), where the scattered-light intensity is proportional to the square of the particle volume. In the case of particles larger than the wavelength of the incident radiation, the contribution of the radiation refracted within the particle diminishes in comparison to the radiation diffracted external to the particle. For particle size greater than four or five times the wavelength of light, the Mie theory reduces to the Fraunhofer theory and the expression for the scattered intensity is the one for diffraction by a circular disc [Allen T, 1990].

A typical, commercial system uses a laser to interrogate a section of the flow (Figure 2.2). The area where the beam is focused is monitored and the second lens produces the spatial Fourier transform of the light. A range of off axis sensors detect the spatial components; the nearer the axis, the larger the component. The system is on-line, but only senses a small (sample) volume of the flow.

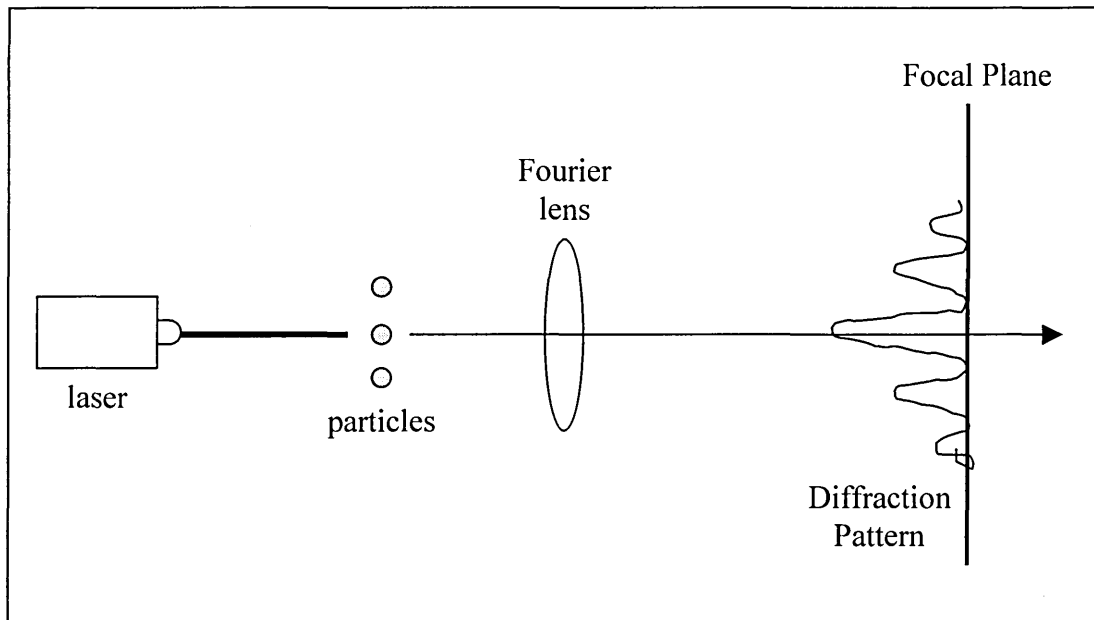


Figure 2.2. Particles diffracted light scattering pattern on the focal plane.

4. Coulter counter

This is a continuous sampling process. Fluid, containing particles is withdrawn from the main flow, sampled and then generally returned downstream into the main flow.

This is a method of determining the number and size of particles suspended in an electrolyte, by causing them to pass through a small orifice on either side of which is implanted an electrode [Allen T, 1990]. There will be changes in electrical impedance as the particles pass through the orifice and generate voltage pulses. This voltage pulse has an amplitude proportional to the volume of the particle. The pulse is then amplified, sized and counted.

This method is suitable for sizing particles greater than 0.6micron in diameter.

5. Hiac particle sizer

Hiac is a stream-scanning method, which is usually applied to a dilute system. It is also known as an optical counter, and preferred to the Coulter counter due to the fact that it can handle higher volume, does not suffer aperture blockage, is more readily adapted for on-line analysis and does not need any electrolytic carrier.

In this method, the particle is forced through a sensor containing a small cell with windows on opposite sides. A collimated beam of light from a high intensity source is directed through the stream of liquid on to a sensor. The particles pass through the volume and produce pulses proportional to their average projected area, where these pulses are scaled and counted. Particle sizes ranging from 2 micron up to 1000 micron can be measured using this method.

6. Climet

The climet method is used for liquid or air-borne particle counting. Here, the incident radiation strikes the sample volume and the scattered light is picked up by a photomultiplier. It can be operated using a white light source and a fibre-optic bundle for light collimation. However, lasers have generally replaced the white light source.

The amount of light scattered by particles smaller than the wavelength of the incident light is proportional to their volume. However, for larger particles the amount of scattered light is related to the projected surface area of the particle in the light beam. This method manages to count particles (drawn from a syringe) ranging from 2 micron to 200 micron, with flow rates ranging from 120-750 ml/minute. The particle concentrations are up to 100 ml [Allen T, 1990].

7. Adsorption method

This method is based on the surface area measurement of a particle. An example of an adsorption method is gas adsorption. In gas adsorption, the gas molecules will impinge upon a solid and reside upon its surface for a finite time when the solid is exposed to a gas. The amount adsorbed depends on the nature of the solid (adsorbent), the gas (adsorbate) and the pressure at which adsorption takes place. The amount of gas adsorbed is calculated by determining the increase in weight of the solid (gravimetric method) or the amount of gas removed from the system due to adsorption (volumetric method) [Allen T, 1990].

2.3 Particle characterisation by means of tomographic techniques

Current activity in the development of new investigative techniques has focused on the use of tomography to provide cross-sectional (*tomo* is *slice* in Greek) and three-dimensional images of internal multi-phase flow behaviour in actual process flow [Simons SJR, 1994]. The tomographic system consists of an array of sensors, a signal conditioning and data acquisition system, and a reconstruction and display system [Green RG and Thorn R, 1998], where the collected data are processed using a reconstruction algorithm to provide an image [Xie CG *et al*, 1989]. A brief review of the application of process tomography in solid/liquid flow is discussed.

Morton and Simons (1994) used X-ray microtomography to capture images of 1 mm up to 10 mm cylinders, but the technique is not generally suited for on-line monitoring of industrial processes. This is due to the fact that microtomographic imaging is not capable of resolving rapid changes in dynamic processes. McKee *et al* (1994) used Positron Emission Tomography (PET) in a solid-liquid (sand-water) mixing model, fitted with four planes of sixteen electrodes. The sand sizes used included 150-210 μm , 425-500 μm and 600-710 μm . The developed PET system has a fast dynamic response but provides images of low resolution. Williams *et al* (1995) investigated the industrial application of capacitance tomography in monitoring solids discharged from a hopper - a study of the distribution of particulate solids within a chute in an operating plant. A transducer based on a 12-electrode capacitance tomography system had been utilised where solid particles with diameters in the range of 14-20 μm , with a density 2400 kg/m^3 were conveyed in the chute. However, the sensor system used can only monitor fine solids for concentration values larger than 5%.

Some research has been done using optical tomographic techniques such as optical diffraction tomography (ODT). Wedberg and Stamnes (1995) used ODT to generate cross-sectional, complex refractive index distributions of weakly scattering cylindrical objects (fibres). The object diameters ranged from about 7 μm to 120 μm .

Abdul Rahim (1996) used optical fibre sensors in a tomographic measurement system designed to measure the flow of dry solids (sand and 3 mm plastic chips) in a gravity drop conveyors. The measurement system used 32 optical fibre transmitter-receiver pairs (two projection system). The output signal of the receiver voltage increased with

increased solid flow rate. The result showed that the majority of particles had a relatively constant velocity when determined using cross-correlation technique – 4.8 meter/second for sand and 4.7 meter/second for plastic chips.

Ibrahim (1999) used the optical tomography system based on Abdul Rahim's measurement system (1995) to study the concentration and velocity profiles of gas bubbles in vertical hydraulic flow rig. However, Ibrahim (1999) used a combination of two orthogonal (8x8 array) and two rectilinear (11x11 array) projections. Thus 38 optical fibre sensors are used in one plane. Two planes were placed axially along the flow pipe for the determination of velocity using cross-correlation technique. The system was capable of measuring the concentration of small bubbles (with diameter of 1-10 mm) in water with volumetric flow rates of up to 1 litre/minute, and the concentration of large bubbles (with diameter of 15-20 mm) in water with the volumetric flow rates of up to 3 litre/minute.

An optical tomography system based on optical fibres was developed by Horbury *et al* (1995a) aimed at providing information on particle size, where three projections are used with each consisting of 16 or 32 views. Three projections are used to reduce the effects of shadowing during reconstruction, with three ranges of bead size - 100 - 150 μm , 150 - 300 μm and 425 - 600 μm . The optical signals were converted into electrical signals. Spectrum analysis was applied to the electrical signals and related to particle size distribution.

From the above literature, it can be concluded that the developed systems did not really measure the size of a particle. The techniques concentrated more on how different types or different sizes of particles affected the particle distribution, concentration and velocity. Some of the techniques have low-resolution outputs, for example optical tomography using optical fibres and electrical impedance tomography. Meanwhile, in other non-tomographic techniques, the measured size of the particle is based on the sampling measurements, which does not represent the full volume of the process flow.

This thesis presents a four projection, optical tomography system using charge coupled devices (CCD) as detectors. The CCD based optical tomography system has high definition sensors. Each of the four devices has 2048 sensors, with sensor size of 0.014

mm by 0.014 mm. Moreover, the system is capable of sizing the whole volume of process flow and the technique is non-intrusive.

2.4 Discussions

Most of the particle-size measuring techniques are off-line, with direct optical providing the only truly on-line measurement [Black DL *et al*, 1996]. Some of the techniques, such as a Coulter counter, have on-line sampling measurements where part of the flow is sampled in real-time or is deviated from the process flow for on-line measurement of the sample. However, measuring particle size on-line by means of an optical tomography system will cover the whole volume of the process flow instead of some sampled flow which might not represent the actual behaviour of the process flow.

Many techniques used for determining particle size are intrusive in nature and can cause unknown variations in the flow field [Black DL *et al*, 1996]. However, optical tomography is based on non-intrusive techniques where the sensors are placed surrounding the process or the flow pipe. One possible difficulty encountered in applying a non-intrusive optical technique lies in the need for optical access to the measurement environment.

“Seeing is believing – what we mean by seeing, however, has changed. One of the best ways to capture these images is to use tomography, which allows us to see the inside of an object without inserting probes or sensors.” [West R, 2003]

CHAPTER 3

MATHEMATICAL MODELLING

3.1 The optical system

Mathematical modelling is an important tool in simulating a system. It can predict the output of a system with known conditions. In addition, the model enables the user to understand the output trends or behaviour. Three types of mathematical model are developed in this project for investigating the effects due to particles, the effects due to light sources and the effects due to diffraction on the optical tomography system.

The complete optical tomography system consists of a lighting system, the measurement section, the sensor system, the data acquisition system, the PIC microcontroller system and image information. Figure 3.1 shows an overview of the system.

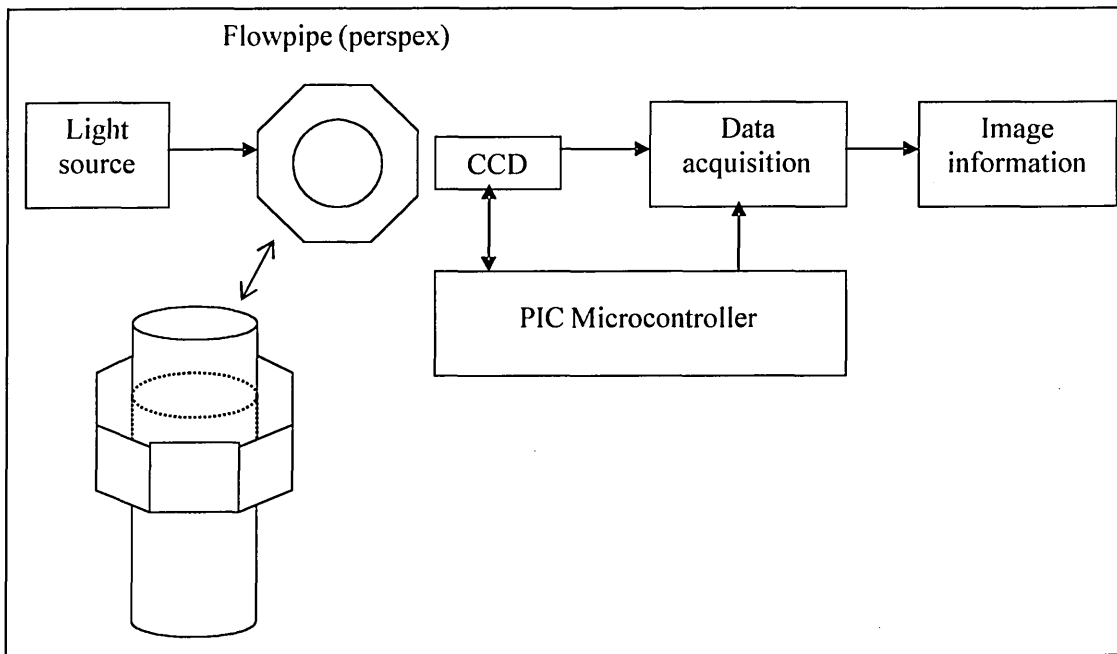


Figure 3.1. A block diagram of the optical tomography system.

A well-collimated beam of light is passed through the measurement section, past the object to be measured. For test and calibration purposes, ground bar of known diameter is used. The detection system is the sensing component in the optical tomography system. The standard object (ground bar of known diameter) is sensed using a charge coupled device (CCD) linear image sensor. The output of the CCD linear image sensor is then acquired by the data acquisition system.

3.2 Models on the effects due to particles

There are three effects occurring with light as it passes through a translucent particle – light attenuation due to absorption, reflectance and scattering (neglected due to its complex mathematical model and the fact that the particle size of interest is much greater than the wavelength of the incident light). Mathematical models are constructed to simulate the behaviour of light and aid understanding of the limitations of the system. The models also predict the expected results, which can be compared later with the experimental results in order to justify the performance of the developed system. The models are based on glass spheres conveyed by water.

a. Light attenuation

Light is attenuated in passing through a medium due to absorption, where the output light intensity is exponentially attenuated by the object density along the optical path (according to Beer-Lambert Law).

$$I_{out} = I_{in} e^{-\alpha x} \quad (3.1)$$

$$\ln\left(\frac{I_{in}}{I_{out}}\right) = \alpha x \quad (3.2)$$

where α is the linear attenuation coefficient and x is the distance the light traversed. The natural logarithm of the ratio of the incident intensity to the transmitted intensity is equal to the line integral or ray sum of the distribution of linear attenuation coefficients within the object along the path.

b. Light reflectance

Energy losses occur when light is passing through an interface in the form of light reflectance. The ratio of light reflected at each surface is called reflectance, which is represented by a symbol R [Hecht E, 1987].

$$R = \left[\frac{(n_t - n_i)}{(n_t + n_i)} \right]^2 \quad (3.3)$$

where n_t : transmitted refractive index

n_i : incidence refractive index

For air-perspex interface:

$$R_{air/perspex} = \left[\frac{1.5 - 1}{1.5 + 1} \right]^2 = 0.04 \text{ or } 4\% \quad (3.4)$$

For water-glass interface:

$$R_{water/glass} = \left[\frac{1.5 - 1.33}{1.5 + 1.33} \right]^2 = 0.0036 \text{ or } 0.36\% \quad (3.5)$$

The value of R above represents the minimum surface reflection and occurs at plane surfaces where the light ray is normal to the surface. As the angle of incidence of the incident ray increases, a greater fraction of the light is reflected. These reflection effects reduce the amount of light transmitted through the particle (Section 3.2.2).

Figure 3.2 shows a 1 mm collimated beam of light striking a spherical particle in the measurement section (top view). The spherical particle is translucent and assumed to behave like a thick lens [Jenkins FA and White HE, 1957]. The side view of the overall measurement section is shown in Figure 3.3.

Three models for the light passing through the sensing volume are now presented.

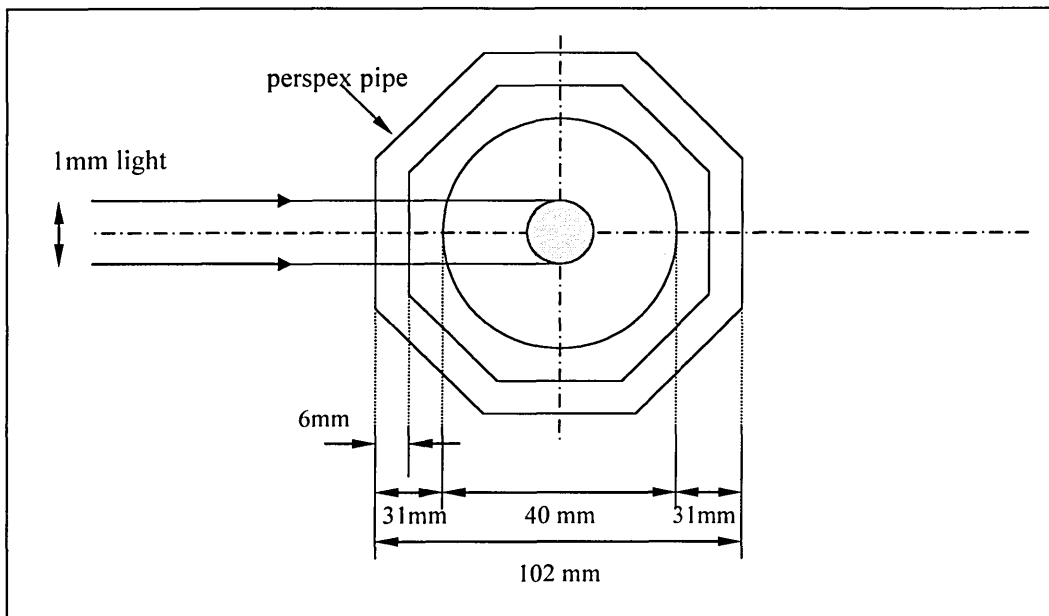


Figure 3.2. Top view of a particle in the middle of the pipe.

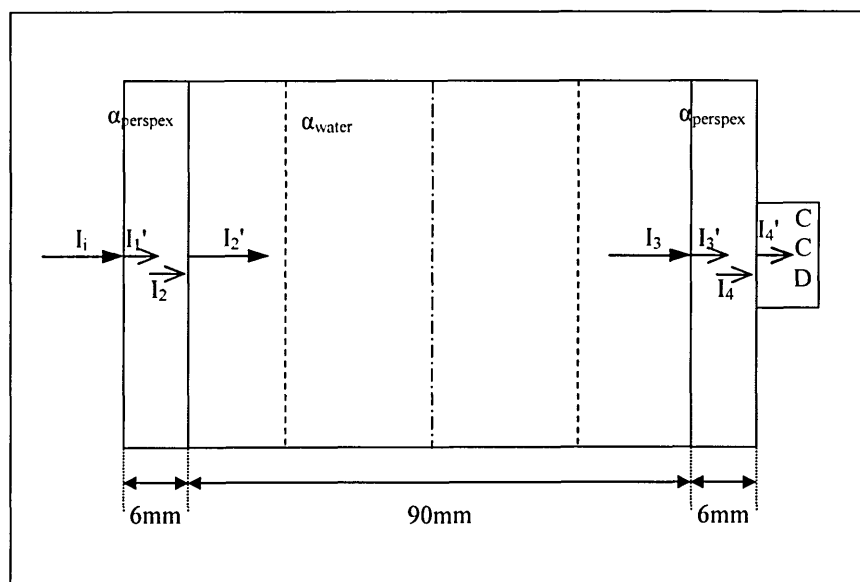


Figure 3.3. Side view of the overall measurement section.

3.2.1 When there is no particle

A CCD linear image sensor detects the shadow an object casts on the sensor when a collimated light is directed directly to the CCD linear image sensor. The light intensity is converted to voltage where the voltage is related to the amount of light falling on the CCD sensor. When there is no obstruction in the flow pipe, the saturation voltage is obtained (V_{sat}). In all cases, the reflection at the front surface of the CCD linear image sensor is neglected. Figure 3.3 shows the layout of the flow pipe when there is no obstruction.

The incoming light intensity (I_i) is reduced at the first surface of the perspex due to the reflection at the air/perspex interface.

$$I_1' = I_i - I_{reflection1} = I_i - \left[I_i \left(\frac{n_{perspex} - n_{air}}{n_{perspex} + n_{air}} \right)^2 \right] \quad (3.6)$$

$$I_1' = I_i - \left[I_i \left(\frac{1.5 - 1}{1.5 + 1} \right)^2 \right] = 0.96I_i \quad (3.7)$$

The light is then absorbed in travelling through the perspex:

$$I_2 = I_1' e^{-(\alpha_{perspex} \times 6mm)} = I_1' e^{-(0.0030 \times 6)} = 0.982I_1' \quad (3.8)$$

The linear attenuation coefficient of water is 0.00287 mm^{-1} [Driscoll WG and Vaughan W, 1978] and the value varies depending on the quality of water. However, the value of the linear attenuation coefficients varies from reference to reference [Driscoll WG and Vaughan W, 1978; Dugdale P *et al*, 1994]. The linear attenuation coefficient of the perspex is approximated to that of the linear attenuation coefficient of glass [Daniels, 1995].

Substituting equation (3.7) into equation (3.8):

$$I_2 = 0.982I_1' = 0.982 \times 0.96I_i = 0.943I_i \quad (3.9)$$

Subsequently, the light (I_2) is further reduced at the perspex/water interface:

$$I_2' = I_2 - I_{reflection2} = I_2 - \left[I_2 \left(\frac{n_{water} - n_{perspex}}{n_{water} + n_{perspex}} \right)^2 \right] \quad (3.10)$$

$$I_2' = I_2 - \left[I_2 \left(\frac{1.33 - 1.5}{1.33 + 1.5} \right)^2 \right] = 0.996I_2 \quad (3.11)$$

Substitute equation (3.9) into equation (3.11):

$$I_2' = 0.996I_2 = 0.996 \times 0.943I_i = 0.939I_i \quad (3.12)$$

I_2' traverses the cell being attenuated by water (linear attenuation of water is 0.00287 mm^{-1}).

$$I_3 = I_2' e^{-(\alpha_{\text{water}} \times 90 \text{ mm})} = I_2' e^{-(0.00287 \times 90)} = 0.772I_2' \quad (3.13)$$

Substituting equation (3.12) into equation (3.13):

$$I_3 = 0.772I_2' = 0.772 \times 0.939I_i = 0.725I_i \quad (3.14)$$

Then I_3 is reduced by reflection at the water/perspex interface (0.4%):

$$I_3' = I_3 - I_{\text{reflection}3} = I_3 - \left[I_3 \left(\frac{n_{\text{perspex}} - n_{\text{water}}}{n_{\text{perspex}} + n_{\text{water}}} \right)^2 \right] \quad (3.15)$$

$$I_3' = I_3 - \left[I_3 \left(\frac{1.5 - 1.33}{1.5 + 1.33} \right)^2 \right] = 0.996I_3 \quad (3.16)$$

Substitute equation (3.14) into equation (3.16):

$$I_3' = 0.996I_3 = 0.996 \times 0.725I_i = 0.722I_i \quad (3.17)$$

I_3' is further being attenuated by perspex (linear attenuation of perspex is 0.0030 mm^{-1}).

$$I_4 = I_3' e^{-(\alpha_{\text{perspex}} \times 6 \text{ mm})} = I_3' e^{-(0.0030 \times 6)} = 0.982I_3' \quad (3.18)$$

Substituting equation (3.17) into equation (3.18):

$$I_4 = 0.982I_3' = 0.982 \times 0.722I_i = 0.709I_i \quad (3.19)$$

I_4' is incident on the CCD linear image sensor after I_4 is reduced due to reflection at the perspex/air interface (the reflection on the front surface of the CCD sensor is neglected as the sensor is placed directly on the perspex).

$$I_4' = I_4 - I_{reflection4} = I_4 - \left[I_4 \left(\frac{n_{air} - n_{perspex}}{n_{air} + n_{perspex}} \right)^2 \right] \quad (3.20)$$

$$I_4' = I_4 - \left[I_4 \left(\frac{1-1.5}{1+1.5} \right)^2 \right] = 0.96I_4 \quad (3.21)$$

Substitute equation (3.19) into equation (3.21):

$$I_4' = 0.96I_4 = 0.96 \times 0.709I_i = 0.681I_i \quad (3.22)$$

I_4' is incident on the CCD sensor giving the saturation voltage (V_{sat}) which is approximately 1.7V based on the average values from four projection measurements (Figure 3.5 and Figure 3.6). The relationship of the CCD output voltage with the light intensity is linear (as shown in Figure 3.4), where the CCD output voltages are 1.7V (saturation voltage) during total illumination and 4.7V during total darkness, respectively.

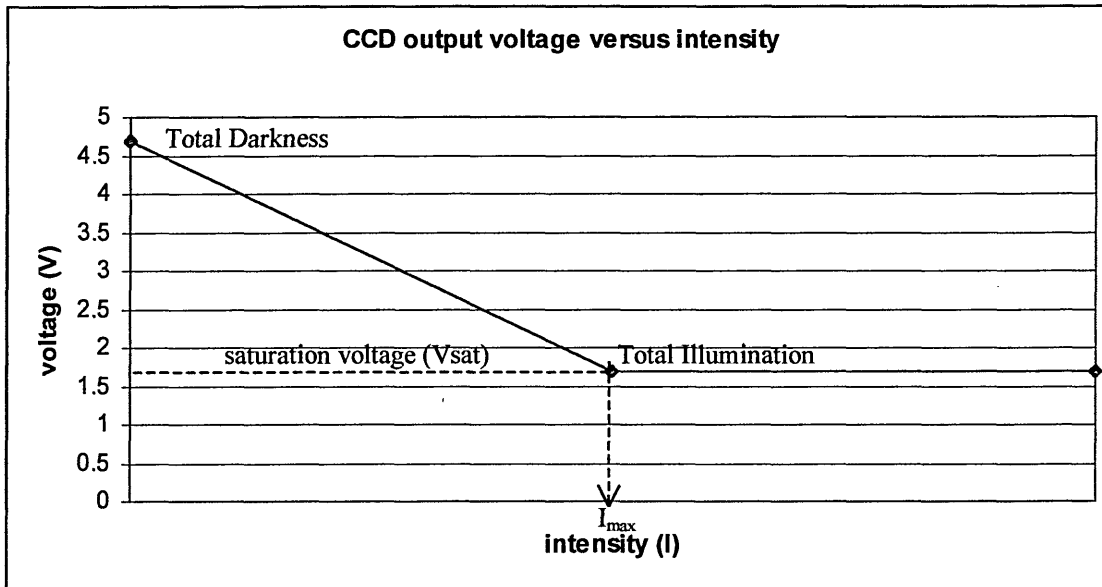


Figure 3.4. The relationship between the CCD output voltage and intensity.

The level of light intensity at the receiver, with only water in the test cell, was adjusted so that the sensor output voltage was very near to the saturation voltage level. Hence diffraction information is lost from the full illumination at each side of the shadow.

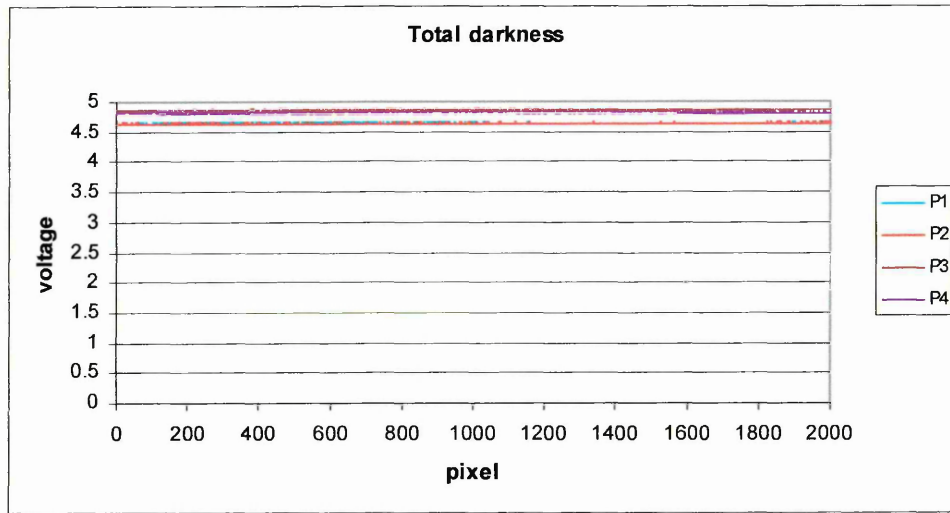


Figure 3.5. The CCD output voltage during total darkness.

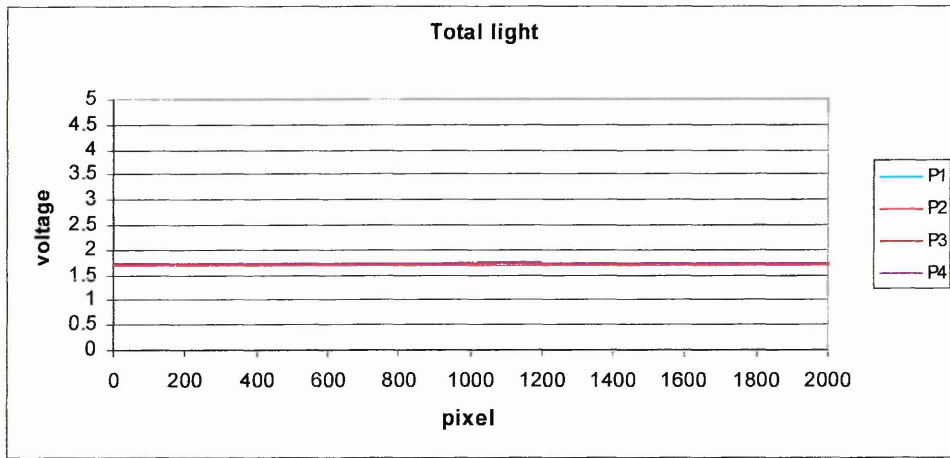


Figure 3.6. The CCD output voltage during total illumination.

From Figure 3.4, the relationship between the intensity, I_o (I_f), and the CCD output voltage, v , (the region before saturation occurred) is linear. The linear equation can be derived as follows.

$$v = -\left[\frac{4.7-1.7}{I_{o,\max}}\right]I_o + 4.7 = -3\frac{I_o}{I_{o,\max}} + 4.7 \quad (3.23)$$

$$\frac{I_o}{I_{o,\max}} = \frac{4.7-v}{3} \quad (3.24)$$

$$\therefore \ln\left(\frac{I_{o,\max}}{I_o}\right) = \ln\left[\frac{3}{4.7-v}\right] = \ln 3 - \ln(4.7-v) \quad (3.25)$$

From Section 3.2.1, when there is no particle, $I_{o,\max} = 0.68I_i$. This value is substituted into Equation 3.24 to obtain the relationship between output intensity and incident intensity.

$$\frac{I_o}{I_{o,\max}} = \frac{4.7 - v}{3} \Rightarrow \frac{I_o}{0.68I_m} = \frac{4.7 - v}{3}$$

$$\therefore \frac{I_m}{I_o} = \frac{3}{0.68(4.7 - v)}$$

Taking natural logarithm on both sides:

$$\ln\left(\frac{I_m}{I_o}\right) = \ln 3 - \ln[0.68(4.7 - v)] \quad (3.26)$$

This equation is used in Section 3.2.3.

3.2.2 With a circular/spherical particle (neglecting scattering effect)

Figure 3.7 shows a light illuminated a particle. In a case of an **opaque** particle with a diameter larger than the size of the sensor element, then there is no light detected by the CCD linear image sensor. Hence, the intensity is zero ($I_t=0$) due to the total shadow of the particle on the CCD linear image sensor (diffraction is neglected). This is the major effect with large particles.

The particle has three effects in a case of a **translucent** particle:

1. Light striking the particle is attenuated due to absorption.
2. The particle behaves as a thick lens.
3. There are reflection effects on the front and rear surface of the particle.

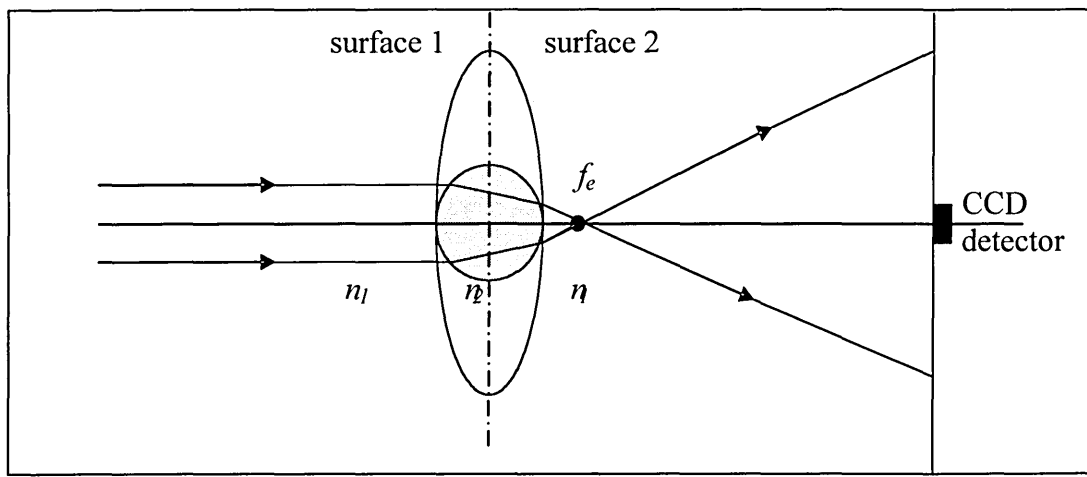


Figure 3.7. A light ray on a particle.

Consider the effects of light attenuation (due to absorption) and light reflectance on the particle, I_4' obtained from Section 3.2.1 (when there is no particle) is further reduced to I_4'' . The particle, assumed spherical with radius R , has its diameter on the principal axis through the centre of the CCD detection. The light beam along the principal axis strikes the particle normally (Figure 3.8) and loses 0.4% intensity by reflection. Beams parallel to the principal axis but not on it will lose more intensity by reflection. A similar operation as in Section 3.2.1 is performed in the calculation of I_4''/I_i . Details of the calculation are described in Appendix A and the result is as follows.

$$I_4'' = 0.96I_4 = 0.89I_i e^{-(0.27+2R\alpha_{particle})} \quad (3.27)$$

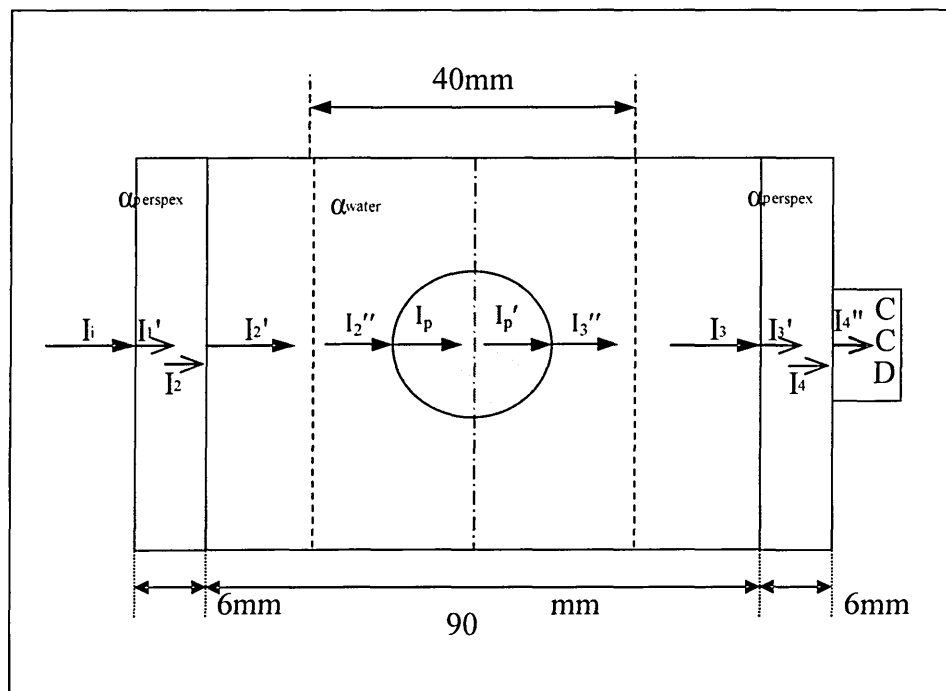


Figure 3.8. A light striking a particle in the middle of the pipe.

From Equation 3.27, different values of α_{particle} are used and the behaviour of the output-input ratio as the attenuation coefficient of the particle is increased is shown in Figure 3.9 and Table 3.1. The attenuation coefficient of an opaque object is infinity. Therefore, less light falls on the CCD linear image sensor as the attenuation coefficient becomes larger i.e. total shadow.

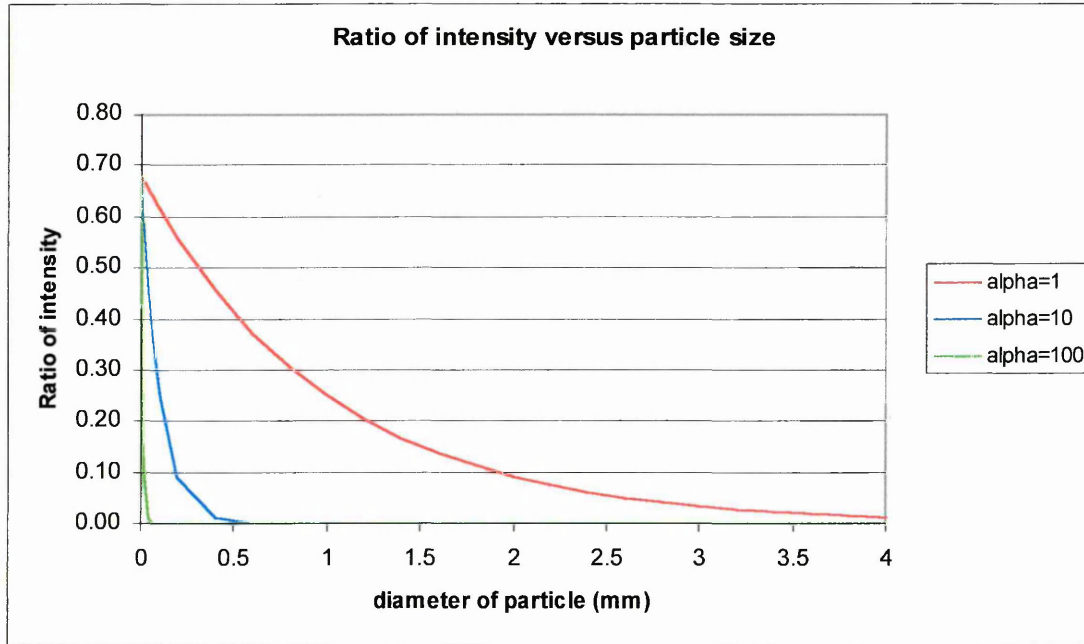


Figure 3.9. Output-input intensity ratio versus particle size.

Figure 3.9 shows that when a light beam striking a large particle (diameter R) where the radius of the particle is large compared to the size of the CCD linear sensor ($R \gg 0.014$ mm), the ratio of output intensity is almost zero as the linear attenuation coefficient of the particle is increased. Hence, the shadow of the particle is detected by the CCD linear image sensor.

Table 3.1. Ratio of intensity for different values of α_{particle} .

alpha=1/mm		alpha=10/mm		alpha=100/mm	
Diameter	Ratio Int	Diameter	Ratio Int	Diameter	Ratio Int
0	0.6794	0	0.6794	0	0.6794
0.014	0.6700	0.014	0.5906	0.014	0.1675
0.02	0.6660	0.02	0.5563	0.02	0.0919
0.04	0.6528	0.04	0.4554	0.04	0.0124
0.06	0.6398	0.06	0.3729	0.06	0.0017
0.08	0.6272	0.08	0.3053	0.08	0.0002
0.1	0.6148	0.1	0.2499	0.1	0.0000
0.2	0.5563	0.2	0.0919	0.2	0.0000
0.4	0.4554	0.4	0.0124	0.4	0.0000
0.6	0.3729	0.6	0.0017	0.6	0.0000
0.8	0.3053	0.8	0.0002	0.8	0.0000
1	0.2499	1	0.0000	1	0.0000
1.2	0.2046	1.2	0.0000	1.2	0.0000
1.4	0.1675	1.4	0.0000	1.4	0.0000
1.6	0.1372	1.6	0.0000	1.6	0.0000
1.8	0.1123	1.8	0.0000	1.8	0.0000
2	0.0919	2	0.0000	2	0.0000
2.2	0.0753	2.2	0.0000	2.2	0.0000
2.4	0.0616	2.4	0.0000	2.4	0.0000
2.6	0.0505	2.6	0.0000	2.6	0.0000
2.8	0.0413	2.8	0.0000	2.8	0.0000
3	0.0338	3	0.0000	3	0.0000
3.2	0.0277	3.2	0.0000	3.2	0.0000
3.4	0.0227	3.4	0.0000	3.4	0.0000
3.6	0.0186	3.6	0.0000	3.6	0.0000
3.8	0.0152	3.8	0.0000	3.8	0.0000
4	0.0124	4	0.0000	4	0.0000
4.2	0.0102	4.2	0.0000	4.2	0.0000
4.4	0.0083	4.4	0.0000	4.4	0.0000
4.6	0.0068	4.6	0.0000	4.6	0.0000
4.8	0.0056	4.8	0.0000	4.8	0.0000
5	0.0046	5	0.0000	5	0.0000
5.2	0.0037	5.2	0.0000	5.2	0.0000
5.4	0.0031	5.4	0.0000	5.4	0.0000
5.6	0.0025	5.6	0.0000	5.6	0.0000
5.8	0.0021	5.8	0.0000	5.8	0.0000
6	0.0017	6	0.0000	6	0.0000

Figure 3.10 shows an opaque particle just covering the CCD sensor in order to obtain the minimum size of a spherical particle, which casts a total shadow on the CCD linear image sensor.

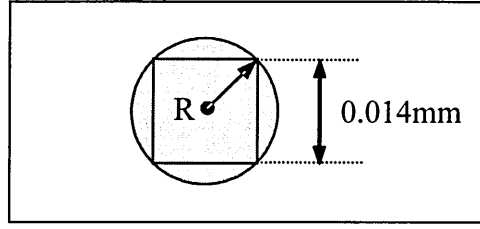


Figure 3.10. Size of particle greater than sensor size.

The ratio of the intensity (I_{out}/I_{in}) will decrease from 0.68 to almost zero when the sensor is fully covered by the particle.

$$I_{out}/I_{in} \approx 0 \Rightarrow R = [0.007^2 + 0.007^2]^{1/2} = 9.9 \times 10^{-3} \text{ mm} \quad (3.28)$$

As a result, there will be no light on the CCD linear sensor element for any particle diameter greater than 19.8 micron when centred on the CCD sensor.

The particle in this case is translucent and may act like a lens with an assumed linear attenuation coefficient (α_{particle} is 0.0030 mm^{-1}) greater than the linear attenuation coefficient of the surrounding (α_{water} is 0.00287 mm^{-1}). The effective thin lens of the particle is positioned at the centre of the sphere (Jenkins FA and White HE 1957) and the calculations involved are as follows. The refractive index of the material of the particle (glass bead) is assumed 1.55.

Power of first surface (F_1):

$$F_1 = (n_2 - n_1) / r_1 = (1.55 - 1.33) / r = 0.22/r \quad (3.29)$$

Power of second surface (F_2):

$$F_2 = (n_1 - n_2) / r_2 = (1.33 - 1.55) / -r = 0.22/r \quad (3.30)$$

Equivalent thin-lens power: $F_e = F_1 + F_2 - (dF_1F_2)/n$

$$\therefore F_e = 0.22/r + 0.22/r - [(2r \times 0.22/r \times 0.22/r)/1.5] = (0.44 - 0.0645)/r$$

$$F_e = 0.3755/r \text{ or } 0.751/d \text{ dioptre} \quad (3.31)$$

The equivalent thin-lens focal length, f_e is the reciprocal of lens power (F_e).

$$\therefore f_e = 2.663r \text{ or } 1.3315d \text{ metre} \quad (3.32)$$

For particles of diameter less than or equal to 10-mm (particle sizes of interest),

$$f_e \leq 0.0133 \text{ m} \equiv 13.3 \text{ mm}$$

Figure 3.11 shows a 1 mm collimated beam of light striking a spherical particle which is assumed to behave like a thick lens [Jenkins and White, 1957] in the middle of the pipe (Figure 3.12). The intensity of light being arriving at the CCD linear image sensor is calculated by looking at the output beam height i.e. h_i .

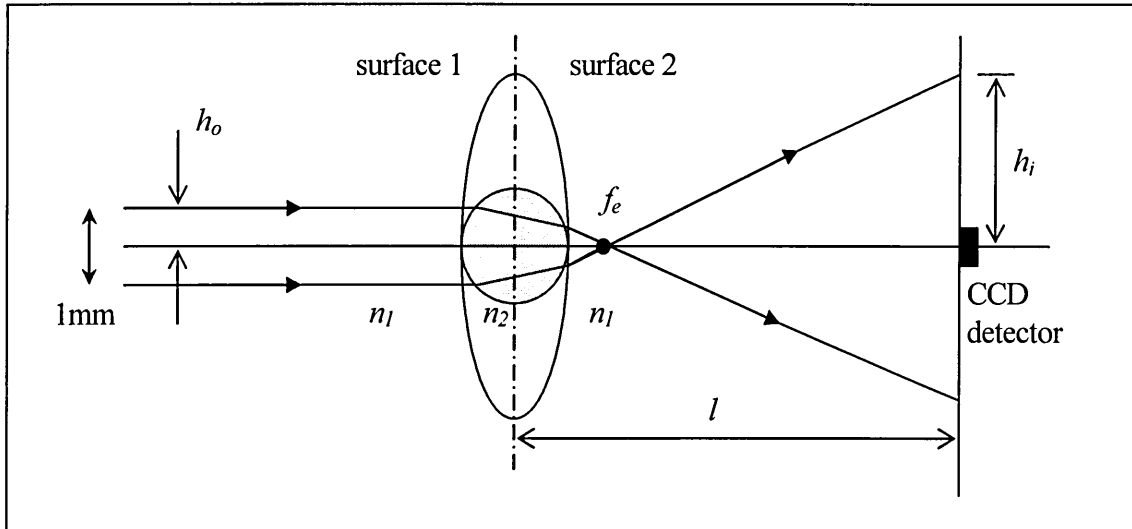


Figure 3.11. A light ray on a particle.

By similar triangles: $h_o/f_e = h_i/(l - f_e) \Rightarrow h_o/1.3315d = h_i/(l - 1.3315d)$

$$\therefore h_i = (l - 1.3315d)h_o/1.3315d \text{ metre}$$

If the particle has a diameter of 1-mm and is in the middle of the pipe:

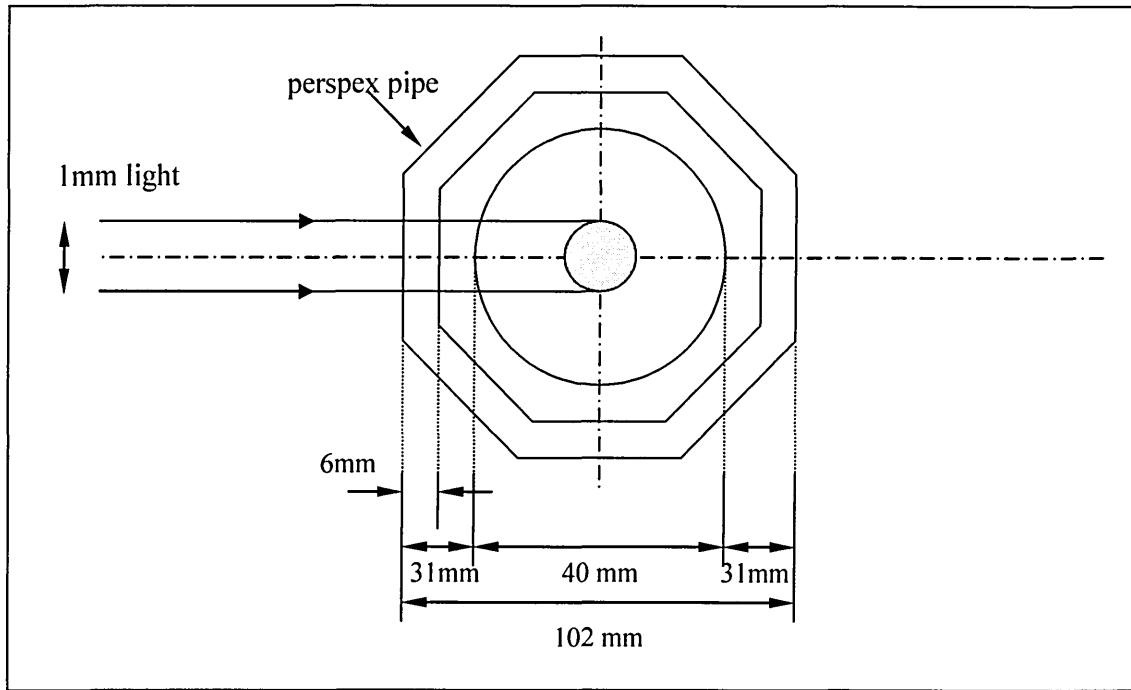


Figure 3.12. Top view of a particle in the middle of the pipe.

Diameter of the particle in Figure 3.12, $d = 1 \times 10^{-3} \text{ m}$

The focal length, f_e : $f_e = 1.3315d = 1.3315 \times 1 \times 10^{-3} = 1.3315 \times 10^{-3} \text{ m}$

$$l = 20 \text{ mm} + 31 \text{ mm} = 51 \text{ mm}$$

$$h_o = 0.5 \times 10^{-3} \text{ m}$$

$$\therefore h_i = [(51 \text{ mm} - 1.3315 \text{ mm})/1.3315 \text{ mm}] \times 0.5 \text{ mm} = 18.651 \text{ mm}$$

The output beam height is **37.3 mm** (2 x 18.65 mm).

The relationship between the output beam height and the particle size, with the particle located at three different positions – 71-mm (farthest), 51-mm (middle) and 31-mm (closest) to the CCD sensor, is shown in Figure 3.13a. From the graph, the output beam height is getting smaller as the particle diameter is increased i.e. less lens effect. This means that the smaller the particle, the higher the lens power i.e. the greater the refraction of the beam and the larger h_i (Figure 3.11).

Figures 3.13b and 3.13c shows the percentage of light that falls on the CCD linear image sensor for different sizes of particle. The transmitted light on the CCD linear image sensor is only 0.037 % (0.014 mm/37.3 mm x 100) of the light normally arriving

for the particle diameter of 1-mm. Therefore, the light transmitted to the CCD linear sensor due to the lens effect of the particle is negligible.

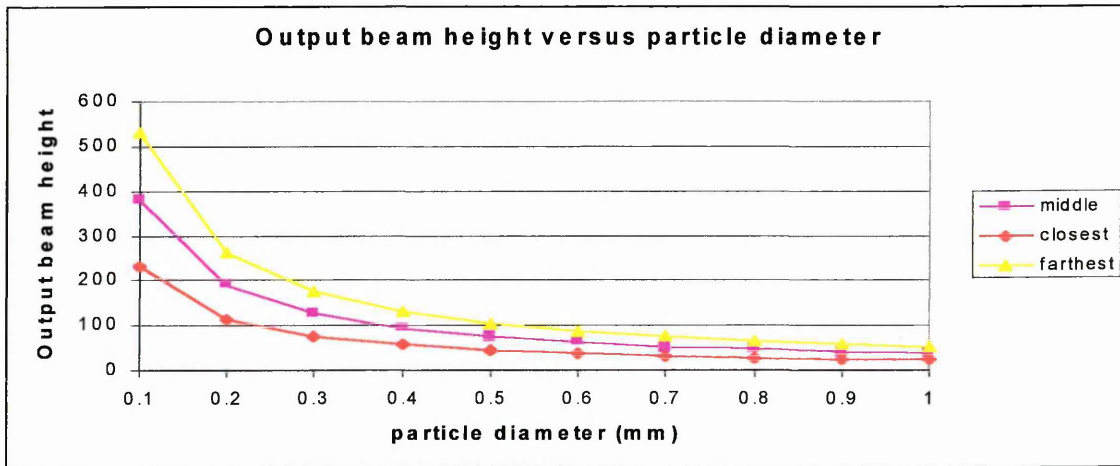


Figure 3.13(a). Relationship between the output beam height and the particle diameter.

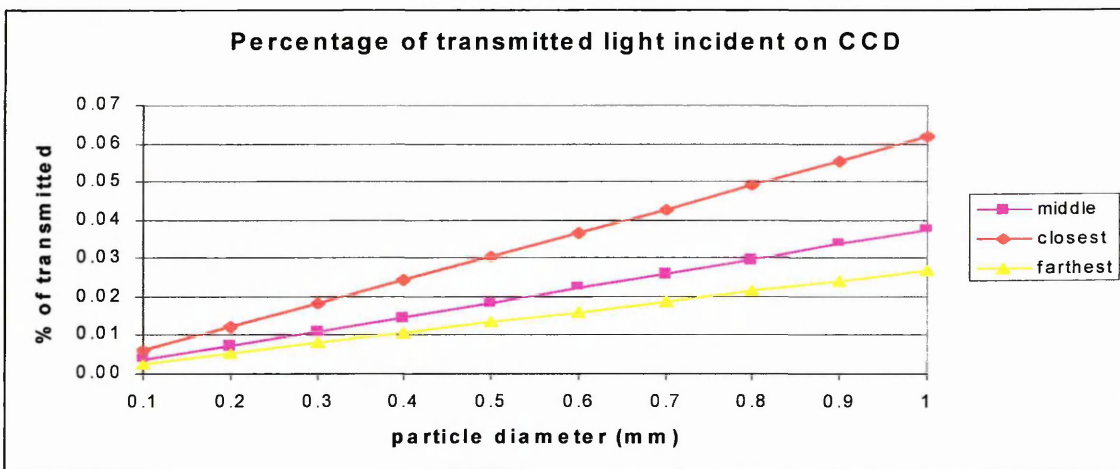


Figure 3.13(b). Percentage of transmitted light on the CCD (particle size below 1mm).

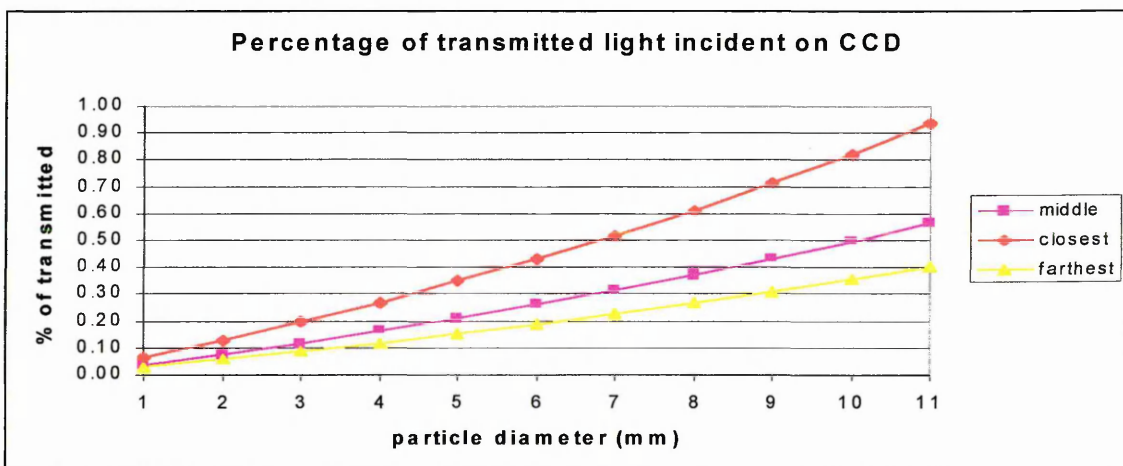


Figure 3.13(c). Percentage of transmitted light on the CCD (particle size 1mm-11mm).

3.2.3 Modelling for the image reconstruction process

The mathematical model used for the image reconstruction process considers only the measurement section (instead of the full layout of the system mentioned in Section 3.2.2). Therefore, the equation used is different from Equation 3.26. Details of techniques used in the image reconstruction process are discussed in Chapter 5.

Figure 3.14 shows the measurement section of the system with the dimension of 30 mm i.e. the size of the CCD linear image sensor. The output-input intensity ratio of the measurement section is I_o'/I_i' (full calculations on I_o'/I_i' can be found in Appendix B).

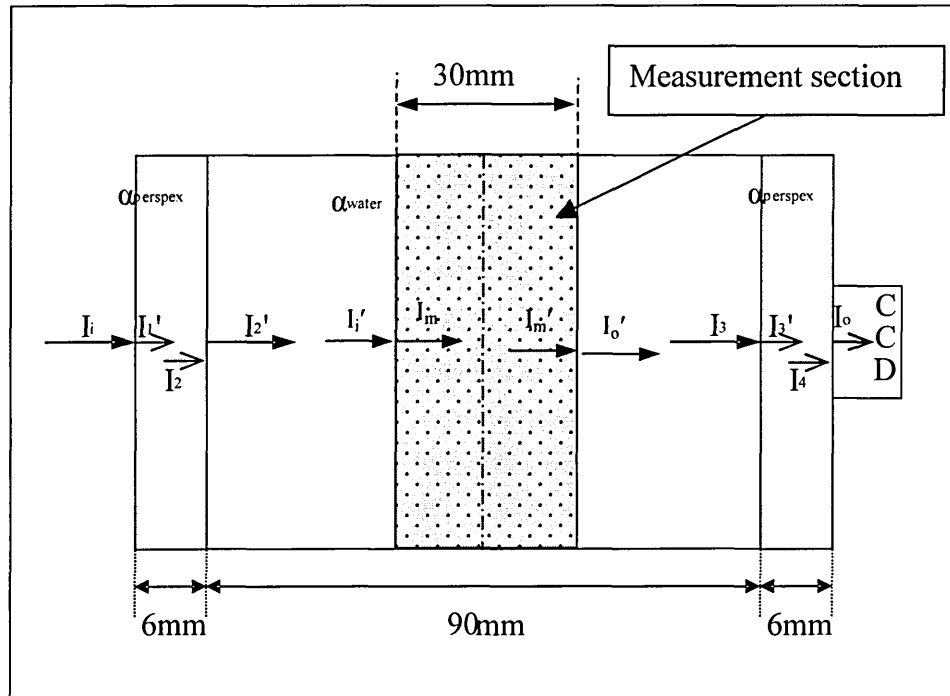


Figure 3.14. Layout of the measurement section.

$$\frac{I_o'}{I_i'} = \frac{1}{0.74} \left[\frac{(0.68)(4.7 - v)}{3} \right] \quad (3.33)$$

$$\frac{I_i'}{I_o'} = 0.74 \left[\frac{3}{(0.68)(4.7 - v)} \right] \quad (3.34)$$

Taking natural logarithm on both sides:

$$\ln \left[\frac{I_i'}{I_o'} \right] = \ln(0.74) + \ln(3) - \ln[(0.68)(4.7 - v)] \quad (3.35)$$

Equation 3.35 is used in the determination of the matrix [M] for the image reconstruction process (inverse problem) discussed in Chapter 6, which relates the transmitted light intensity to the output voltage of the CCD linear image sensor.

3.3 Effects due to light sources

Light sources play an important role in the process of achieving accurate results. The CCD linear sensor is a light-sensitive device and easily saturates. The light falling on the CCD linear sensor needs to be well collimated to produce an accurate image, with a uniform controlled intensity across the 2048 active pixels of the CCD linear sensor. Two different light sources are tested on the CCD linear sensor – white light and laser.

a. White light

When white light passes through a prism, it produces the rainbow - all the colours of the spectrum; but a mixture of red, green and blue primary colours in the correct proportions may be combined to produce white light. The wavelengths of each of the primary colours are as follows [Hecht E, 1987]:

Red : 622 to 780 nm

Green : 492 to 577 nm

Blue : 455 to 492 nm

When white light hits a transparent, spherical particle (which is assumed to behave like a lens); the particle will refract the different colour components according to their different wavelengths - λ_{red} , λ_{green} and λ_{blue} . As a result, there will be three different focal points, one for each of the wavelengths (as shown in Figure 3.15). Separate images may be produced due to the different refractive indices.

A simple collimating lens may introduce chromatic aberration problems. If the collimating lens has a diameter of 50 mm, a nominal focal length of 200 mm and is made of crown glass, the refractive indices for the three primary colours are:

$$n_{red} \approx 1.5, \quad n_{green} \approx 1.51, \quad n_{blue} \approx 1.52$$

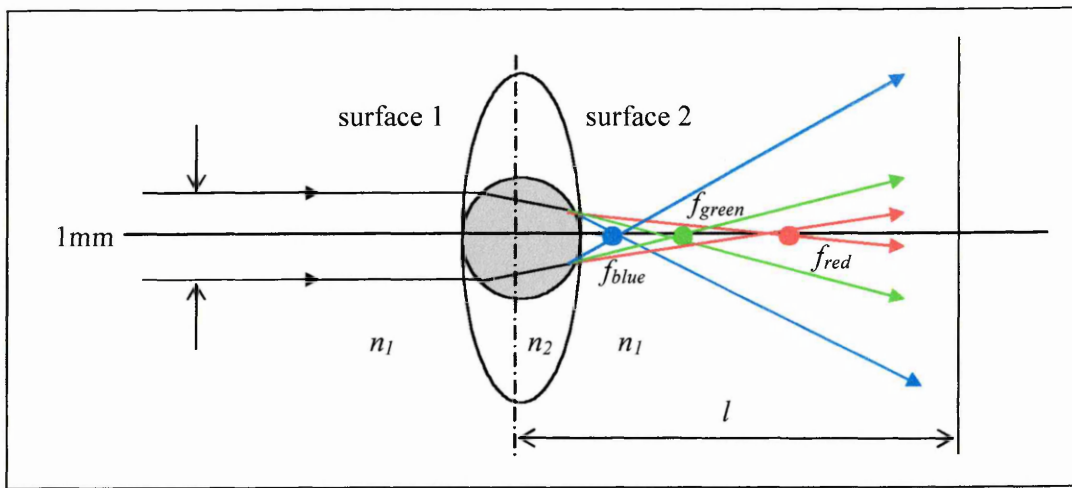


Figure 3.15. White light source illuminating a particle.

Using the simple thin lens equation [Hecht E, 1987], the focal length:

$$1/f = (n-1)(1/r_1 - 1/r_2) \quad (3.36)$$

Let $f_{green} = 200 \text{ mm}$: $1/f_{green} = 1/200 = (1.51 - 1)(1/r_1 - 1/r_2)$

$$(1/r_1 - 1/r_2) = 1/(200 \times 0.51) = 1/102 \quad (3.37)$$

$$1/f_{red} = (1.5 - 1)(1/r_1 - 1/r_2) \quad (3.38)$$

Substitute equation (3.37) into (3.38):

$$1/f_{red} = (1.5 - 1)(1/102) = 4.902 \times 10^{-3} \Rightarrow f_{red} = 204 \text{ mm} \quad (3.39)$$

Similarly, $1/f_{blue} = (1.52 - 1)(1/102) = 5.098 \times 10^{-3} \Rightarrow f_{blue} = 196.2 \text{ mm} \quad (3.40)$

The effect on image size for the red and the blue is now derived assuming the white light source is centred at the f_{green} point (Figure 3.16).

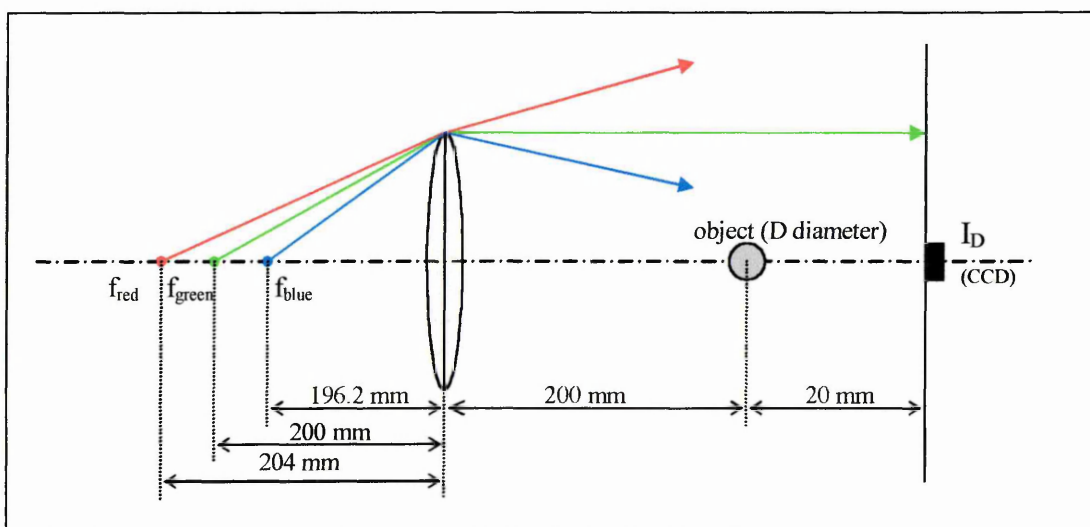


Figure 3.16. Chromatic aberration.

For red: $1/f_{red} = 1/l_1 + 1/l_2 \Rightarrow 1/204 = 1/200 + 1/l_2$
 $1/l_2 = 1/204 - 1/200 \Rightarrow l_2 = -10200 \text{ mm}$ (3.41)

(The light appears to be coming 10200-mm to the left of lens - virtual image.)

By similar triangles: $D/(10200 + 200) = I_D/(10200 + 200 + 20)$
 $I_D/D = 10420/10400 = 1.002$ i.e. 0.2 % larger than the object (3.42)

For blue: $1/f_{blue} = 1/l_1 + 1/l_2 \Rightarrow 1/196.2 = 1/200 + 1/l_2$
 $1/l_2 = 1/196.2 - 1/200 \Rightarrow l_2 = 10326 \text{ mm}$ (3.43)

(The light appears to be coming 10326-mm to the right of lens - real image.)

By similar triangles: $D/(10326 - 200) = I_D/(10326 - 200 - 20)$
 $I_D/D = 10106/10126 = 0.998$ i.e. 0.2 % smaller than the object (3.44)

Discussion: Using white light with the CCD without a good quality achromatic lens will produce errors in the image height due to colour aberration. The use of colour filters (to produce near monochromatic light) will reduce this error. An achromatic lens is required in order to provide a uniformly collimated white light beam. A simple lens can only collimate one colour (chromatic aberration).

b. Laser

The optical tomography system requires a monochromatic and collimated light source. The best light source which can fulfil the requirements is a laser. The main disadvantage of the laser is its high intensity, which may saturate or burn the CCD linear sensor if the intensity is not controlled. This problem can be overcome by using a neutral density (ND) filter between the CCD sensor and the laser. The laser generally produces a collimated beam approximately 1 mm in diameter. To produce full illumination on the CCD linear sensor, the beam is expanded using a telescope. This consists of a microscope eyepiece and a spherical lens (Figure 3.17).

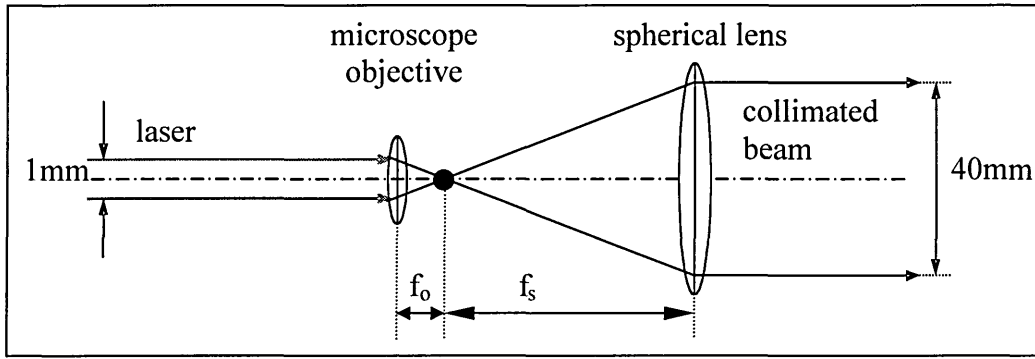


Figure 3.17. Collimated beam produced by laser.

A collimated light beam is obtained when the microscope objective is located exactly at the focal point of the spherical lens. The minimum required output beam diameter:

$$D_{out(min)} = 2048 \text{ pixels} \times 0.014 \text{ mm/pixel} = 28.7 \text{ mm}$$

Therefore, the measurement system (Section 4.1) requires a 28.7 mm diameter collimated beam. Hence, the required magnification is chosen to be 40 ($M = 40$). It is aimed for D_{out} to equal 40 mm in order to try to obtain uniform illumination across the CCD linear sensor.

The standard focal length of the objective lens (f_o) is 4 mm [Hecht E, 1987]. Therefore, for a microscope magnification of 40x, the required spherical lens will have a focal length (f_s) of 160 mm in order to obtain 40 mm diameter output beam.

$$\text{By similar triangles: } f_s/40 \text{ mm} = f_o/1 \text{ mm} \Rightarrow f_s = 40 \times 4 = 160 \text{ mm}$$

3.4 Effects due to diffraction

An opaque body placed midway between a screen and a point source casts an intricate shadow made up of bright and dark regions due to bending of the light [Hecht E, 1987]. This phenomenon is called diffraction.

When the light source or the screen is close to the obstruction (Figure 3.18), and the light comes from a point source, the diffraction effect is called Fresnel or Near-field diffraction. Whereas when the light source is extended and both it and the screen are far from the obstruction, this type of diffraction effect is called Fraunhofer or Far-field diffraction. It is assumed that the diffraction effect in the optical tomography system is mainly Fresnel diffraction, since the particle is close to the CCD linear sensor (the farthest distance between the particle and the sensor is 71 mm).

The effect of diffraction is closely related to the size of the obstruction. If the size of the particle or the obstruction is very large compared to the wavelength of the light source (λ), the diffraction effects will be small. Diffraction effects become more pronounced, as the size of the obstruction becomes smaller.

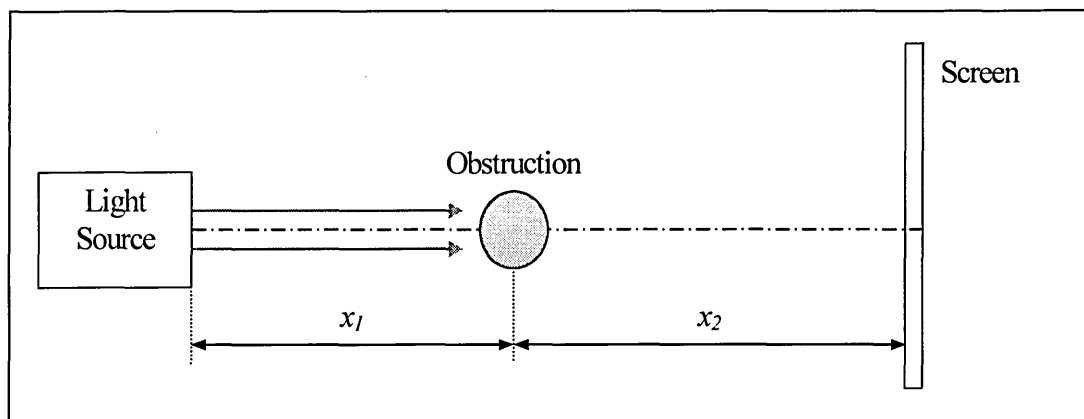


Figure 3.18. A light strikes an obstruction.

Figures 3.19 to 3.21 show the effect of diffraction when the light is bent by an opaque obstruction and the related fringe pattern on the screen. Hence, there is still some light at the edge of the opaque obstruction - no total shadow or total darkness at the screen; some light 'softens' the edge of the shadow.

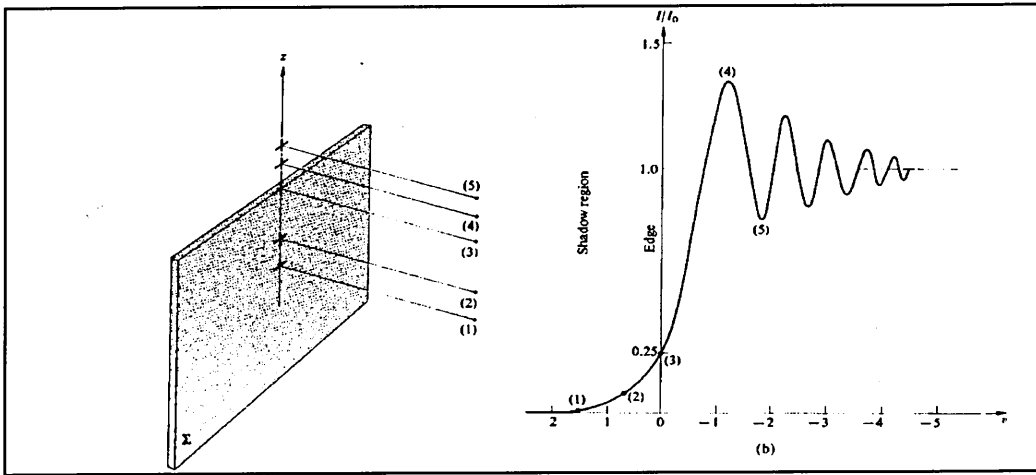


Figure 3.19. The opaque screen and the intensity distribution (Hecht E, 1987).

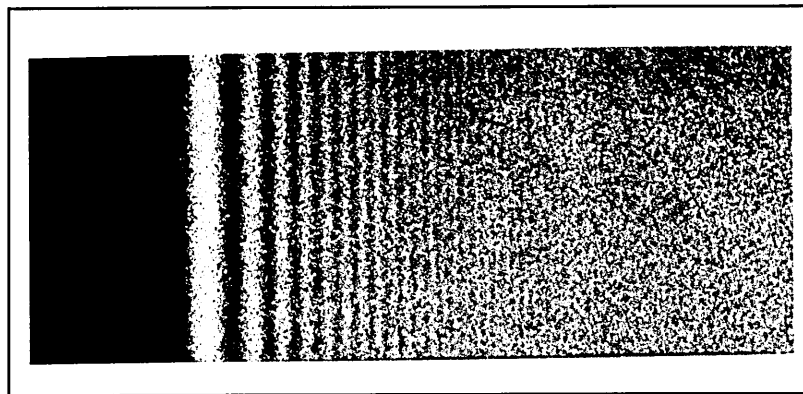


Figure 3.20. The fringe pattern (Jenkins FA and White HE, 1957).

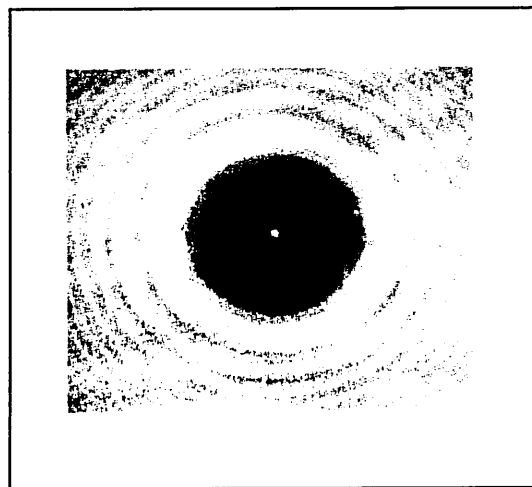


Figure 3.21. The shadow pattern cast by a $1/8$ -inch diameter rod (Jenkins FA and White HE, 1957).

3.4.1 Diffraction at a straight edge

The intensity of the diffraction pattern can be derived from two Fresnel integrals known as Fresnel Cosine integral (C) and Fresnel Sine integral (S). Both of the Fresnel integrals are a function of parameter, v , which is the arclength along the amplitude vector diagram called the Cornu Spiral. The Cornu Spiral is the graphical aid used in evaluating the Fresnel integrals (Smith FG and Thomson JH, 1988). Figure 3.22 shows the diffraction at a straight edge where the Cornu Spiral is shown in Figure 3.22b.

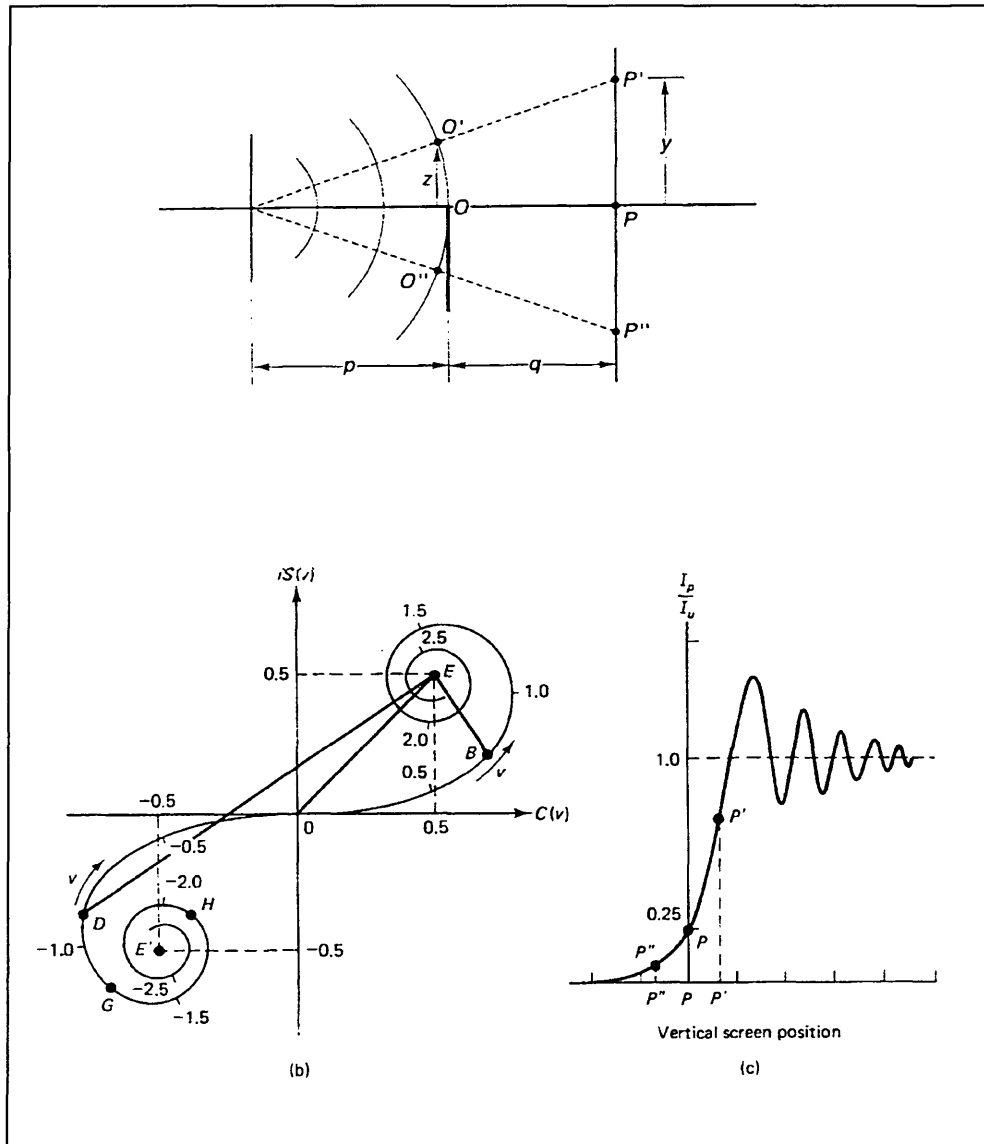


Figure 3.22. Diffraction at a straight edge.

The expression for Fresnel diffraction involves the width of the obstacle in the same reduced unit i.e. v . For an actual width w , a reduced width is defined as Δv (Smith FG and Thomson JH, 1988).

$$\Delta v = w \sqrt{\frac{2}{\lambda b}} \quad (3.45)$$

where: Δv is the reduced width

w is the width of the obstacle

λ is the light wavelength

b is the distance between the obstacle and the sensor

The Fresnel integrals consist of sine and cosine functions, where $S(v)$ is the Fresnel Sine function and $C(v)$ is the Fresnel Cosine function (Smith FG and Thomson JH, 1988).

The integrals are defined as below:

$$S(v) = \int_0^v \sin\left(\frac{\pi t^2}{2}\right) dt, \quad C(v) = \int_0^v \cos\left(\frac{\pi t^2}{2}\right) dt \quad (3.46)$$

The intensity can be expressed in terms of Fresnel integrals (C and S), where both of the integrals are functions of v (Smith FG and Thomson JH, 1988).

$$\frac{I_p}{I_m} = \frac{1}{2} \left\{ \left[\frac{1}{2} + C \right]^2 + \left[\frac{1}{2} + S \right]^2 \right\} \quad (3.47)$$

The diffraction pattern shown in Figure 3.22c is derived using this equation.

At the edge of the geometric shadow, the upper half of the zones of the Cornu spiral (OE in Figure 3.22b) is effective. The resulting amplitude,

$$A = \sqrt{\left[\left(\frac{1}{2}\right)^2 + \left(\frac{1}{2}\right)^2\right]} = \sqrt{\frac{1}{2}} \quad (3.48)$$

The intensity I_p , where P is the linear shadow edge of the object is:

$$I_p = \frac{1}{2} I_o = \frac{1}{4} I_m \quad (3.49)$$

Hence, the edge of the shadow is not sharp.

In a case of an unobstructed wavefront, the intensity is unity.

$$\int_0^{\infty} \cos\left(\frac{\pi v^2}{2}\right) dv = \int_0^{\infty} \sin\left(\frac{\pi v^2}{2}\right) dv = 0.5 \quad (3.50)$$

3.4.2 Diffraction by a circular obstacle

When coherent and collimated light strikes a circular object, there is a bright spot in the centre of the shadow (Figure 3.21). However, the bright spot can be observed only if the obstacle is smooth and exactly circular (Longhurst RS, 1967). Besides the spot and faint rings in the shadow, there are bright circular fringes bordering the outside of the shadow (Jenkins FA and White HE, 1987). This type of diffraction can be observed with small diameters of wire.

Diffraction by a thin obstacle (wire)

The intensity for the diffraction by a wire can be expressed in terms of Fresnel integrals (Equation 3.46), where the Cornu Spiral is shown in Figure 3.23.

$$\frac{I_p}{I_{in}} = \frac{1}{2} \left\{ [1 + C(v - \Delta v) - C(v + \Delta v)]^2 + [1 + S(v - \Delta v) - S(v + \Delta v)]^2 \right\} \quad (3.51)$$

This equation is used to calculate the expected light intensities produced by diffraction around a thin wire (Section 3.4.3).

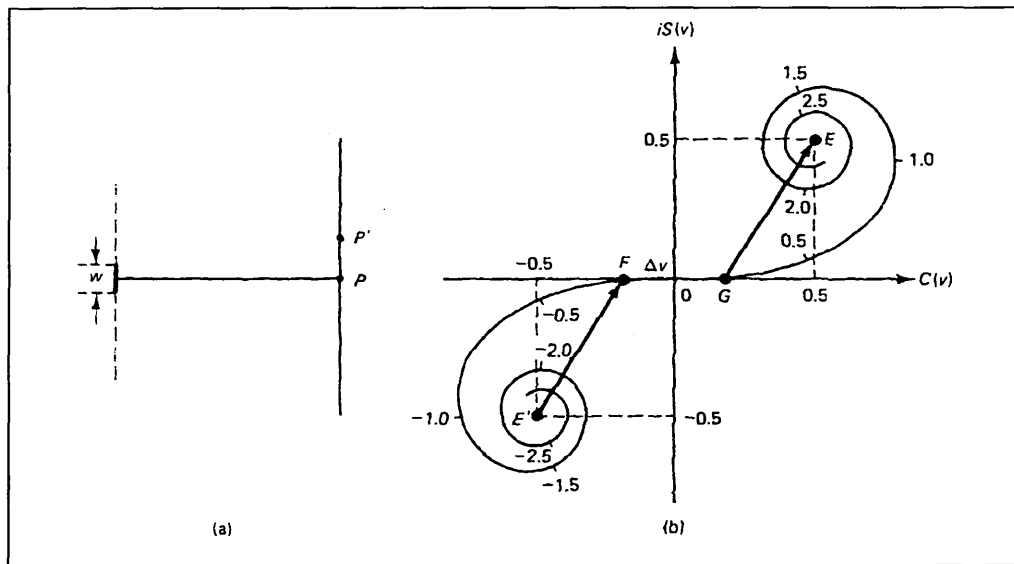


Figure 3.23. The Cornu Spiral for the diffraction by a wire.

3.4.3 Diffraction in the optical tomography system

The laser module used in the optical tomography system has a wavelength of 680 nanometre, which strikes a particle of interest ranging from 0.18mm up to 10mm. Thus, the particle size is much greater than the wavelength of the laser module (λ). However, diffraction effects do occur.

The diffraction effects depend on the distance between the measured object and the CCD linear image sensor. This distance should be as small as possible to avoid widening of edges - boundaries between light and shadow on the sensor (Fischer J *et al.*, 2002). The majority of experiments performed on the optical tomography system have a fixed distance between the CCD sensor and the light source, and between the object and the CCD sensor. The object is placed in the middle of the measurement section throughout these experiments.

The examples and theories regarding the Fresnel diffraction are based on a point light source. However, the optical tomography system is based on a plane wave light source i.e. parallel light. Therefore, it can be concluded that the diffraction is neither totally Fresnel nor Fraunhofer. However, because the image screen (the CCD sensor) is close to the object, Fresnel diffraction has been used in the modelling.

The exact location of edges of the object is crucial in order to achieve accurate particle size measurements. The simplest method used in determining the position of edges of the particle is by comparing the sensor output signal with a threshold level. The threshold level is set to 25% of the signal's amplitude; this follows from the analysis of the light diffraction on the edge of the measured object illuminated by a parallel light source (Figure 3.22c).

The output voltage of the CCD linear image sensor is captured on a pixel per pixel basis. Particle size measurements are obtained by setting a threshold level at 25% of full illumination of the signal's amplitude, and counting the numbers of pixels between the two edges of the particle as determined by the threshold voltage. These pixel values are converted to millimetres by multiplying by 0.014, in order to obtain the measured diameter of the particle.

The calculated Fresnel diffraction patterns are derived from the Fresnel integrals (Equation 3.51) using Maple6 Software. Figures 3.24 to 3.27 show the calculated variation in light intensity value for different sizes of particle diameter ranging from 2 mm down to 0.1 mm.

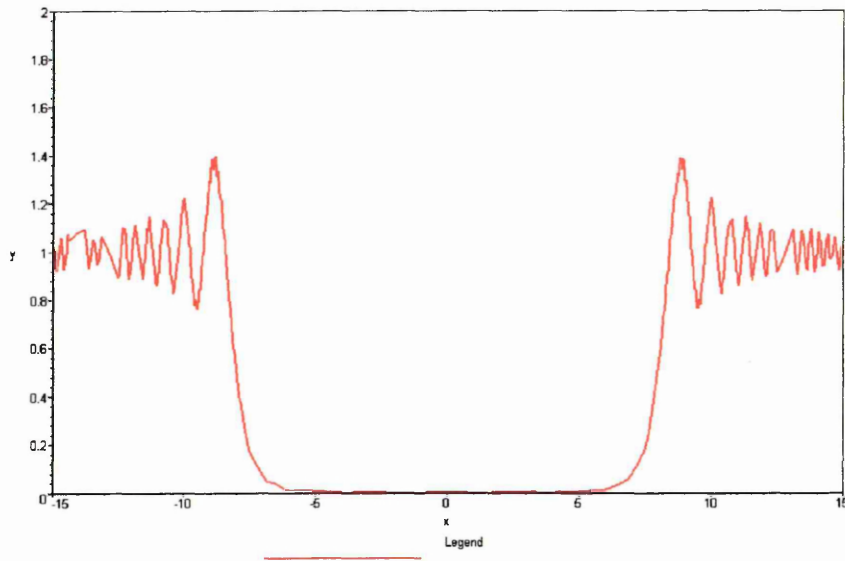


Figure 3.24. Fresnel diffraction for particle size of 2-mm ($\Delta v = 7.65$).

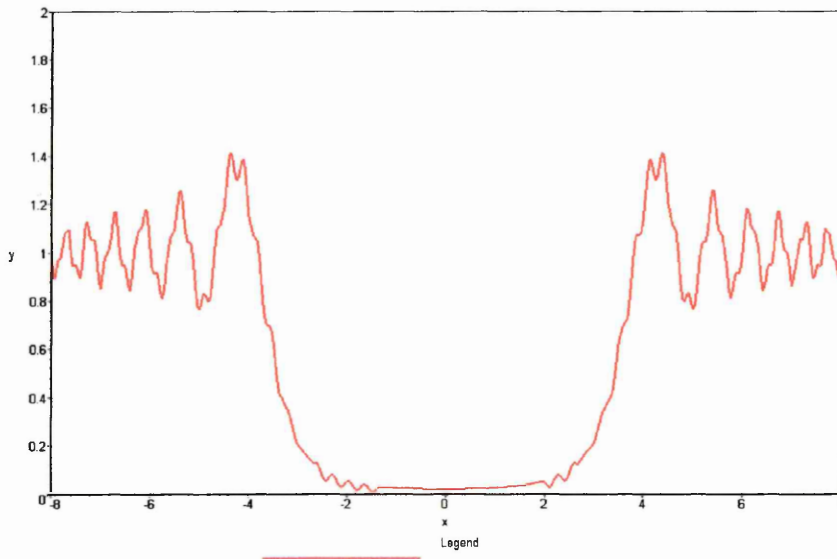


Figure 3.25. Fresnel diffraction for particle size of 0.8-mm ($\Delta v = 3.06$).

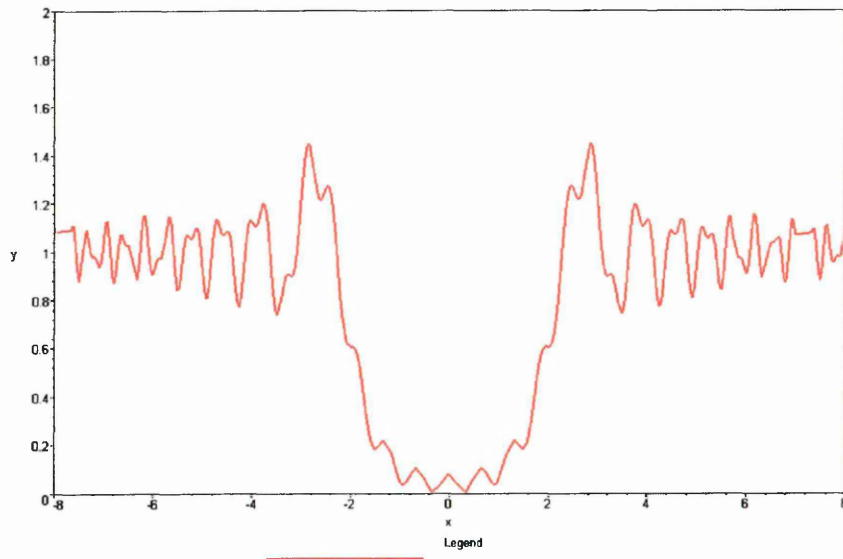


Figure 3.26. Fresnel diffraction for particle size of 0.4-mm ($\Delta v = 1.53$).

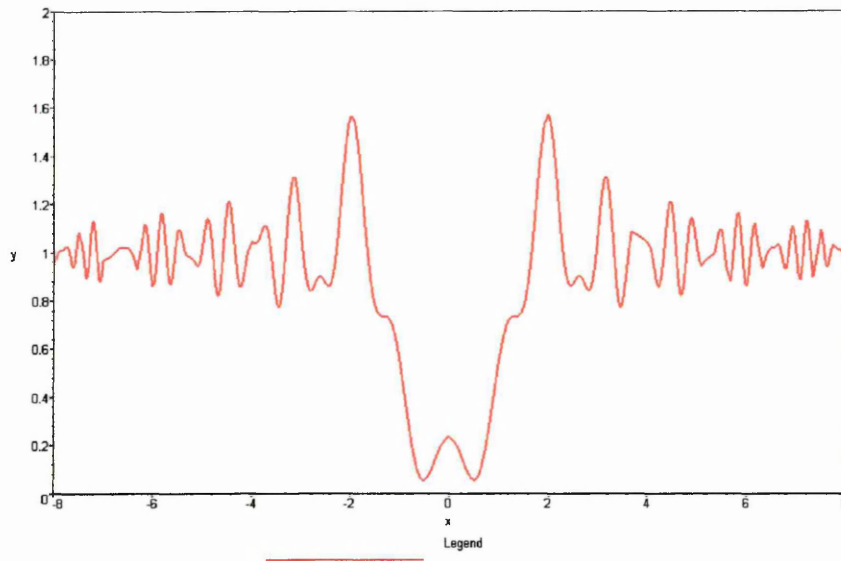


Figure 3.27. Fresnel diffraction for particle size of 0.2-mm ($\Delta v = 0.77$).

Discussion

The results shown in Figures 3.24 to 3.27 show the expected increase in diffraction effects as the object diameter is decreased. The modelled diameters based on 25% illumination are shown on each figure. Measured values are shown in Chapter 6.

3.5 The scan rate

It is important to understand the dynamic behaviour of a known particle, especially the speed of the particle when it flows past the CCD linear sensor. If the particle flows too fast, the CCD linear sensor may not be able to capture any image of the particle. Therefore, the maximum operating speed of the particle needs to be modelled and calculated. Figure 3.28 shows the configuration used in considering the relationship between the clock speed of the CCD linear sensor and the speed of the particle.

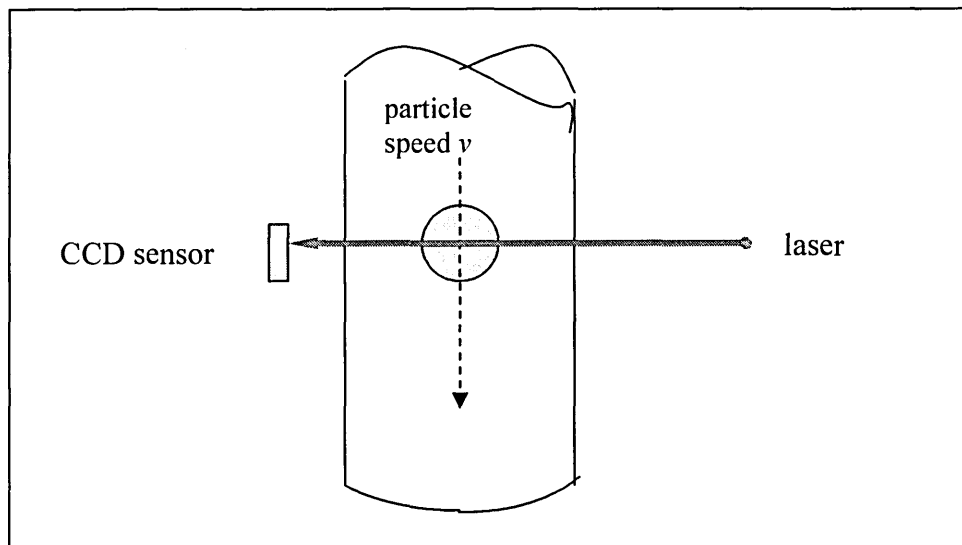


Figure 3.28. The configuration used for the calculation of the CCD speed.

The height of the array in the CCD linear sensor element is 0.014-mm and the image distance, d , of the particle at the CCD sensor can be calculated.

$$\text{Velocity} = \text{Distance} / \text{Time} \quad \Leftrightarrow \quad v = d/t$$
$$v_p = 0.014 \text{ mm} / t$$

In order to fully scan the particle, the maximum velocity of the particle, v_m , is related to the CCD clock speed. Each scan consists of 2100 pixels and each pixel is read at the clock speed (Figure 3.29). Therefore, the particle must move a maximum distance of 0.014 mm in the time taken to complete a scan. This clock speed will enable full information about the outline of the particle to be obtained.

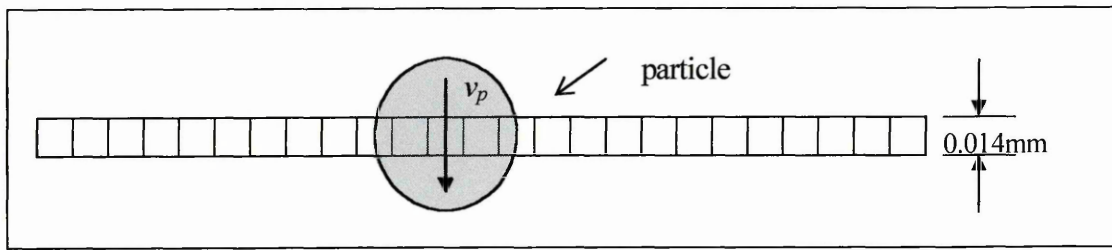


Figure 3.29. Scanning a particle.

With a clock of f MHz, 1 clock period is $1/f$ μ seconds and a scan takes:

$$T_{scan} = 2100/f \mu\text{sec} \equiv 2.1/f \text{ msec}$$

[If $f = 1$ MHz, $T_{scan} = 2.1$ msec; if $f = 5$ MHz, $T_{scan} = 0.42$ msec]

For touching scans, $v_p = s/t = 0.014/T_{scan} \text{ mms}^{-1}$

The relationship between the velocity of the particle and time is shown in Figure 3.30. From the graph, the maximum speed of the particle is 0.0067 m/s when the CCD linear sensor is clocked at a rate of 1 MHz. The scan rate of the CCD should be increased as the particle moves faster in order to fully captured the pixel readings of the CCD linear image sensor. The CCD is assumed to have captured 2100 pixels per line scan.

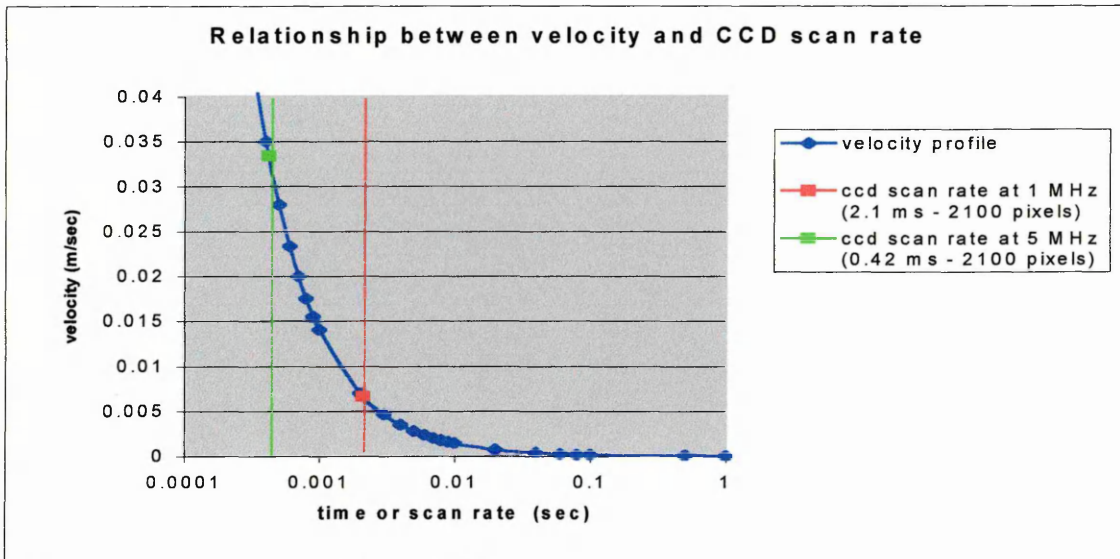


Figure 3.30. A graph shows the velocity of the particle versus time.

3.6 Discussions

This chapter compares the use of a white light and a monochromatic laser as the light sources for the collimated light. The laser is used because it introduces less aberration than the white light. It then presents models relating to light transmitted by transparent particles and expected changes in detected intensity due to both translucent and opaque solids. The effect of diffraction around the particle is described, and the maximum velocity, which will permit a complete scan of the particle to be obtained, is calculated. The next chapter presents the design of the tomography system.

CHAPTER 4

DESIGN OF THE OPTICAL TOMOGRAPHY SYSTEM

4.1 Overview of the system

The complete optical tomography system (Figure 4.1) consists of four projections (Figure 4.2); each channel or projection has a lighting system, detection system, triggering system and data acquisition system. The lighting system consists of a laser diode, an objective lens and a spherical lens. All of these components are assembled in a metal-box termed the 'ray-box'. The measurement section is shown in Figures 4.2 and 4.3, with the four projections system surrounding an octagonal shaped flow pipe.

The laser module used in the system produces red light at a wavelength of 680 nanometer. The laser module operates at the maximum power of 3mW with a supply of 3V and was chosen due to its low power since the Sony ILX551A CCD linear image sensor is very sensitive to light. The CCD can be easily saturated if the light illuminating it is too bright. The other reason is due to safety as the laser module used is a Class II type.

The laser has a beam diameter of approximately 1 mm. The minimum required output in order to illuminate the CCD linear image sensor is 28 mm. To provide reasonably uniform illumination the laser is to be expanded to 40 mm i.e. a beam expander of 40 times. The beam expander lens has a focal length of 4 mm and is used with a spherical lens as a telescope with a magnification of 40 times.

$$\text{Magnification} = f_{\text{spherical}}/f_{\text{beam expander}} \quad (4.1)$$

$$40 = f_{\text{spherical}}/4\text{mm} \quad \Rightarrow \quad f_{\text{spherical}} = 160 \text{ mm} \quad (4.2)$$

The diameter of the spherical lens is 50 mm to ensure the magnified beam is transmitted out properly onto the CCD linear image sensor. The output light from the ray-box is collimated and monochromatic, and is passed through a 1 mm width slit at the 'nose' of the ray-box.

The detection system is the sensing component in the optical tomography system where objects in the test cell are sensed using a charge coupled device (CCD) linear image sensor. The linear image sensor used is the Sony ILX551A with 2048 pixels where each pixel size is 14-micron by 14-micron. The output of the CCD linear image sensor is then acquired by the Keithley-DAS data acquisition system.

The Keithley DAS data acquisition system is capable of acquiring data at a maximum rate of 333 kHz. An external trigger and clocking input are connected to the data acquisition system for acquiring the output voltage of every pixel on the CCD linear image sensor. A triggering system based on a PIC microcontroller, i.e. PIC16F84, is used to coordinate the timing and synchronization between the units in the system.

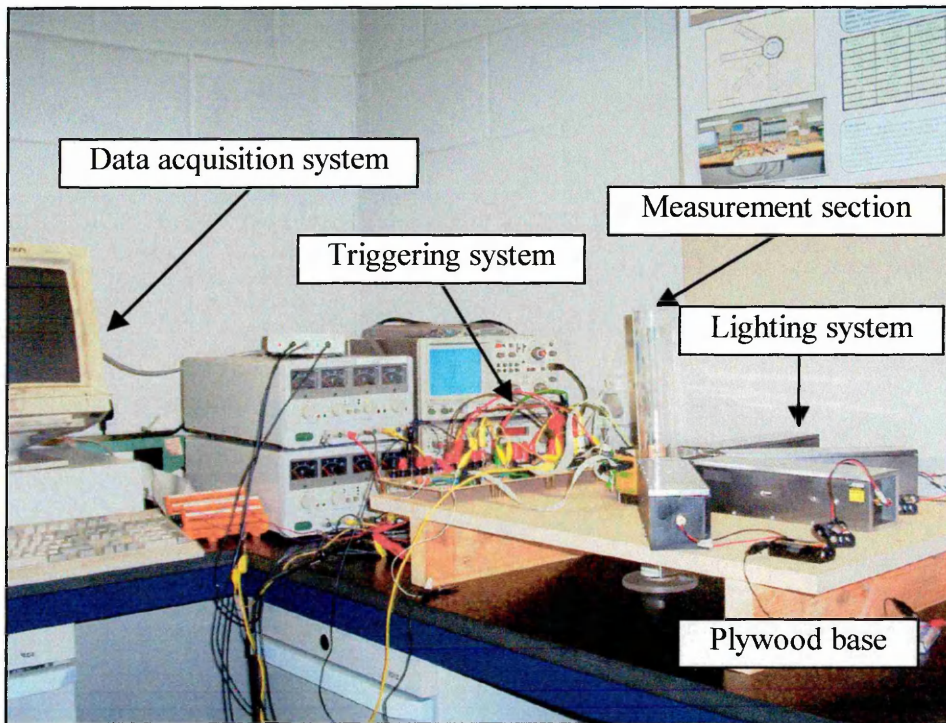


Figure 4.1. Photograph of a complete optical tomography system with four projections.

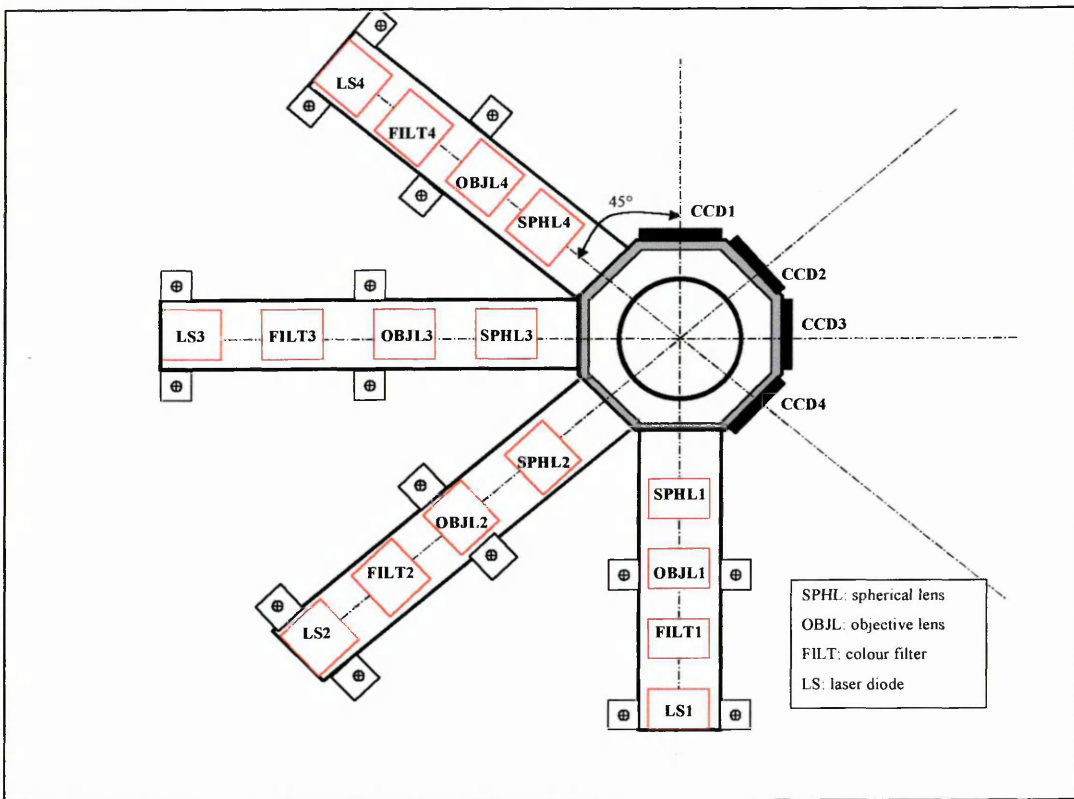


Figure 4.2. The measurement section of the optical tomography system.

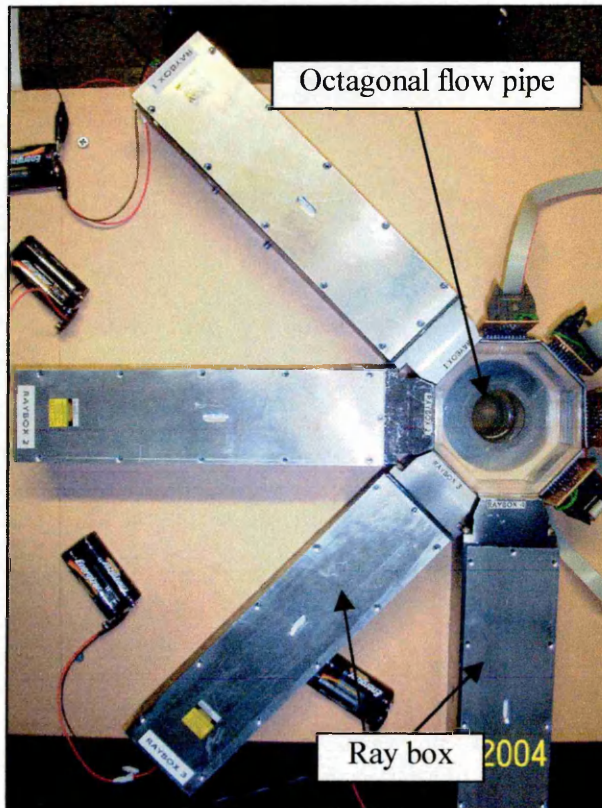


Figure 4.3. Photograph of the measurement section.

4.2 Experimental set-up

Figure 4.4 shows the experimental set-up used to measure the size of the test samples in a single projection. The surfaces of the flow pipe (the octagonal portion) not being traversed in the measurement are covered with black card to minimise reflections due to scattering within the measurement cross-section. The octagonal part of the flow pipe enables four projections of the tomographic system to be assembled around the pipe, with four pairs of the illumination-detection system arranged opposite to each other.

The four-projections tomographic system is shown in Figure 4.5 where the system is mounted on a plywood base to ensure that the system is stable. The whole rig is elevated to allow liquid used in the pipe to be collected from the bottom.

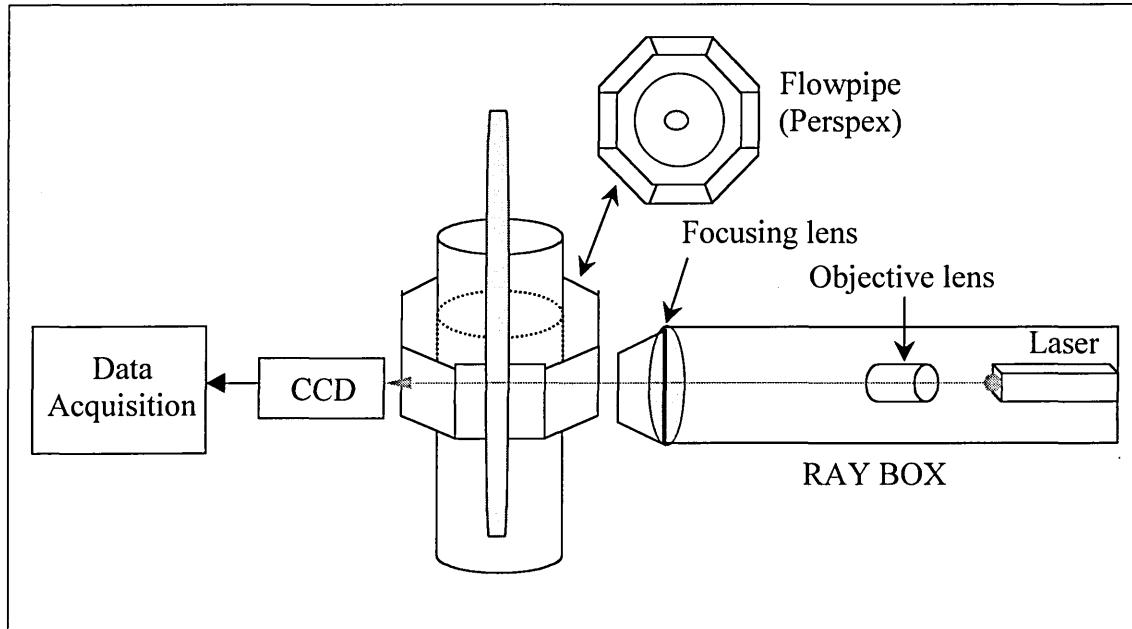


Figure 4.4. The experimental set-up (single projection).

The four ray-boxes are arranged surrounding the hexagon part of the pipe with the corresponding CCD linear image sensors on the opposite side. Individual CCD drivers are connected to each of the CCD linear image sensors used (Figure 4.6). The individual sub units are now described in detail.

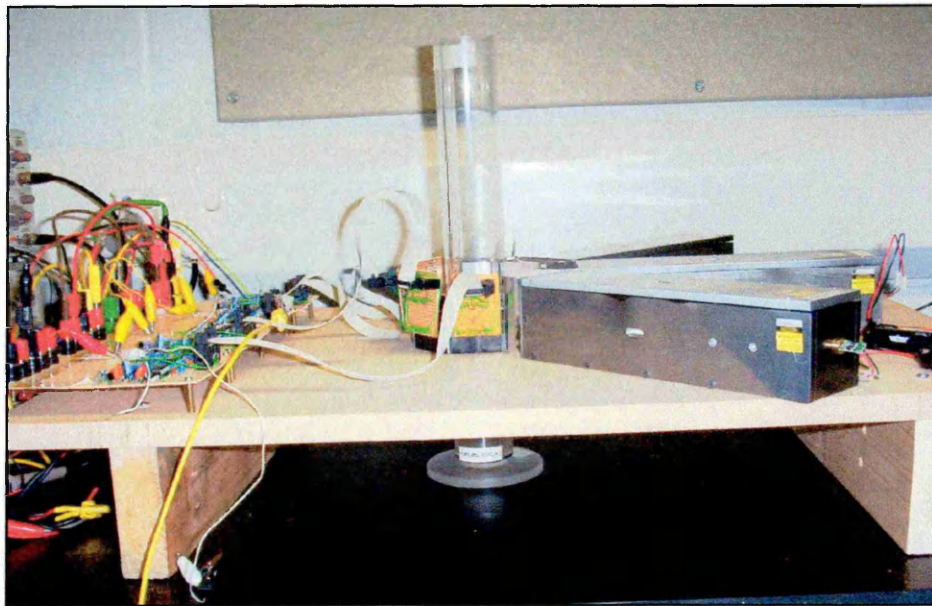


Figure 4.5. A photograph of a four-projections tomographic system.

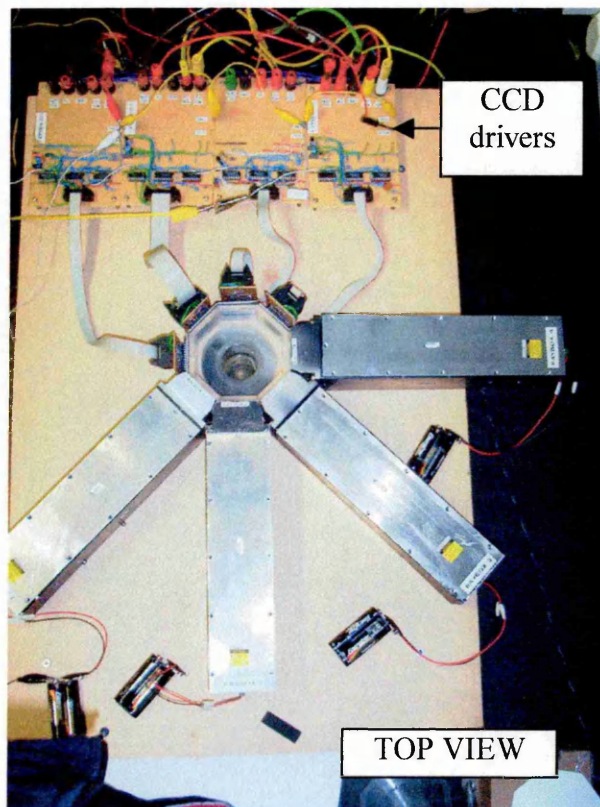


Figure 4.6. A photograph of the CCD drivers of the tomographic system.

4.2.1 The illumination system

The illumination system is assembled in a metal box called a ray-box. There are four identical ray-boxes for the whole system. Each ray-box consists of a laser module, an objective lens and a spherical lens. Figure 4.7 shows the top and side views of the ray-box. The ray-box consists of two parts – the main body and the ‘nose’.

The main body is shown in Figure 4.8 with a hole for the laser module on the left side of the box (Figure 4.10) and the objective lens holder in the middle. The spherical lens is positioned on the right in between the main body and the ‘nose’ (Figure 4.9). The slit can be seen at the far end of the ‘nose’ which is shown in Figure 4.9. The objective lens (beam expander) is located in a holder (Figure 4.11b) which can be moved vertically and horizontally by adjustment screws with respect to the aluminium body of the holder (Figure 4.11a). This enables it to be centralised on the laser beam. The objective lens holder can be moved axially to optimise the beam collimation.

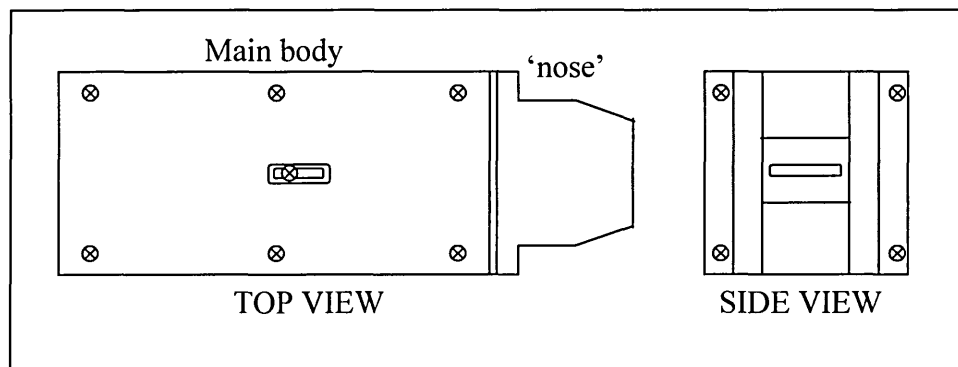


Figure 4.7. The top and side views of the ray-box.

Before mounting the lens and final assembly, all parts of the ray box are painted matt black to minimise scattering and internal reflection of light which could produce a less collimated beam.

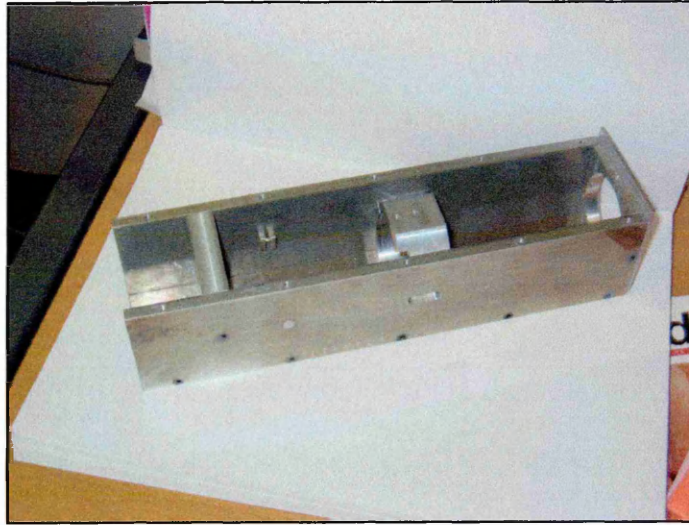


Figure 4.8. The main body of the ray-box.



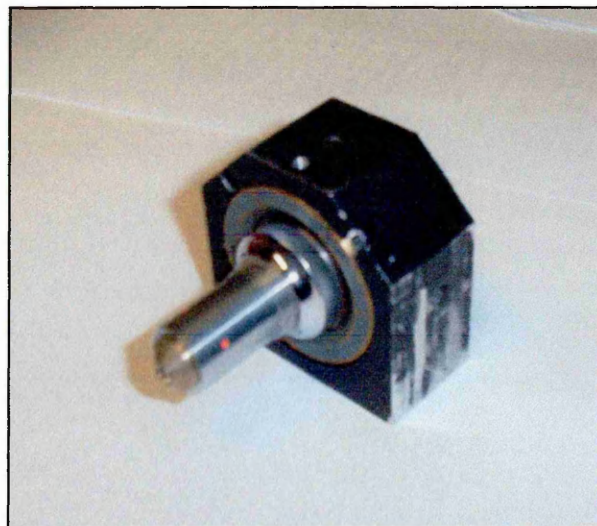
Figure 4.9. The 'nose' of the ray-box.



Figure 4.10. The laser module holder.



(a)



(b)

Figure 4.11. The objective lens holder.

Test on the ray-box

The ray-box is tested for two factors – uniformity in intensity and collimated illumination. For the first test (uniform intensity), a Fibre Optic Power Meter is used where the input probe of the meter is positioned along the slit of the ‘nose’ (Figure 4.12). The brightness of the light is reasonably uniform along the slit, ranging from 33.1 to 34.5 dBm.

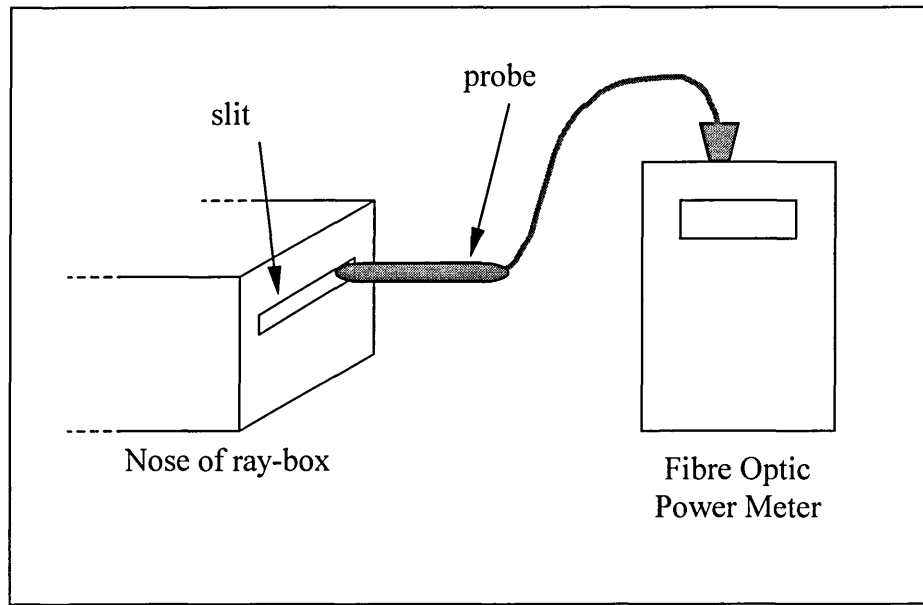


Figure 4.12. Test on uniform intensity.

The test on collimated illumination is performed by observing the diameter of the light coming out from the ‘nose’ (with the slit part taken out). The light beam is circular in shape with a diameter of 30 mm. A circle of similar diameter is drawn on a white card used to trace the light dimension. As the card is moved farther from the ray-box along an optical bench, the circular shape of intensity remains almost constant i.e. the beam is collimated.

4.2.2 The CCD detection system

The sensor used in the optical tomography system is a charge coupled device (CCD) linear image sensor – Sony ILX551A. The linear image sensor is capable of scanning only a line of an object compared to an area image sensor, which can capture or scan a specific area depending on the size of the image sensor. However, the linear image sensor is relatively low cost and produces a high definition line scan which is readily transferred to a computer for further analysis.

The Sony ILX551A is a 22-pin DIP linear image sensor (Figure 4.13) with a built-in timing generator and clock-drivers ensuring direct drive at 5 volts logic for easy use. It also has the following features:

- Number of effective pixels: 2048 pixels
- Pixel size: 14 micron by 14 micron (14 micron pitch)
- Built-in timing generator and clock drivers
- Maximum clock frequency: 5 MHz

The block diagram of the CCD linear image sensor is as in Figure 4.14.

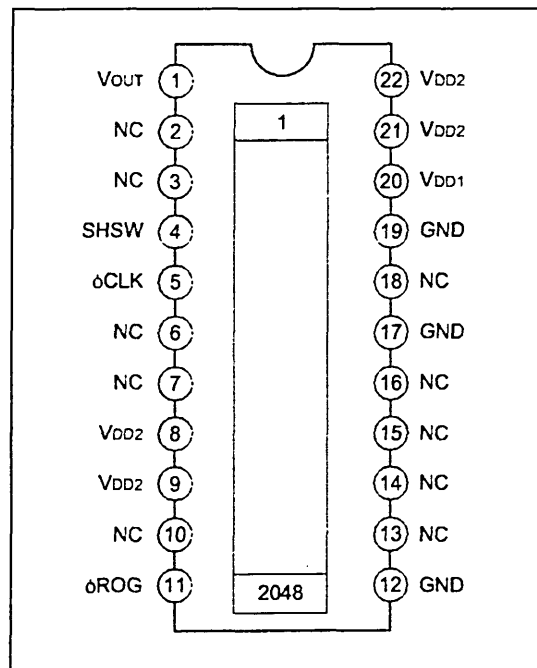


Figure 4.13. The pin configuration of the Sony ILX551A.

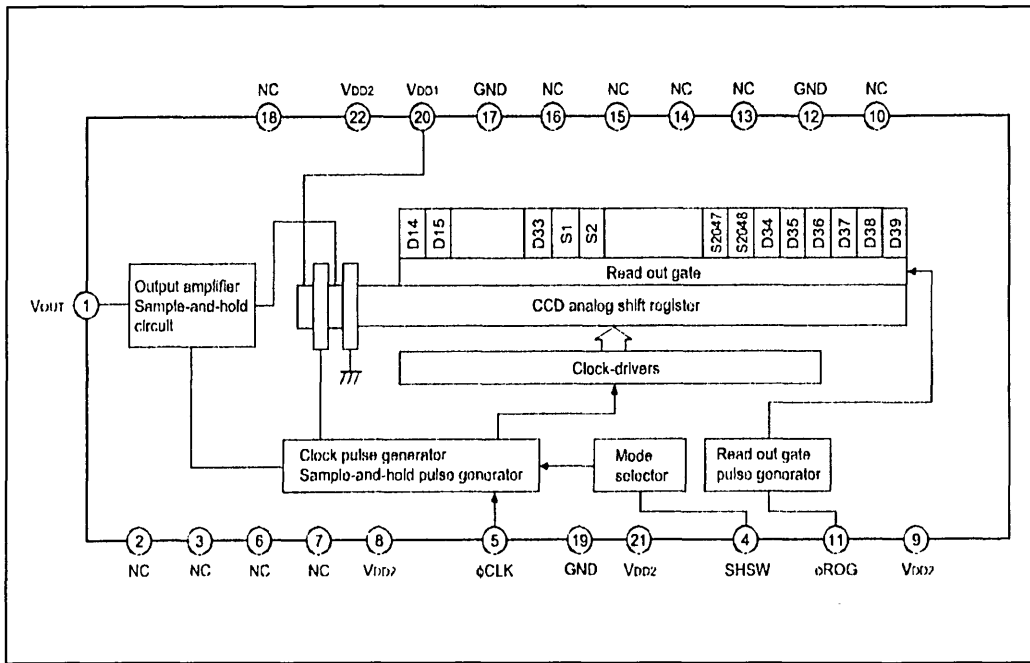


Figure 4.14. A block diagram of Sony ILX551A.

4.2.2.1 Driver for the CCD linear image sensor

The CCD linear image sensor requires two externally generated control inputs namely ϕ ROG and ϕ CLK. The timing diagram for ϕ ROG, ϕ CLK and V_{OUT} is shown in Figure 4.17 whilst detailed timing for ϕ CLK – V_{OUT} and ϕ ROG – ϕ CLK are shown in Figure 4.15 and 4.16, respectively.

Basically, the output of the CCD linear image sensor i.e. V_{OUT} is first acquired when ϕ ROG is logic LOW whilst ϕ CLK is logic HIGH. When ϕ ROG is logic LOW and ϕ CLK is logic HIGH, the CCD is active and the image is built up on the CCD element. When ϕ ROG is logic HIGH, the CCD information is stored and 2087 analogue voltages are clocked out to the data acquisition system via V_{OUT} as ϕ CLK goes HIGH. Hence a series of samples on the CCD output is triggered on every positive edge of ϕ CLK.

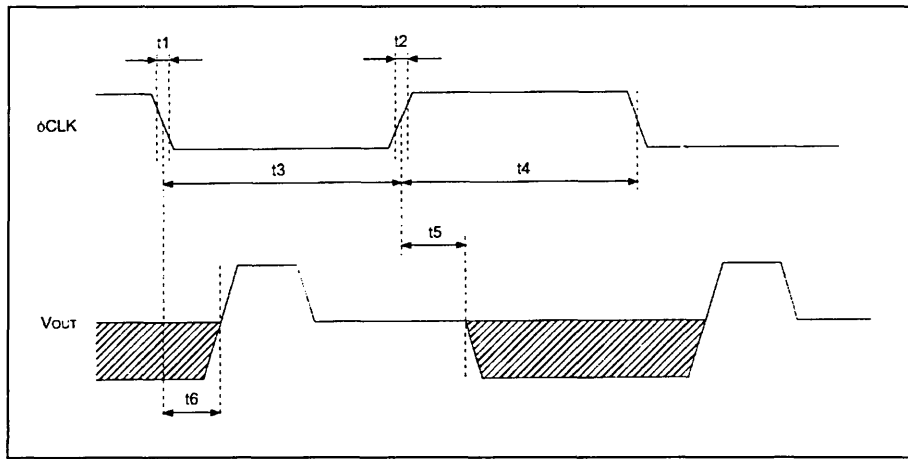


Figure 4.15. Timing diagram for $\phi\text{CLK} - V_{\text{OUT}}$.

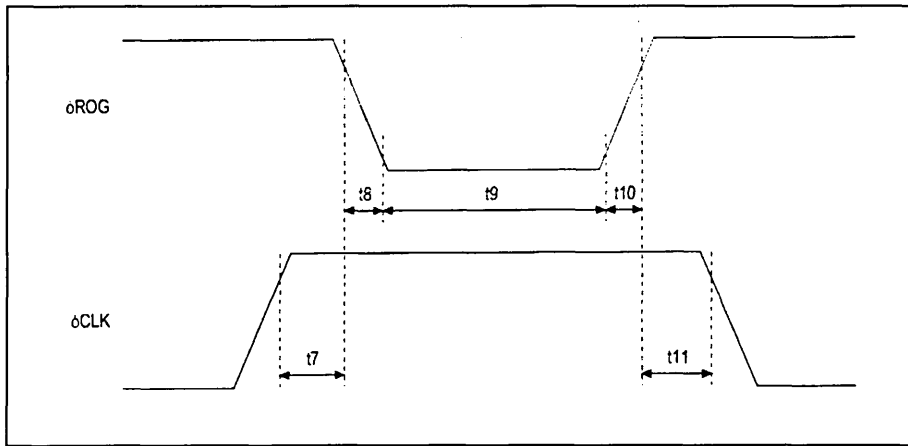


Figure 4.16. Timing diagram for $\phi\text{ROG} - \phi\text{CLK}$.

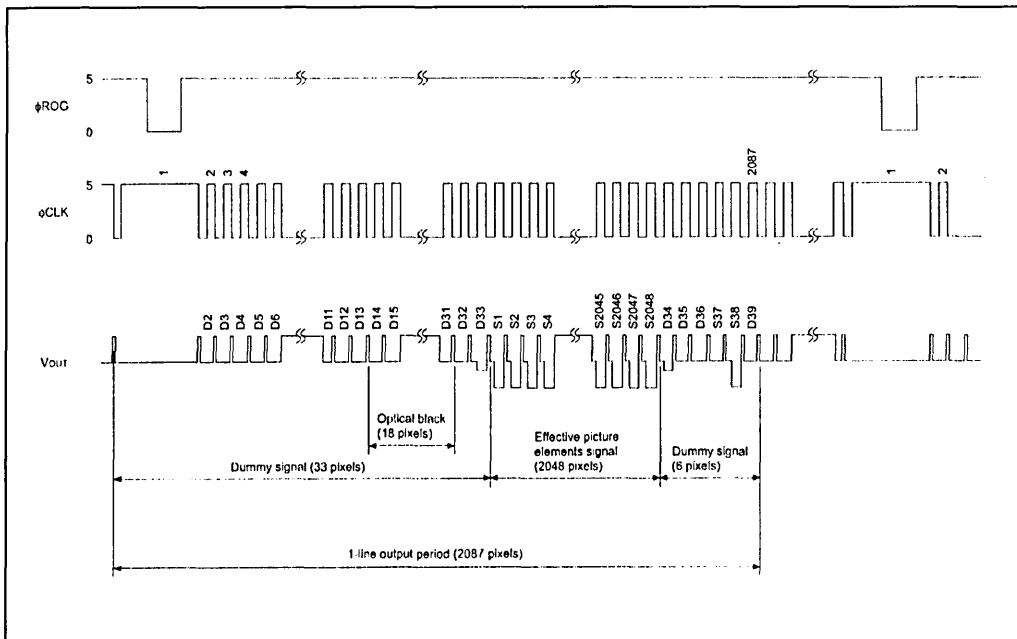


Figure 4.17. Timing diagram for ϕROG , ϕCLK and V_{OUT} .

4.2.2.2 Hardware of the CCD driver

A circuit diagram for the driver of the CCD linear image sensor is shown in Figure 4.18. The ϕ ROG function is built using a one-shot multivibrator whilst the ϕ CLK function is built by OR-ing another one-shot multivibrator with a square-wave function generator to enable changes in the clock frequency. The frequency of ϕ CLK needs to be adjusted to ensure compatibility of the CCD system with the existing data acquisition system (Keithley DAS-1800HC). The Keithley DAS system limits the maximum clock frequency to 333 kilohertz.

In order to read the output voltage of the CCD linear image sensor, the ϕ ROG should be pulsed LOW whilst the ϕ CLK is pulsed HIGH as in the specification of the timing diagram shown in Figure 4.16. The ϕ ROG is then pulsed HIGH during the shifting out of the acquired output (2087 pixels). The designed ϕ ROG and ϕ CLK signals are shown in Figure 4.19 and Figure 4.20, respectively. Figure 4.21 shows the relationship between the two signals (ϕ ROG- ϕ CLK).

V_{OUT} consists of a series of output data for 2100 pixels depending on the type of CCD sensor used. The amount of data on the V_{OUT} is controlled by a TRIGGER function with an adjustable time period per clock cycle. For example 2100 pixels requires 2.1 milliseconds per clock cycle when 1 MHz clock frequency is used (2100 pixels multiplies 1 microsecond/pixel). Since the Keithley-DAS acquisition system can operate at the maximum frequency of 333 kHz, the designed system is operated at a frequency of 250 kHz. Hence, the overall system is clocked at approximately 8.4 milliseconds per clock cycle.

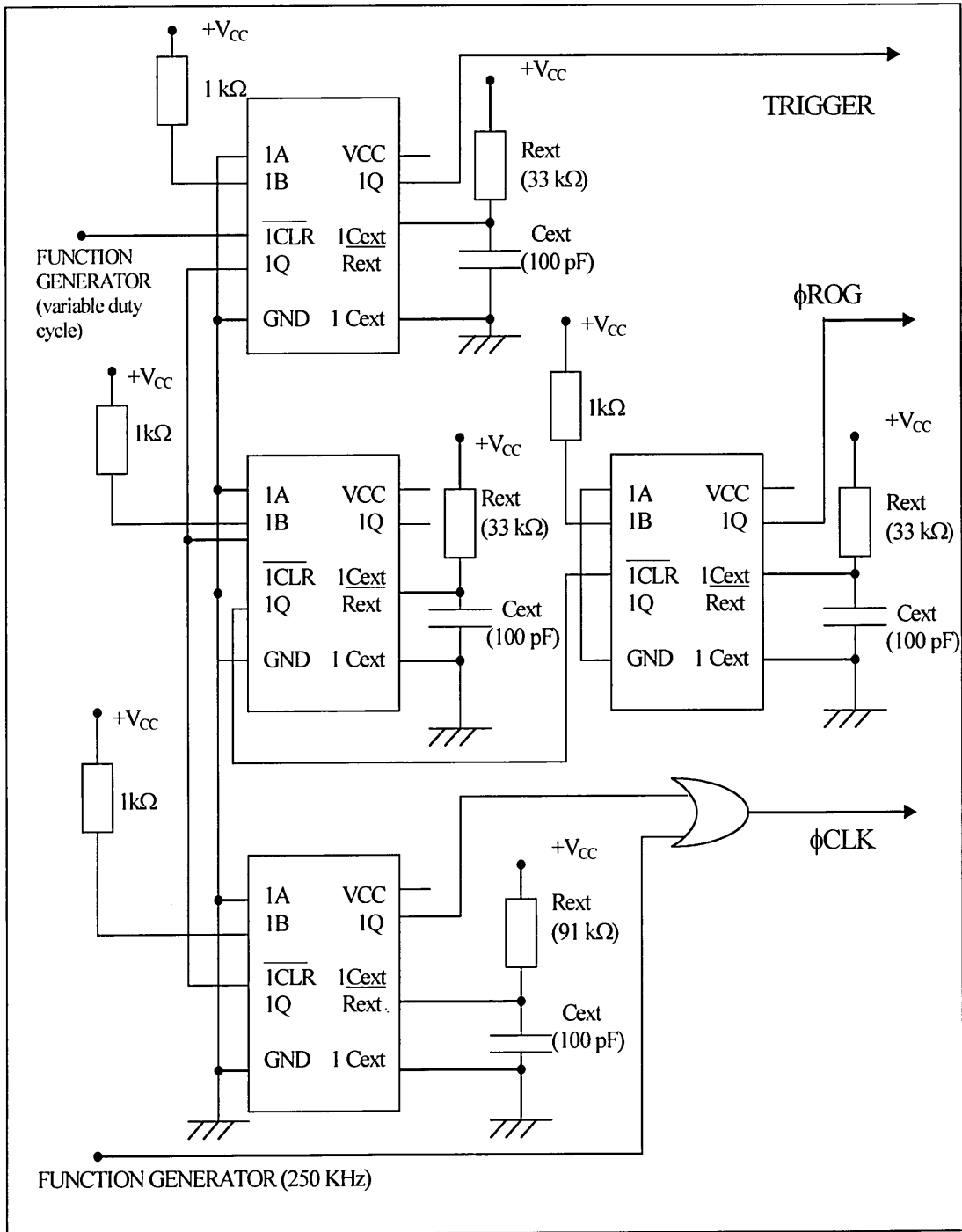


Figure 4.18. A circuit diagram for CCD linear sensor's driver.

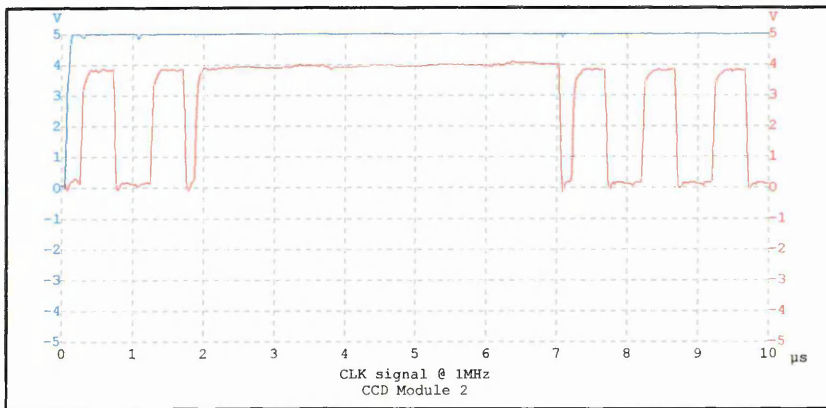


Figure 4.19. The ϕ CLK signal from the triggering circuit.

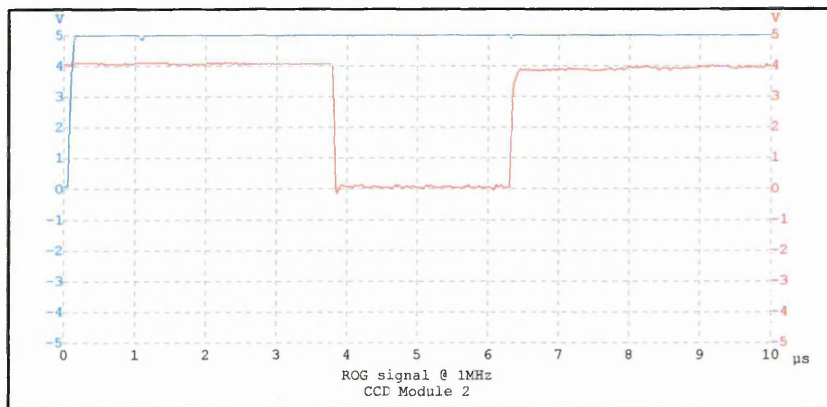


Figure 4.20. The ϕ ROG signal from the triggering circuit.

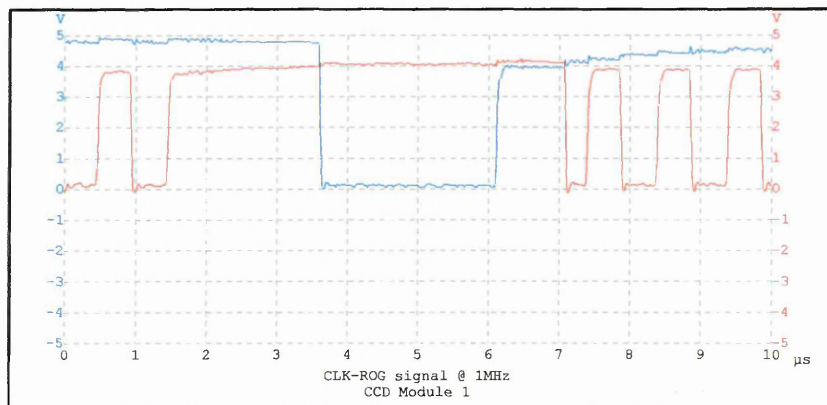


Figure 4.21. The ϕ ROG- ϕ CLK signals from the triggering circuit.

4.2.2.3 Triggering circuit: PIC16F84

All four of the CCD modules need to be synchronised and clocked sequentially. This operation is performed using the PIC16F84 microcontroller. Ideally, the CCD modules should be triggered simultaneously in order to obtain real time images of the particle. However, the light beam illuminated by four of the laser modules saturates the CCD linear sensor when the operation is done at the same time. Therefore, each of the laser modules is activated sequentially. The timing diagram for the CCD modules is shown in Figure 4.22.

Tests show that, for a specific linear image CCD sensor, the 'dark region' (see Section 3.3.1) in the shadow of the particle is reduced when more than one ray box is enabled. This is probably due to light from other projections being scattered and illuminating the 'wrong' sensor. The contrast is maximised by activating each of the lasers sequentially.

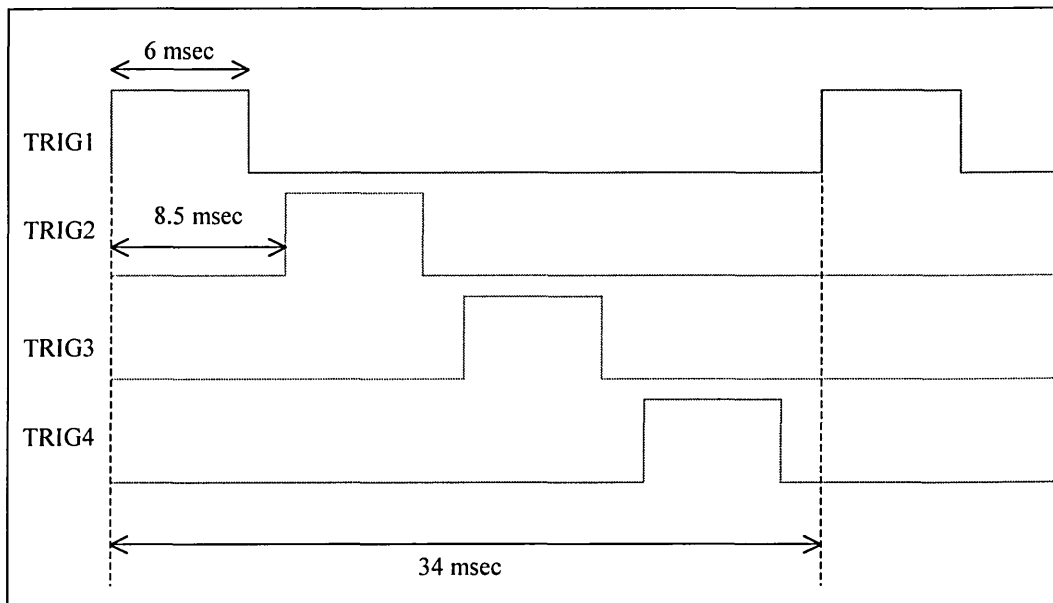


Figure 4.22. The timing diagram for the CCD modules.

The CCD linear image sensor is still operated in the saturation mode when the laser module is ON for one clock cycle i.e. 8.5 ms. This operation is performed at the frequency of 250 kHz and 8.4 ms is required to acquire 2100 pixels (2100 pixels multiplies 1/250 ms). Experimentally, t_{ON} of the laser module is increased gradually (with a known particle diameter in the pipe) in order to obtain the optimal time. The results show that the measured value of the particle's diameter has the least error when t_{ON} is at 6.0 ms to 6.2 ms. This time-range is used for the overall measurement process. Figure 4.23 shows the difference in the CCD output voltage due to the particle when t_{ON}

is 6.0 ms (red line) and 8.5 ms (blue line), respectively. The output signal is noisier and larger when the laser module is on for 8.5 ms than with a t_{ON} of 6.0 ms. When the time base is converted into equivalent length (1pixel = 0.014 mm), the size percentage of error is 16% for ON time of 8.5 ms and 2% for 6.0 ms.

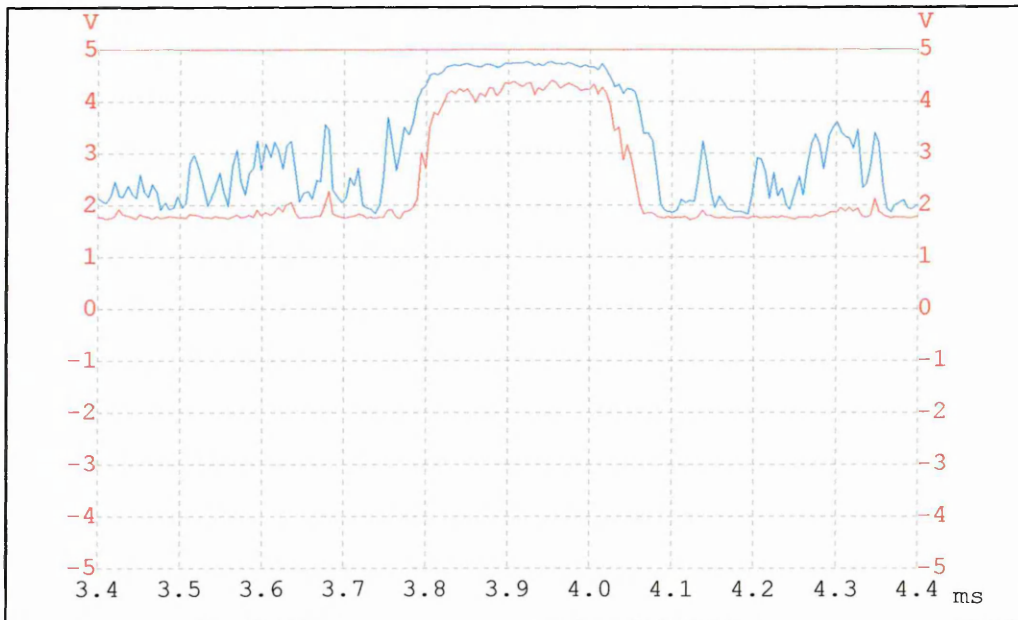


Figure 4.23. The output images of a particle when t_{ON} is 6 ms (red line) and 8.5 ms (blue line).

Careful timing of the CCD linear image sensor and the laser module is important to ensure that the laser module is already ON when the CCD linear image sensor starts reading the output signals from each of the pixels. The read-out gate input or ϕ_{ROG} is triggered when the laser module has reached the full illumination mode. Figure 4.24 shows the circuit diagram of the triggering system using the PIC16F84 microcontroller. The algorithm of the PIC16F84 is shown in Figure 4.25.

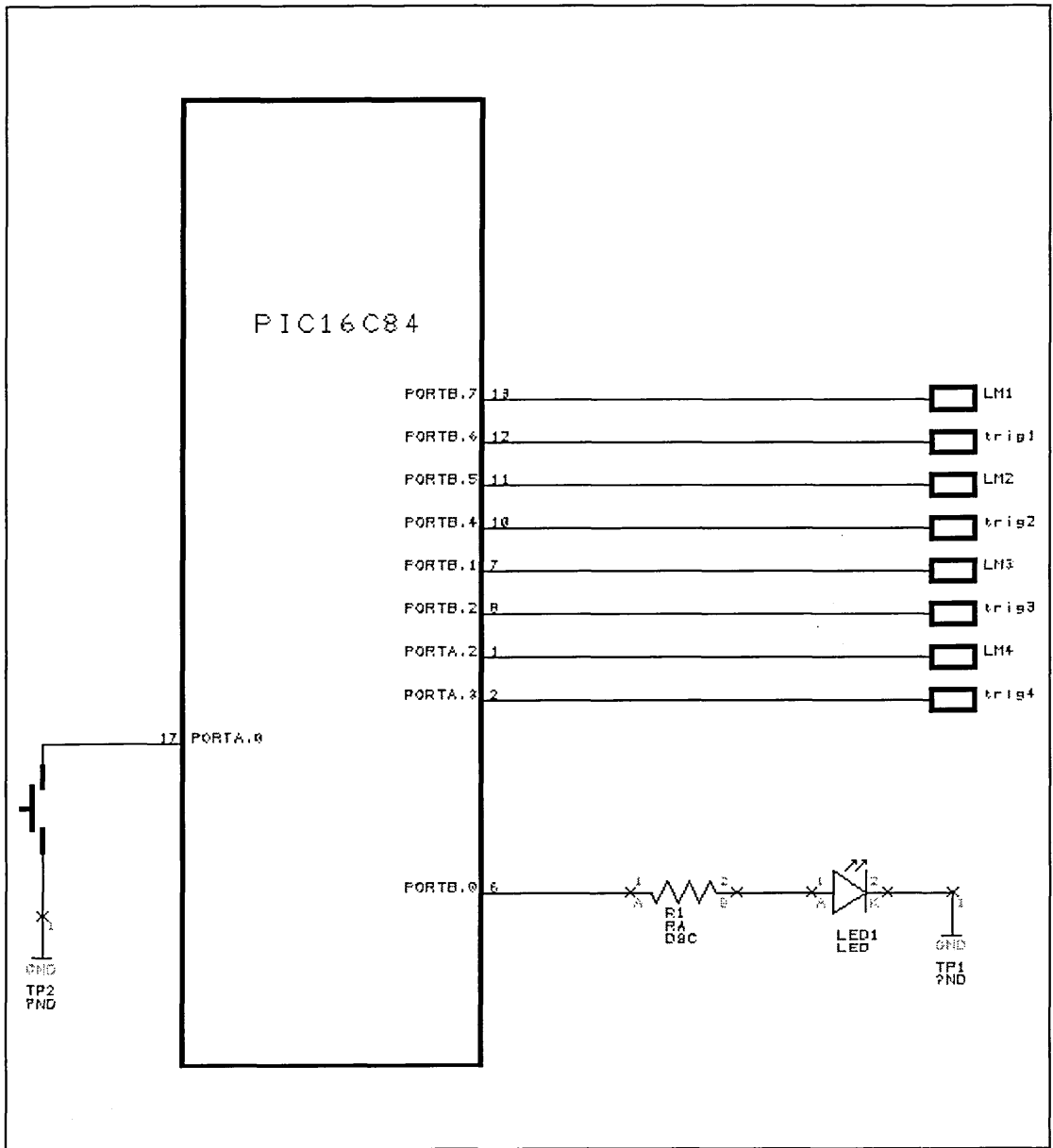


Figure 4.24. The triggering circuit.

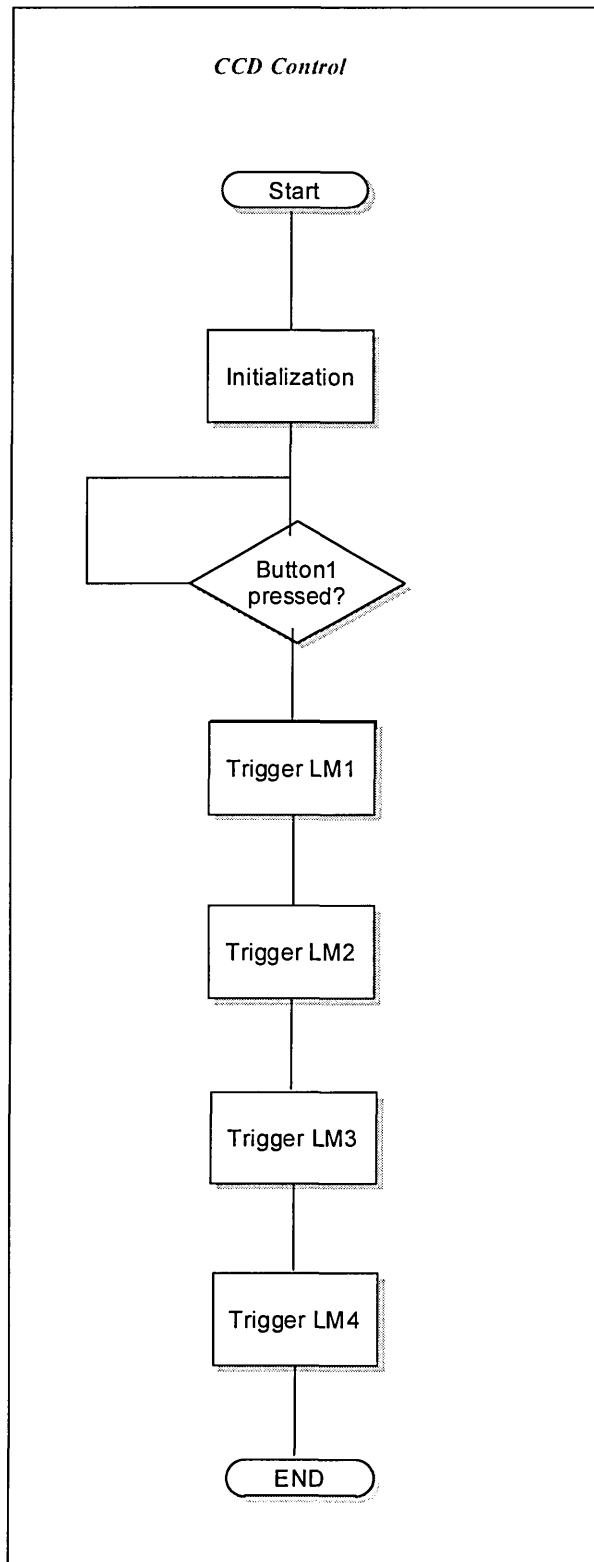


Figure 4.25. The flowchart of the PIC16F84.

4.3 Switching the laser module.

The laser module and the CCD triggering circuit need to be synchronised. The laser is switched on and the CCD linear sensor is enabled a few microseconds later. A basic switching circuit is based on a 3904NPN transistor and the schematic diagram is shown in Figure 4.26.

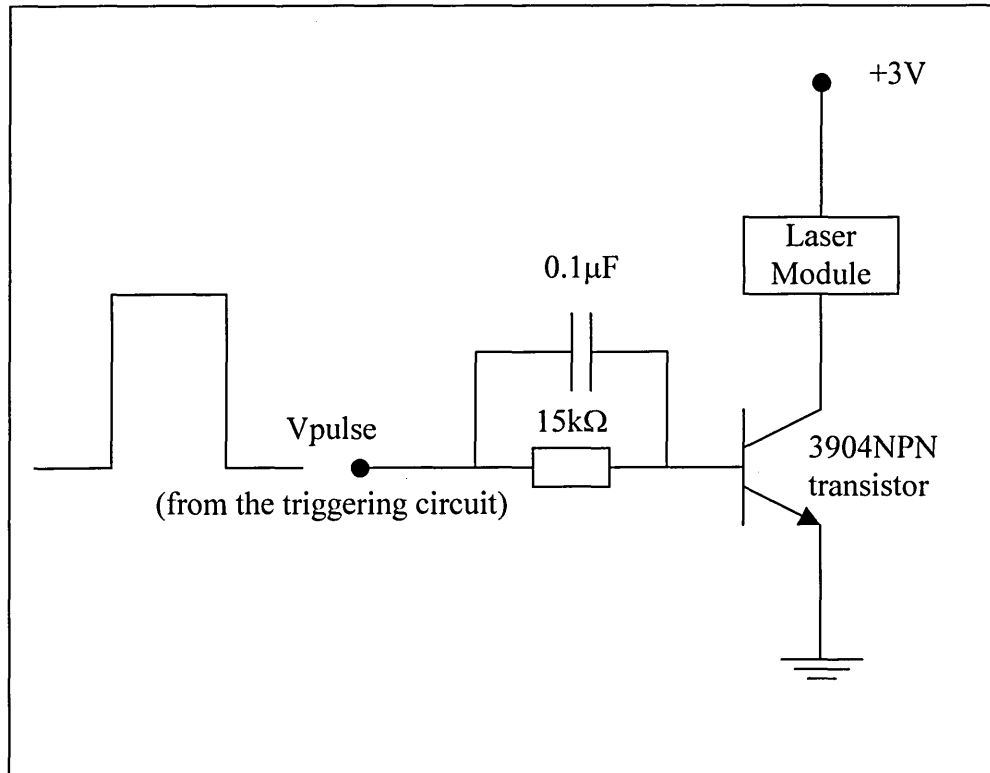


Figure 4.26. The switching circuit of the laser module.

A capacitor is placed parallel with the current limiting resistor to speed up the switching of the laser module.

4.5 Discussions

This chapter covers the hardware development of the optical tomography system – the illumination system (ray-box), the CCD detection system, the triggering circuit (based on the PIC16F84 microcontroller and the switching circuit. Two tests are performed on the illumination system to ensure uniform intensity and collimated illumination fall on the CCD linear image sensors. The triggering circuit is important in coordinating the synchronisation of each unit in the optical tomography system. This is done using the PIC16F84 microcontroller due to its flexibility in program modification.

CHAPTER 5

OPTICAL TOMOGRAPHIC IMAGE RECONSTRUCTION

5.1 Introduction

Image reconstruction is a process of generating an image from raw data, or a set of unprocessed measurements, made by the imaging system. In general, there is a well-defined mathematical relationship between the distribution of physical properties in an object and the measurements made by the imaging system. Image reconstruction is the process which inverts this mathematical process to generate an image from the set of measurements [Xie, 1995].

In an optical imaging system, the object density along the optical path (according to Beer-Lambert Law) exponentially attenuates the light intensity,

$$I_{out} = I_{in} e^{-\alpha x} \quad (5.1)$$

$$\ln\left(\frac{I_{in}}{I_{out}}\right) = \alpha x \quad (5.2)$$

where α is the linear attenuation coefficient and x is the distance the light traverses. The natural logarithm of the ratio of the incident intensity to the transmitted intensity is equal to the line integral or ray sum of the distribution of linear attenuation coefficients within the object along the path. An image of the object density distribution can be created using a projection reconstruction algorithm.

The optical tomography system consists of four projection systems where each projection is generated by a ray-box which has the laser diode, the objective lens, and the spherical lens in it (see Section 4.2.1) and the CCD linear image sensor at the other side of the pipe. The CCD linear image sensor used in the system has 2048 effective pixels with a pixel size of 14 micron by 14 micron (refer Section 4.2.2).

As a result, the tomographic image consists of four projections, with each providing 2048 measurements. The complete forward problem requires 2048 by 2048 values of α (attenuation coefficient) to model the system. The image reconstruction process for the system is modelled using smaller m by n arrays of pixels to make the problem solvable using a personal computer (PC). This approach reduces the processing time and enables a better understanding of the impact of each technique when applied to the actual system.

To explain the forward problem simply the object space is considered to consist of a 7×7 array of cells projected onto a circular measurement cross-section, later this is extended to the 2048×2048 array. The analysis is for four projections (Figure 5.5). For the inverse problem several different arrangements are investigated. These include three projections on a 3×3 array of cells, four projections on a 4×4 array cells and two, three and four projections on a 7×7 array of cells. This analysis aims to compare the effects of using pseudo inverse and transpose of the sensitivity matrix.

A simple optical attenuation model is used to model the measurement system. The model uses an array of octagonal shaped cells with square cells to ensure that the light traverses through all cells normally (Figure 5.1). Moreover, the arrangement of cells based on the octagon and square shape simplify the matrix manipulation in the image reconstruction process. The light beam width is assumed to be 0.006 mm i.e. passes through the square cell and the octagonal cell normally. In this case, the octagonal cell has four projections whilst the square cell has only two projections. However, the effect of the pixel shapes on the reconstructed image is not significant in the actual system due to its large number of pixels (2048×2048 pixels) and small particles of interest (100 micron up to 10 mm diameter particles).

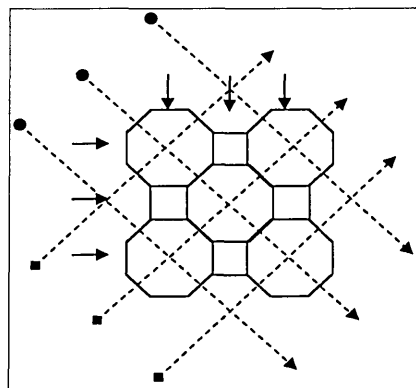


Figure 5.1. Four projections on 3×3 cells.

The dimension of each side of the octagonal cell is calculated as follows (refer to Figure 5.2).

$$\tan 22.5^\circ = (x/2) / 0.007 \quad (5.3)$$

$$x = 0.014 (\tan 22.5^\circ) = 0.0058 \text{ mm} \approx 0.006 \text{ mm} \quad (5.4)$$

The actual measurement of the octagonal and square cells is shown in Figure 5.3.

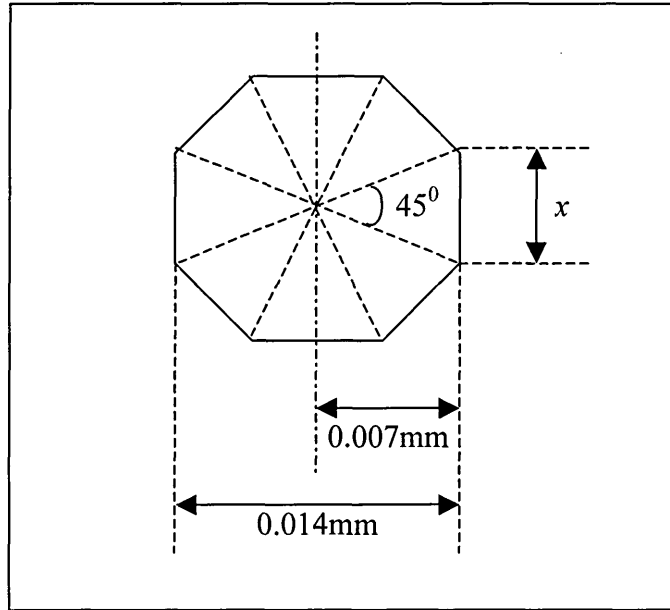


Figure 5.2. An octagonal shaped cell.

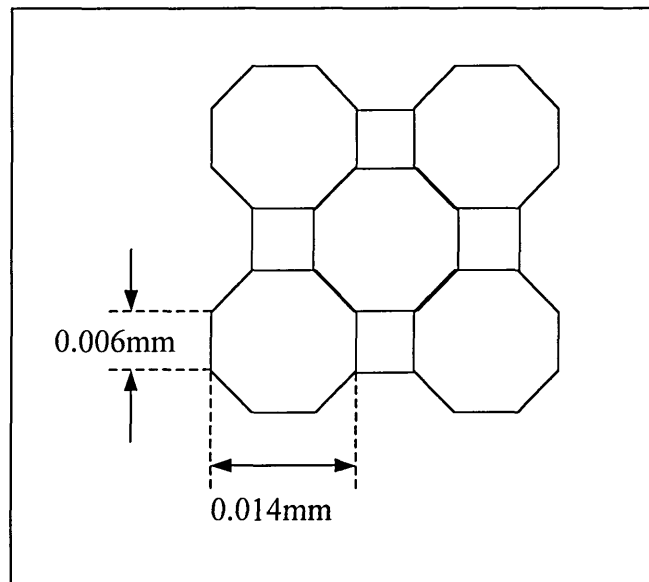


Figure 5.3. Actual measurements of octagonal-square shaped cells.

The optical attenuation model (based on the combination of octagonal-square shaped cells) is used in the forward problem. These cells are used in the formation of the sensitivity matrix for the image reconstruction process (Section 5.2.1). However, the reconstructed image from the inverse problem has square image pixels due to the standard format of a matrix. The pixel size is 0.014 mm by 0.014 mm for the actual reconstructed image system (2048x2048 array).

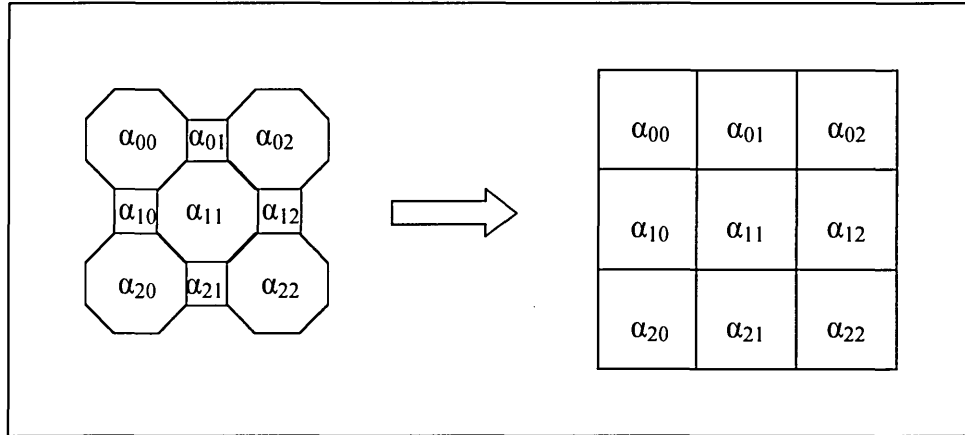


Figure 5.4. Transformation of octagonal-square cells into square image pixels.

5.2 Image reconstruction process

Several techniques have been used in optical tomography to produce images from measured data, such as layergram backprojection (LYGBP) by Ibrahim [1999], linear backprojection (LBP) by Abdul Rahim [1996], Algebraic reconstruction technique (ART) by Reinecke and Mewes [1994], iteration techniques, Fourier inversion techniques and others [Herman GT, 1980]. Xie [1993] highlighted techniques used in transmission tomography such as optical and X-ray, which are based on the straight-line propagation.

The forward problem has to be performed first in order to obtain the expected output from the sensors (for known attenuation coefficients of water and the particle). The calculated output from the forward problem is then used in the backprojection process – the inverse problem.

5.2.1 Forward problem

In this project, the particle may be translucent or opaque and is a solid surrounded by water. The particle used in the modelling analysis is considered to have a linear attenuation coefficient of 10 mm^{-1} . To explain the forward problem process, the area to be imaged in the pipe is divided into 49 cells (7x7 array of cells) for simplicity. Later in this section the model is extended to a 2048x2048 array of cells. The reconstructed image of the particle in water is based on four projections. The arrangement of cells is shown in Figure 5.5.

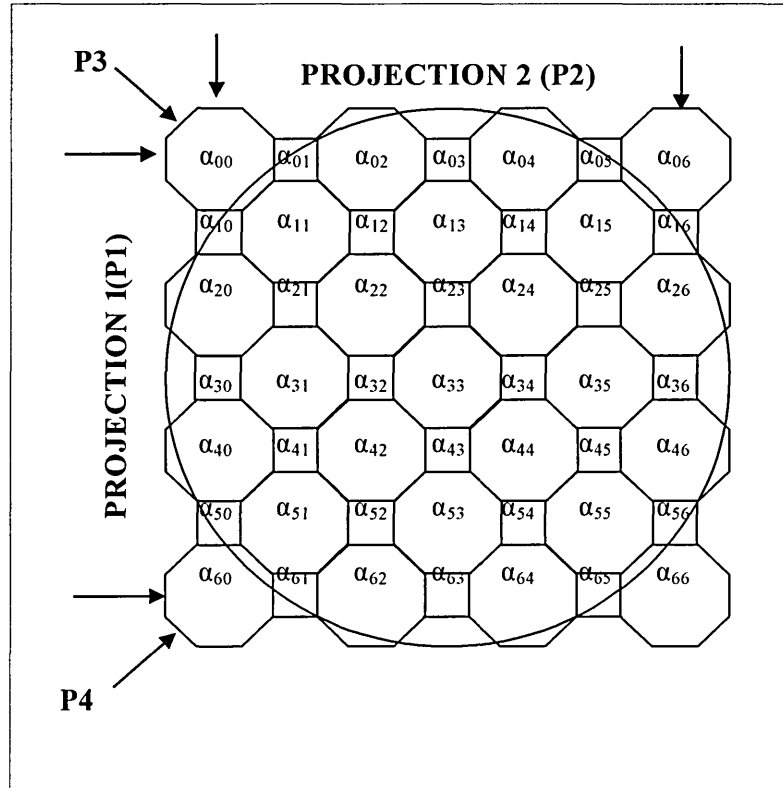


Figure 5.5. 7x7 array of pixels with four projections.

From Figure 5.5 each projection has seven optical sensors and hence the total number of sensors for four projections (P1 to P4) is twenty-eight which provide twenty-eight measurements - M1 to M28. There are up to seven cells associated with each sensor when the incoming light passes through the pipe. The linear attenuation of the light is modelled by assuming that each cell has an attenuation coefficient of α_{ij} where i and j represent the row and column, respectively. The length of the octagon pixel is 0.014 mm whilst the length of the square pixel is 0.006 mm. The change in light intensity measured by the sensors may be written

$$\ln\left(\frac{\text{constant}}{I_{out}}\right)_n = M_n \quad \text{where } n = 1 \text{ to } 28.$$

Based on the Beer-Lambert Law of absorption (equation 1 and 2), the horizontal equations (i.e. projection 1) for each sensor are (Equations 5.5 to 5.11):

$$\begin{aligned}\alpha_{00}(0.014) + \alpha_{01}(0.006) + \alpha_{02}(0.014) + \alpha_{03}(0.006) + \alpha_{04}(0.014) + \alpha_{05}(0.006) + \alpha_{06}(0.014) &= M_1 \\ \alpha_{10}(0.006) + \alpha_{11}(0.014) + \alpha_{12}(0.006) + \alpha_{13}(0.014) + \alpha_{14}(0.006) + \alpha_{15}(0.014) + \alpha_{16}(0.006) &= M_2 \\ \alpha_{20}(0.014) + \alpha_{21}(0.006) + \alpha_{22}(0.014) + \alpha_{23}(0.006) + \alpha_{24}(0.014) + \alpha_{25}(0.006) + \alpha_{26}(0.014) &= M_3 \\ \alpha_{30}(0.006) + \alpha_{31}(0.014) + \alpha_{32}(0.006) + \alpha_{33}(0.014) + \alpha_{34}(0.006) + \alpha_{35}(0.014) + \alpha_{36}(0.006) &= M_4 \\ \alpha_{40}(0.014) + \alpha_{41}(0.006) + \alpha_{42}(0.014) + \alpha_{43}(0.006) + \alpha_{44}(0.014) + \alpha_{45}(0.006) + \alpha_{46}(0.014) &= M_5 \\ \alpha_{50}(0.014) + \alpha_{51}(0.006) + \alpha_{52}(0.014) + \alpha_{53}(0.006) + \alpha_{54}(0.014) + \alpha_{55}(0.006) + \alpha_{56}(0.014) &= M_6 \\ \alpha_{60}(0.014) + \alpha_{61}(0.006) + \alpha_{62}(0.014) + \alpha_{63}(0.006) + \alpha_{64}(0.014) + \alpha_{65}(0.006) + \alpha_{66}(0.014) &= M_7\end{aligned}$$

Similarly for the vertical equations (projection 2) for each sensor (Equations 5.12 to 5.18):

$$\begin{aligned}\alpha_{00}(0.014) + \alpha_{10}(0.006) + \alpha_{20}(0.014) + \alpha_{30}(0.006) + \alpha_{40}(0.014) + \alpha_{50}(0.006) + \alpha_{60}(0.014) &= M_8 \\ \alpha_{01}(0.006) + \alpha_{11}(0.014) + \alpha_{21}(0.006) + \alpha_{31}(0.014) + \alpha_{41}(0.006) + \alpha_{51}(0.014) + \alpha_{61}(0.006) &= M_9 \\ \alpha_{02}(0.006) + \alpha_{12}(0.014) + \alpha_{22}(0.006) + \alpha_{32}(0.014) + \alpha_{42}(0.006) + \alpha_{52}(0.014) + \alpha_{62}(0.006) &= M_{10} \\ \alpha_{03}(0.006) + \alpha_{13}(0.014) + \alpha_{23}(0.006) + \alpha_{33}(0.014) + \alpha_{43}(0.006) + \alpha_{53}(0.014) + \alpha_{63}(0.006) &= M_{11} \\ \alpha_{04}(0.006) + \alpha_{14}(0.014) + \alpha_{24}(0.006) + \alpha_{34}(0.014) + \alpha_{44}(0.006) + \alpha_{54}(0.014) + \alpha_{64}(0.006) &= M_{12} \\ \alpha_{05}(0.006) + \alpha_{15}(0.014) + \alpha_{25}(0.006) + \alpha_{35}(0.014) + \alpha_{45}(0.006) + \alpha_{55}(0.014) + \alpha_{65}(0.006) &= M_{13} \\ \alpha_{06}(0.006) + \alpha_{16}(0.014) + \alpha_{26}(0.006) + \alpha_{36}(0.014) + \alpha_{46}(0.006) + \alpha_{56}(0.014) + \alpha_{66}(0.006) &= M_{14}\end{aligned}$$

Projection 3 (Equations 5.19 to 5.25):

$$\begin{aligned}\alpha_{06}(0.014) &= M_{15} \\ \alpha_{04}(0.014) + \alpha_{15}(0.014) + \alpha_{26}(0.014) &= M_{16} \\ \alpha_{02}(0.014) + \alpha_{13}(0.014) + \alpha_{24}(0.014) + \alpha_{35}(0.014) + \alpha_{46}(0.014) &= M_{17} \\ \alpha_{00}(0.014) + \alpha_{11}(0.014) + \alpha_{22}(0.014) + \alpha_{33}(0.014) + \alpha_{44}(0.014) + \alpha_{55}(0.014) + \alpha_{66}(0.014) &= M_{18} \\ \alpha_{20}(0.014) + \alpha_{31}(0.014) + \alpha_{42}(0.014) + \alpha_{53}(0.014) + \alpha_{64}(0.014) &= M_{19} \\ \alpha_{40}(0.014) + \alpha_{51}(0.014) + \alpha_{62}(0.014) &= M_{20} \\ \alpha_{60}(0.014) &= M_{21}\end{aligned}$$

Projection 4 (Equations 5.26 to 5.32):

$$\begin{aligned}\alpha_{66}(0.014) &= M_{22} \\ \alpha_{64}(0.014) + \alpha_{55}(0.014) + \alpha_{46}(0.014) &= M_{23} \\ \alpha_{62}(0.014) + \alpha_{53}(0.014) + \alpha_{44}(0.014) + \alpha_{35}(0.014) + \alpha_{26}(0.014) &= M_{24} \\ \alpha_{60}(0.014) + \alpha_{51}(0.014) + \alpha_{42}(0.014) + \alpha_{33}(0.014) + \alpha_{24}(0.014) + \alpha_{15}(0.014) + \alpha_{06}(0.014) &= M_{25} \\ \alpha_{40}(0.014) + \alpha_{31}(0.014) + \alpha_{22}(0.014) + \alpha_{13}(0.014) + \alpha_{04}(0.014) &= M_{26} \\ \alpha_{20}(0.014) + \alpha_{11}(0.014) + \alpha_{01}(0.014) &= M_{27} \\ \alpha_{00}(0.014) &= M_{28}\end{aligned}$$

These equations may be written in matrix form.

The matrices shown above can be represented in a form of matrix [S] and matrix [R]:

$$[S][R] = [M] \quad (5.33)$$

where [S] is the sensitivity matrix [28x49], [R] is the matrix of optical attenuation coefficients [49x1] and [M] is the measurement values [28x1]. This approach is now outlined for the full system.

A similar process is performed on the actual tomography system with 2048 horizontal and 2048 vertical cell (2048x2048 array). A simplified diagram of the cell attenuation coefficients is shown in Figure 5.6.

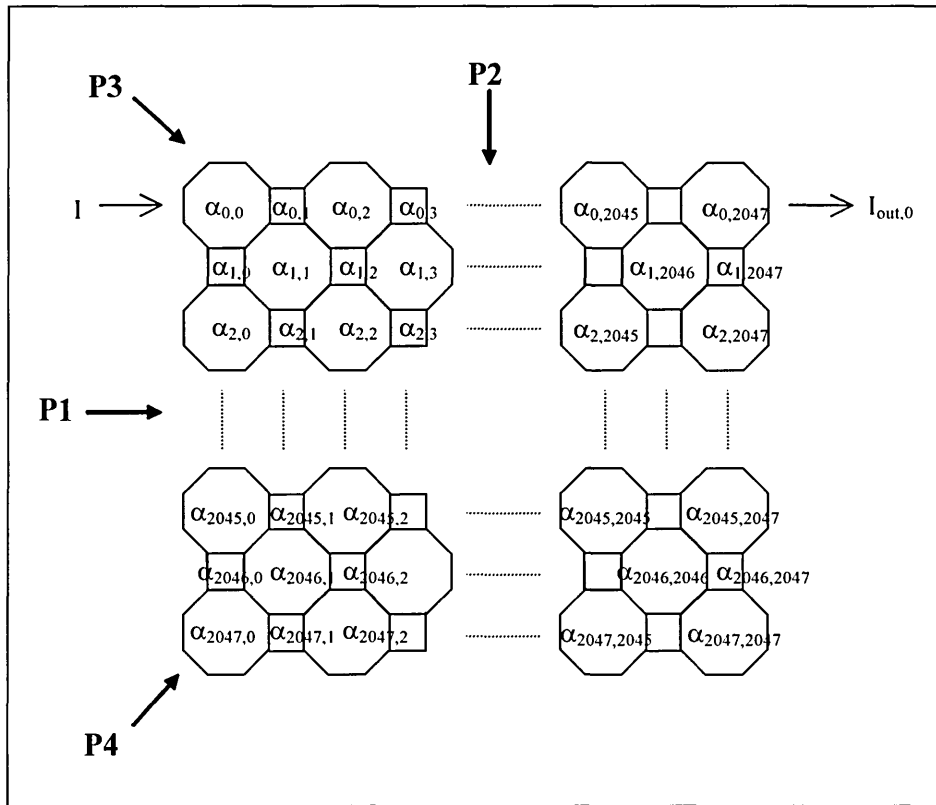


Figure 5.6. 2048 by 2048 array of pixels with four projections.

The equations for each of the projections for the 2048x2048 array (Figure 5.6) – projection 1, 2, 3 and 4 can be expressed in a similar manner to those shown in full for the 7x7 array.

Projection 1:

$$\alpha_{0,0} a + \alpha_{0,1} b + \alpha_{0,2} a + \dots \alpha_{0,2045} a + \alpha_{0,2046} b + \alpha_{0,2047} a = \ln (I/I_{out,0})$$

$$\alpha_{1,0} a + \alpha_{1,1} b + \alpha_{1,2} a + \dots \alpha_{1,2045} a + \alpha_{1,2046} b + \alpha_{1,2047} a = \ln (I/I_{out,1})$$

and so forth until:

$$\alpha_{2047,0} a + \alpha_{2047,1} b + \alpha_{2047,2} a + \dots \alpha_{2047,2045} a + \alpha_{2047,2046} b + \alpha_{2047,2047} a = \ln (I/I_{out,0})$$

Similarly for the vertical equations (projection 2):

$$\alpha_{0,0} a + \alpha_{1,0} b + \alpha_{2,0} a + \dots \alpha_{2045,0} a + \alpha_{2046,0} b + \alpha_{2047,0} a = \ln (I/I_{out,2048})$$

$$\alpha_{0,1} a + \alpha_{1,1} b + \alpha_{2,1} a + \dots \alpha_{2045,1} a + \alpha_{2046,1} b + \alpha_{2047,1} a = \ln (I/I_{out,2049})$$

and so forth until:

$$\alpha_{0,2047} a + \alpha_{1,2047} b + \alpha_{2,2047} a + \dots \alpha_{2045,2047} a + \alpha_{2046,2047} b + \alpha_{2047,2047} a = \ln (I/I_{out,4095})$$

Projection 3:

$$\alpha_{0,2047} a = \ln (I/I_{out,4096})$$

$$(\alpha_{0,2045} + \alpha_{1,2046} + \alpha_{2,2047})a = \ln (I/I_{out,4097})$$

and continue until:

$$\alpha_{2047,0} a = \ln (I/I_{out,6143})$$

Projection 4:

$$\alpha_{2047,2047} a = \ln (I/I_{out,6144})$$

$$(\alpha_{2047,2045} + \alpha_{2046,2046} + \alpha_{2045,2047})a = \ln (I/I_{out,6145})$$

and the same process is repeated until

$$\alpha_{0,0} a = \ln (I/I_{out,8191})$$

The above expressions can be expressed in matrix form,

$$[S]x[R] = [M] \tag{5.34}$$

where $[S]$ is the sensitivity matrix [8192x4194304], $[R]$ is the matrix of attenuation coefficients [4194304x1], and $[M]$ is the measurement values [8192x1].

5.2.2 Inverse problem

In practice, measurements are made and then used to estimate values of the linear attenuation coefficients. Equation (5.34) needs to be re-arranged in order to reconstruct the tomographic image.

$$[R] = [S]^{-1} x[M] \quad (5.35)$$

The main problems associated with the above equation are that the matrix $[S]$ is not square, hence there is no direct inverse and it is also sparse (many of its values are zero). These are the main limitation of the inverse problem because it is not possible to have the number of projections equal to the number of cells involved. Even if the matrix $[S]$ is square, it will be shown later that the inversion is still not possible because the matrix is too sparse. Many references such as Yang *et al* [1999], Xie *et al* [1992], Isaksen and Nordtvedt [1992] and Salkeld [1991] use the transpose of the sensitivity matrix to obtain qualitative information about the permittivity coefficients in Electrical Capacitance Tomography (ECT) measurements. A mathematically rigorous approach is to use the pseudo inverse of the matrix. Therefore, both the transpose and the pseudo-inverse are investigated in order to obtain an estimate of the inverse matrix of S.

$$[R] = [S]^{transpose} x[M] = [S]^T x[M] \quad (5.36)$$

$$[R] = [S]^{pseudo-inverse} x[M] = pinv[S] x[M] \quad (5.37)$$

In the remainder of the thesis the two methods are used and compared (Chapter 5, 6 and 7). The values of matrix $[M]$ are determined from the relationship between the intensity and the output voltage of the CCD linear sensor (Section 3.2.3). The computation of matrix $[R]$ (based on equations 5.36 and 5.37), is performed using Matlab software version 6.1. The values of matrix $[R]$, which represent the optical attenuation coefficient, are then re-written as a square matrix. These values are represented by a colour in a graph. This graph is interpreted as a tomographic image with pixels of known size, and hence the physical size of the object can be obtained.

The following example shows the 2x2 array of numbers used to investigate the relationship between inverse, transpose, and pseudo-inverse of a matrix. Basic theories on the operation of the transpose and the pseudo-inverse matrices are described in Appendix C.

$$A = \begin{bmatrix} 1 & 2 \\ 3 & 4 \end{bmatrix}, \quad B = \begin{bmatrix} 1 \\ 1 \end{bmatrix}$$

$$A^{-1} = \begin{bmatrix} -2 & 1 \\ 1.5 & -0.5 \end{bmatrix}, \quad A^T = \begin{bmatrix} 1 & 3 \\ 2 & 4 \end{bmatrix}, \quad \text{pinv}(A) = \begin{bmatrix} -2 & 1 \\ 1.5 & -0.5 \end{bmatrix}$$

$$A^{-1}xB = \begin{bmatrix} -1 \\ 1 \end{bmatrix}, \quad A^TxB = \begin{bmatrix} 4 \\ 6 \end{bmatrix}, \quad \text{pinv}(A)xB = \begin{bmatrix} -1 \\ 1 \end{bmatrix}$$

The arguments show that pseudo-inverse in this case is equivalent to inversion of the matrix. In this case of matrix-inversion, the pseudo-inverse correctly represents the inverse matrix. However, the transpose does not give the correct answer. The transpose and pseudo inverse transforms are now used to generate images of several different models. The transpose is widely used in many tomographic researches due to its popularity, fast operation and simplicity (in terms of having the required dimensional form) [Yang *et al*, 1999].

5.2.2.1 3x3 array of pixels (three projections)

Figure 5.7 shows the arrangement of cells for a 3x3 array with three projections.

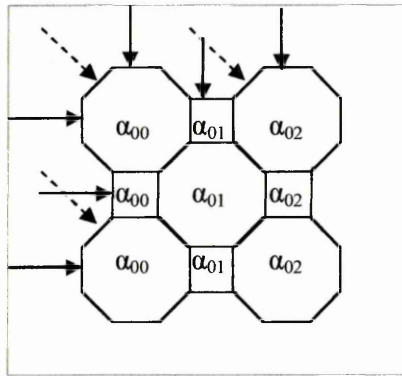
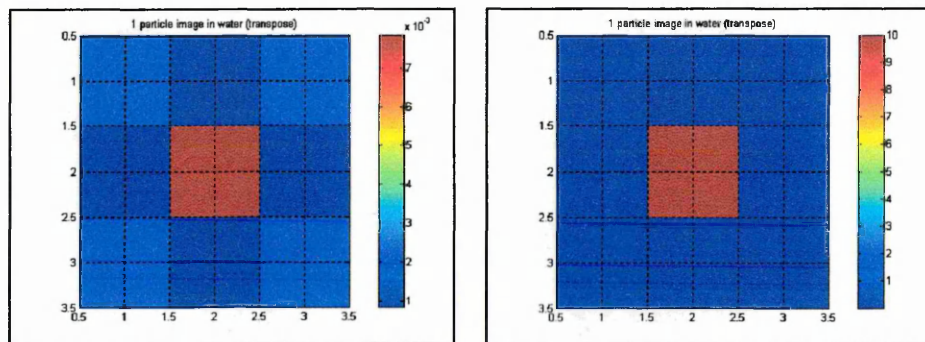


Figure 5.7. A 3x3 array of cells with three projections.

In this case, the matrix S is square because the three projections give the same number of sensors (M_1 to M_9) as the test cells (nine cells of octagonal and square shapes). However, there is no inverse matrix of S because the matrix is too sparse. Figures 5.8a and 5.8b show the reconstructed image of a semi-opaque particle in water (in the middle), using transpose and pseudo-inverse matrices, respectively. The linear attenuation coefficient for the semi-opaque particle is assumed to be 10 mm^{-1} , whilst for water it is 0.00287 mm^{-1} .

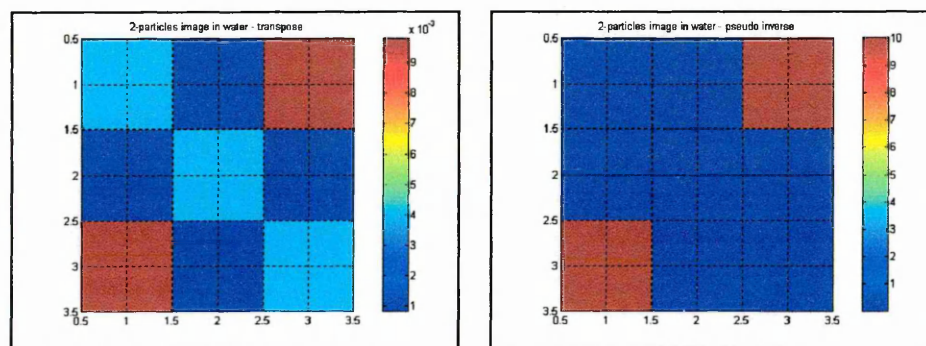


(a) Transpose

(b) Pseudo-inverse

Figure 5.8. One particle in water.

Figures 5.9a and 5.9b show reconstructed images when two similar particles are present in the measurement section.



(a) Transpose

(b) Pseudo-inverse

Figure 5.9. Two-particles in water.

The reconstructed images using the pseudo-inverse matrix are found to be better in representing the actual value of the linear attenuations of water and the particle, compared to the images using the transpose matrix (the linear attenuation values are shown in Appendix C). This is expected, as the pseudo-inverse matrix is closer to the matrix inversion when compared to the transpose matrix. Hence, the contrast is better in the pseudo-inverse image compared to the transpose image. The pseudo inverse image shows no indication of *aliasing* in the top left and bottom right hand corners of the image.

5.2.2.2 7x7 array of pixels

In this section, three different projections are discussed - two, three and four projections. It is seen that the reconstructed image quality improves as the number of projections is increased.

The image with four projections is less smeared, especially when the image is reconstructed using the pseudo-inverse matrix, compared to the one with two projections. Moreover, the effect of *aliasing* on the image is also reduced as the number of projections is increased. This is more noticeable when the image in Figure 5.10 (with two projections) is compared with the four-projection image in Figure 5.12.

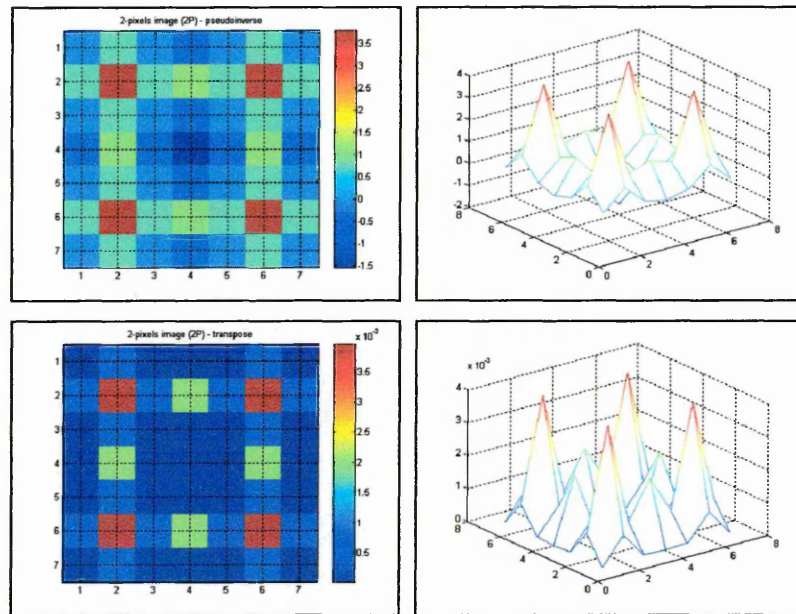


Figure 5.10. Two-particles image with two projections: pseudo-inverse (top) and transpose (bottom).

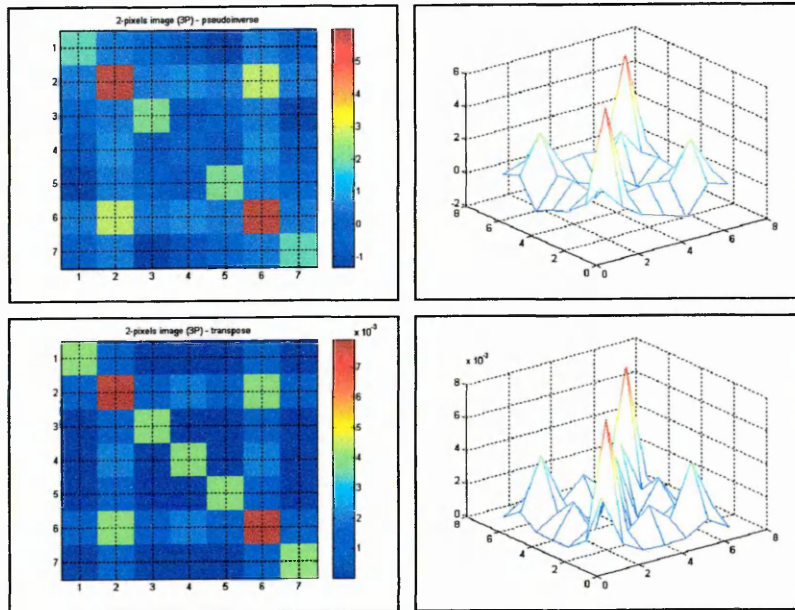


Figure 5.11. Two-particles image with three projections.

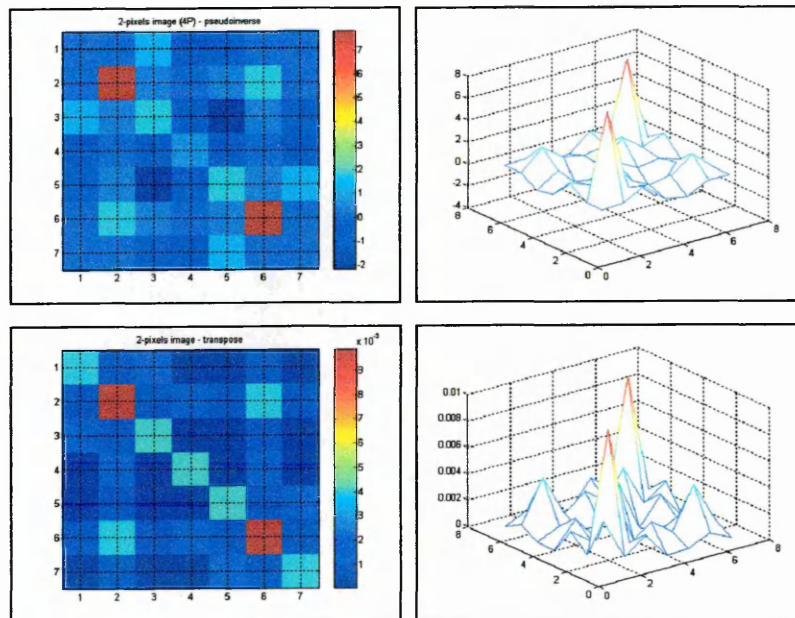


Figure 5.12. Two-particles image with four projections.

5.2.2.3 21x21 array of pixels

In the actual system, the effective cells to represent an object vary between approximately 7 cells (for a 100 micron particle) up to 71 cells (for a 1 mm particle). Since the optical tomography system is intended for small diameter particles, only a few of the whole 2048 pixels are used. Hence, the reconstruction may be simplified by only imaging a small area of the measurement section.

A 21x21 array of pixels actually represents $0.294 \times 0.294 \text{ mm}^2$ image area with an image pixel size of 0.014 mm by 0.014 mm. A 100 micron object with a round shape in water is modelled using the forward problem. The object is positioned in the middle of the measurement section, where the attenuation coefficients of water fill image pixels beyond this $0.294 \times 0.294 \text{ mm}^2$ image area. Figures 5.13 and 5.14 show images representing one 100 micron particle in water obtained using the pseudo inverse and the transpose matrices, respectively.

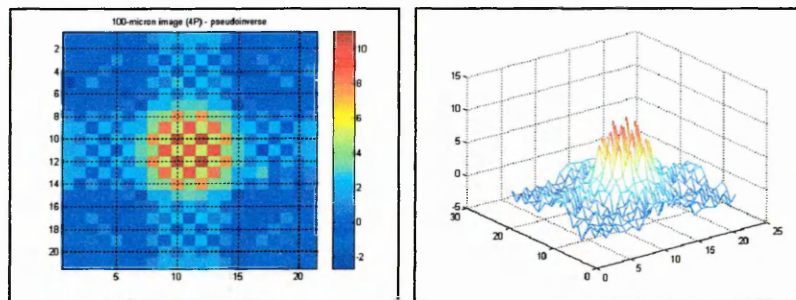


Figure 5.13. A 100 micron reconstructed image using pseudo inverse.

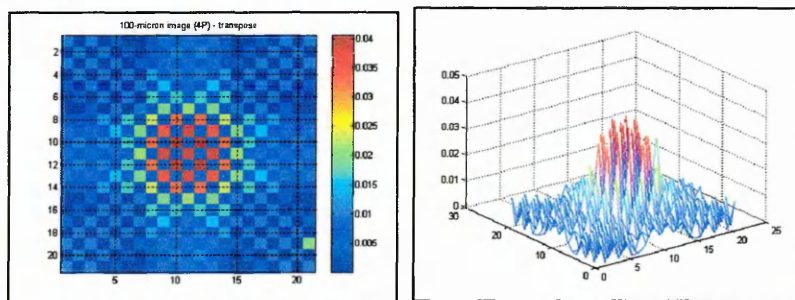


Figure 5.14. A 100 micron reconstructed image using transpose.

5.2.2.4 101x101 array of pixels

In the actual system, the effective number of sensors per projection used to generate the image ranges from approximately 7 pixels (for a 100 micron particle) up to 71 pixels (for a 1 mm particle). Since the optical tomography system is intended for measuring small diameter particles, only about 5% (101 pixel/2048 pixel \times 100) of the whole 2048 pixels per projection are used. Hence, a smaller array of pixels is used so that the reconstruction process is less complex (due to the smaller size of the matrices involved) and faster. In the actual system a 101x101 array of pixels is used for the reconstruction of the tomographic images i.e. 1.414x1.414 mm² area of image.

The full reconstruction operation requires a 2048x2048 array of pixels, which requires a lot of memory space (approximately 275 Gigabytes!). The actual size of the matrix (four projections) = $[4n \text{ by } n^2]$ where n is the number of sensors in each CCD linear image sensor. Therefore, the required memory size is the multiplication of the actual matrix size with 8 bytes i.e. $32n^3$. This result is only based on the amount of memory needed for the sensitivity matrix (S matrix) with four projections. The actual calculation would need more memory and hence the whole operation is just not possible on a PC. Table 5.1 shows the minimum memory required to perform the reconstruction process as the numbers of pixels is increased whilst Figure 5.15 shows the graph of the relationship.

Table 5.1. Relationship between number of sensors per projection (n) and memory size.

n	Memory (byte)
3	864
5	4,000
7	10,976
21	296,352
41	2,205,472
61	7,263,392
81	17,006,112
101	32,969,632
201	259,859,232
301	872,668,832
401	2,063,298,432
501	4,024,048,032
601	6,946,617,632
801	16,445,516,832
1001	32,096,096,032
1201	55,434,355,232
1401	87,996,294,432
1601	131,317,913,632
1801	186,935,212,832
2001	256,384,192,032
2049	275,280,756,768

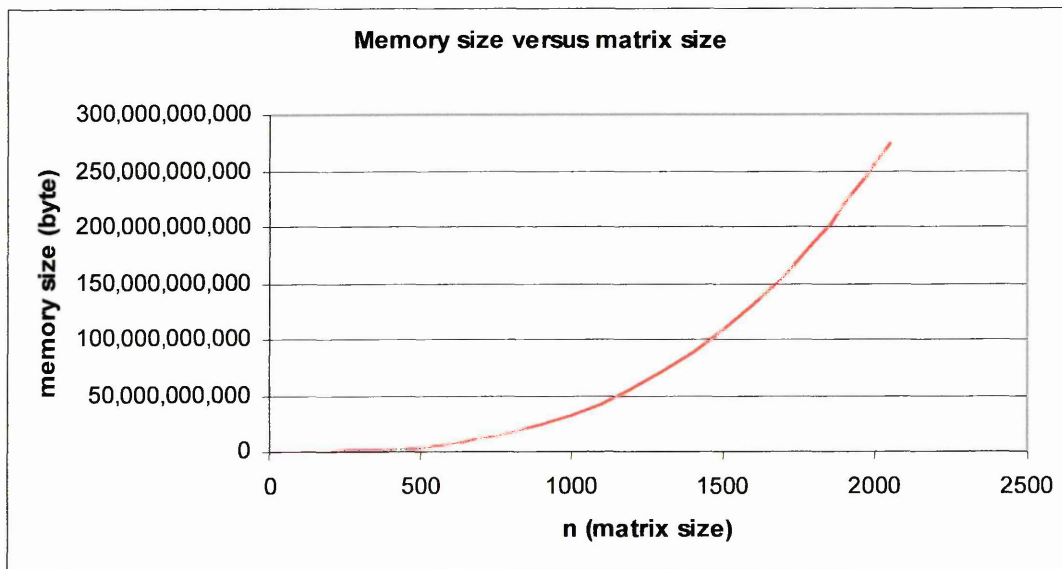


Figure 5.15. A graph of n versus memory size.

The limitation of the computer memory limits the reconstructed image area to a 101x101 array of pixels (1.414x1.414 mm²). In order to reconstruct a larger object, a scaling process is done where several pixels are grouped together before averaging them. For example, averaging five CCD pixels to give a single measurement value which represents a spatial length of 0.07-mm. If the 101x101 array of pixels is used combined with this averaging, the image area is increased to 7.07x7.07mm².

A 101x101 array of pixels (with different scaling factor) is used to generate the reconstructed images in the remainder of this thesis (Chapters 6 and 7).

5.3 Discussion

A novel arrangement of cells with a combination of square-shaped cells and octagon-shaped cells makes the image reconstruction process possible for the ccd-based optical tomography system. In this case, the square-shaped cell has two projections whereas the octagon-shaped cell has four projections of measurements. The tomographic images reconstructed using the transpose matrix is found to be producing qualitative images whilst the image reconstructed using the pseudo inverse matrix contains the quantitative information of the image. The main reason is that the pseudo inverse matrix represents the closest generalisation of matrix inversion. Moreover, the pseudo inverse minimises the error between the calculated values and the real values. On the other hand, the transpose calculates a value, which is often used as a basis for iterative image improvement. The transpose is much quicker to calculate than the pseudo inverse. Comparative times for a 101x101 pixel image are: 20 seconds (transpose) and 1 hour (pseudo inverse).

CHAPTER 6

EXPERIMENTAL RESULTS

6.1 The calibration process

The CCD-based optical instrumentation system was calibrated and tested for accuracy, repeatability of measurements and repeatability of projections readings. Test pieces with known diameters were used. These consisted of steel rods with nominal diameters of 400 micron, 2 mm, 3.7 mm and 10.5 mm. The actual diameters of the test pieces were 395 micron, 2 mm, 3.66 mm and 10.47 mm. The tomographic measurements were acquired by the Keithley DAS data acquisition system with an operating frequency of 250 kHz.

The projections were identified in the following tables – Projection 1 is P1, Projection 2 is P2, Projection 3 is P3 and Projection 4 is P4. The measurements are obtained in the form of pixels which are in shadow (Section 3.2.1). These measurements are converted to millimetres using one pixel as being equivalent to 0.014 mm. The measurements were repeated ten times for each of the four projections (projections 1, 2, 3 and 4) in order to obtain the mean and standard deviations of the measurement.

The experiments were performed in a dark room to avoid any light from the surroundings interfering with the system (Section 4.2). The tomographically reconstructed images of the measurements were performed using Matlab version 6.1 on a Pentium III computer. The images are reconstructed using both the transpose and pseudo inverse sensitivity matrices.

6.1.1 Accuracy

The tomographic instrumentation system based on the CCD linear image sensor has been calibrated and tested for its accuracy, repeatability and consistency. These factors are important in order to test the performance of the system. Accuracy is a test carried out to observe the closeness of the measured value to the true value.

Table 6.1 and Figure 6.1 show the summarised accuracy of the system when four test pieces with known diameters (nominally 0.4 mm, 2 mm, 3.7 mm and 10.5 mm) were used in the experiment. The test pieces were positioned at the centre of the measurement section. Ten diameter measurements for each projection were taken and averaged for the final measured diameter of the particle (Appendix D). The diameter measurement is based on the diffraction theory discussed in Section 3.4, where the measured value was taken at a threshold level of 25% of the signal's amplitude (Section 3.4.2)

The diffraction patterns of the measured particles were compared with the calculated Fresnel diffraction patterns (Section 3.4.2), and shown in Figure 6.2. The experiments performed on the optical tomography system were based on the CCD linear image sensors operated slightly above saturation level. Hence, diffraction information is lost from the full illumination at each side of the shadow.

The designed system has accuracy better than 0.0085 mm (0.6 pixel), with the percentage error better than 1.456% (Table 6.1). The accuracy is acceptable because the error is less than 1 pixel i.e. 0.014 mm.

Table 6.1. Accuracy calculations of the four-projections measurements.

	0.395-mm	2.00-mm	3.66-mm	10.47-mm
AVG P1 (mm)	0.402	1.967	3.654	10.469
AVG P2 (mm)	0.385	1.998	3.662	10.476
AVG P3 (mm)	0.413	1.995	3.667	10.487
AVG P4 (mm)	0.403	2.006	3.679	10.445
AVG (mm): 4P	0.401	1.992	3.666	10.469
STD DEV	0.01	0.02	0.01	0.02
ABS ERROR (mm)	0.0057	0.0085	0.0055	0.0008
ABS ERROR (pix)	0.4	0.6	0.4	0.1
% ERROR	1.456	0.425	0.150	0.007

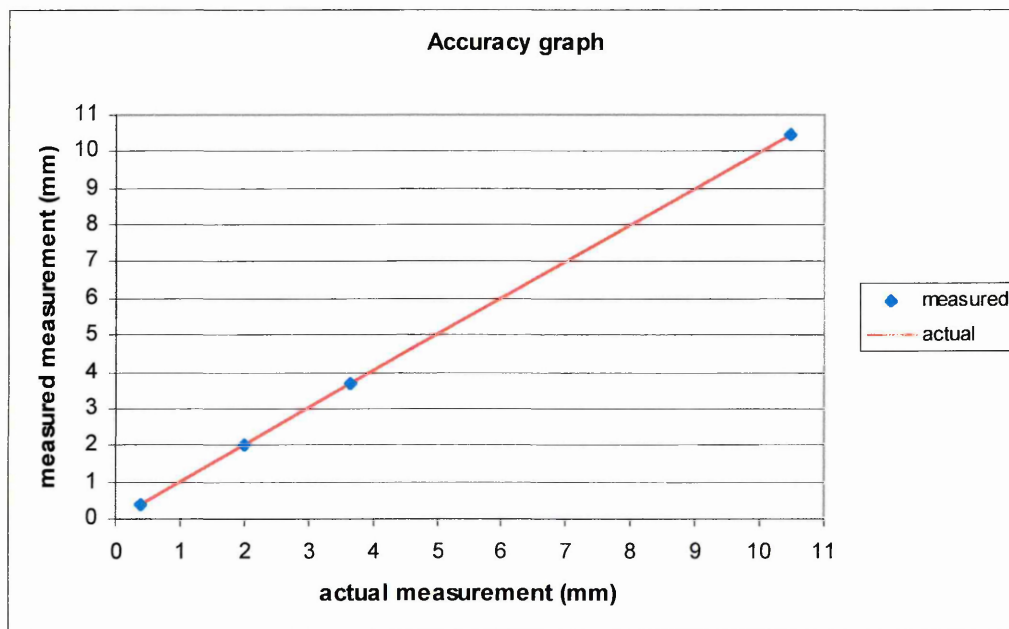
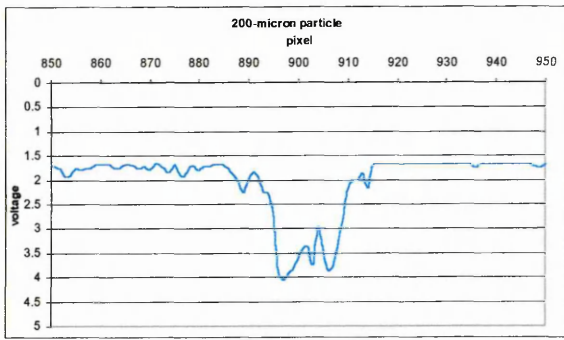
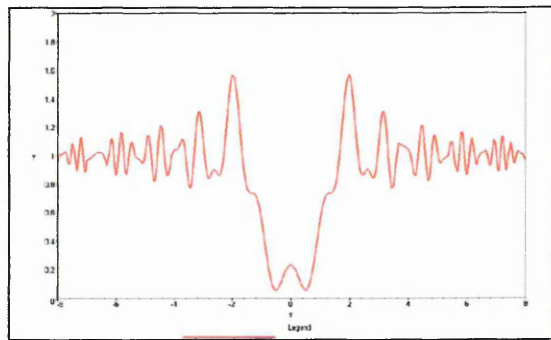


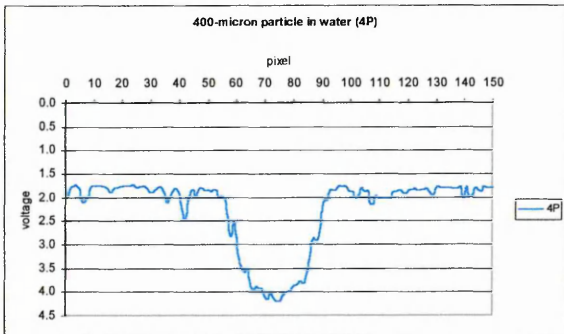
Figure 6.1. An accuracy graph.



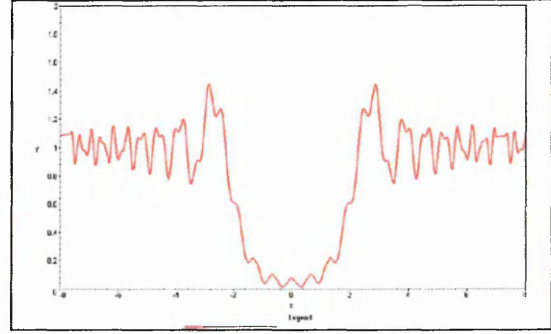
(a) 0.2 mm particle (measured)



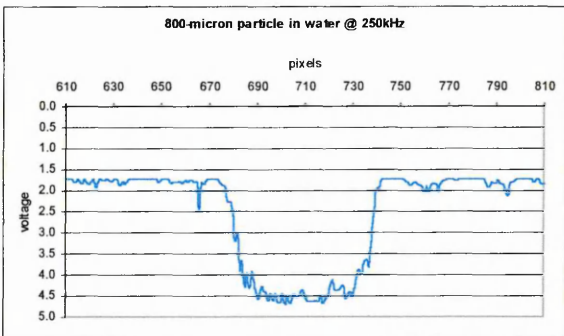
(b) 0.2 mm particle (model)



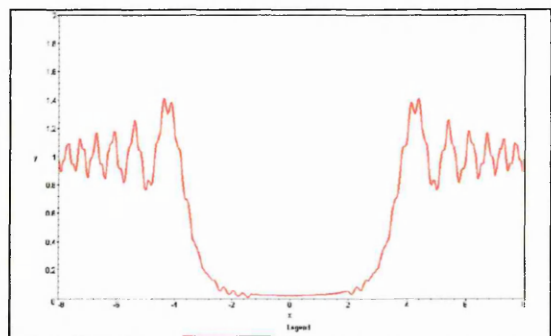
(c) 0.4 mm particle (measured)



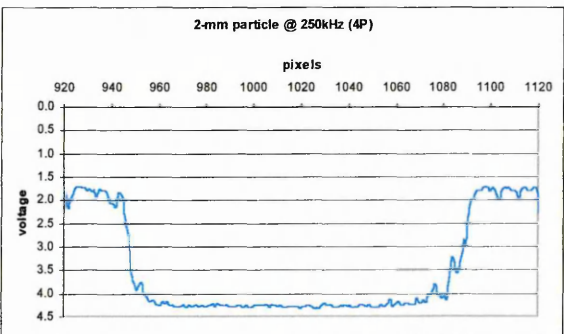
(d) 0.4 mm particle (model)



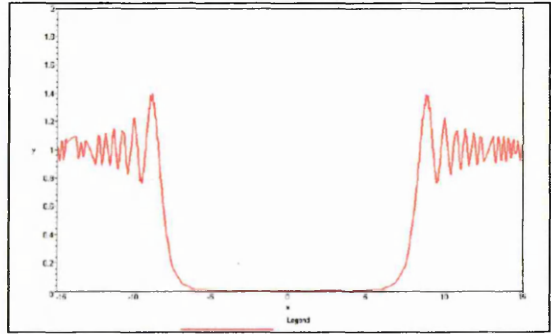
(e) 0.8 mm particle (measured)



(f) 0.8 mm particle (model)



(g) 2 mm particle (measured)



(h) 2 mm particle (model)

Figure 6.2. Diffraction patterns for measured and model data.

6.1.2 Repeatability

Repeatability is a test of reproducibility i.e. closeness of repeated readings in the measurements after several readings are taken. Ten measurements were taken for each projection (Appendix C). The repeatability of the test pieces (0.4 mm, 2 mm, 3.7 mm and 10.5 mm diameters) is summarised in Table 6.1. Figures 6.3 to 6.6 show the graphical representation of repeatability in the measurements.

The repeatability of the measurements is:

0.40 mm \pm 0.01 mm standard deviation

1.99 mm \pm 0.02 mm standard deviation

3.67 mm \pm 0.01 mm standard deviation

10.47 mm \pm 0.02 mm standard deviation

The measurements deviated less than 1.25 pixels from the actual values, which is good considering the size of the pixel is only 14 micron.

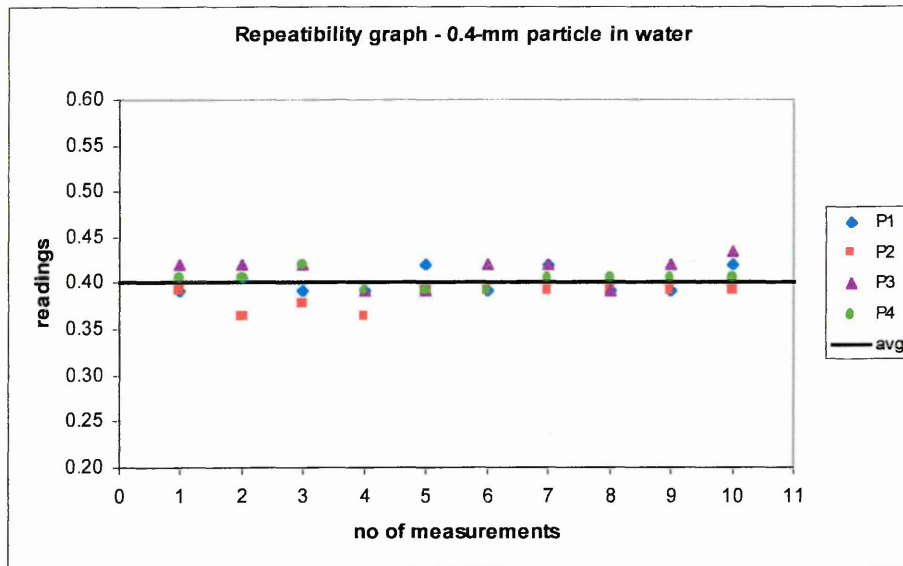


Figure 6.3. Repeatability graph for a 0.4 mm particle in water.

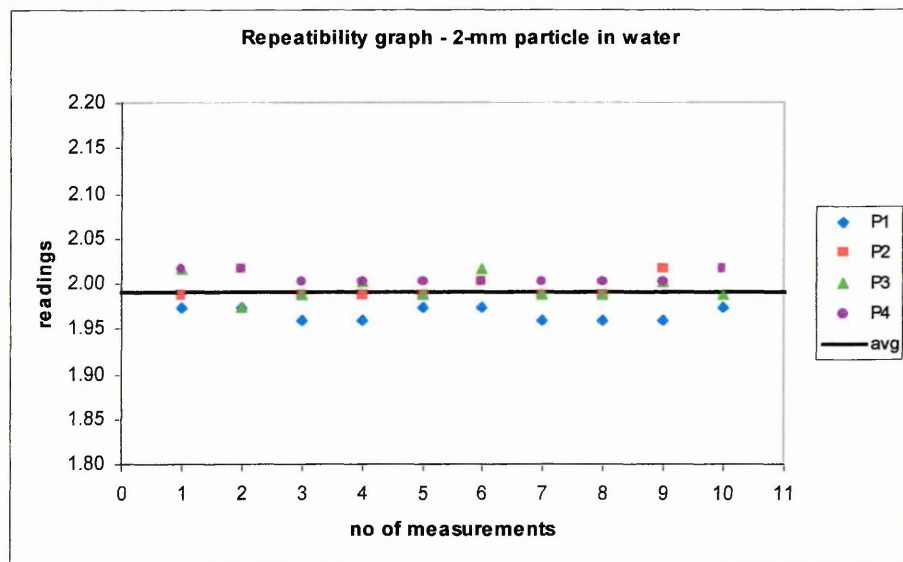


Figure 6.4. Repeatability graph for a 2 mm particle in water.

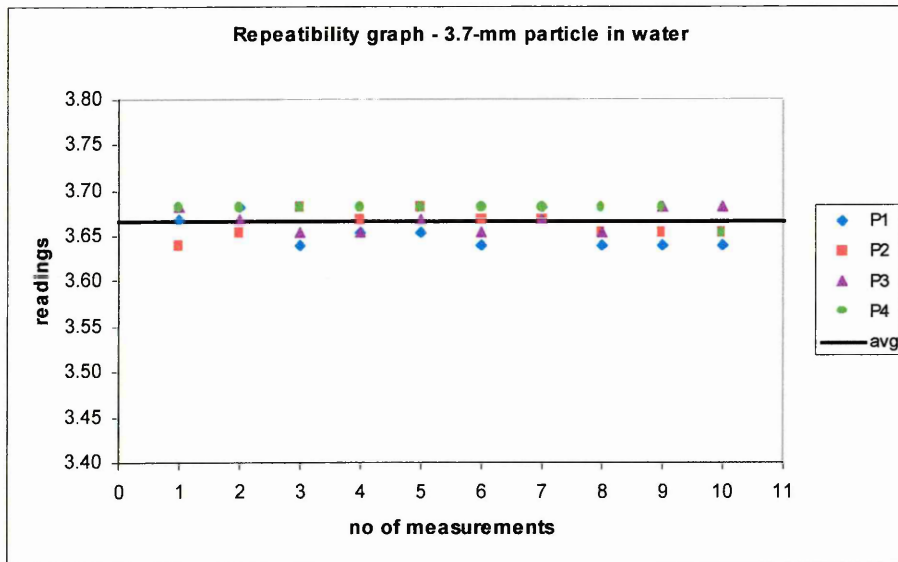


Figure 6.5. Repeatability graph for a 3.7 mm particle in water.

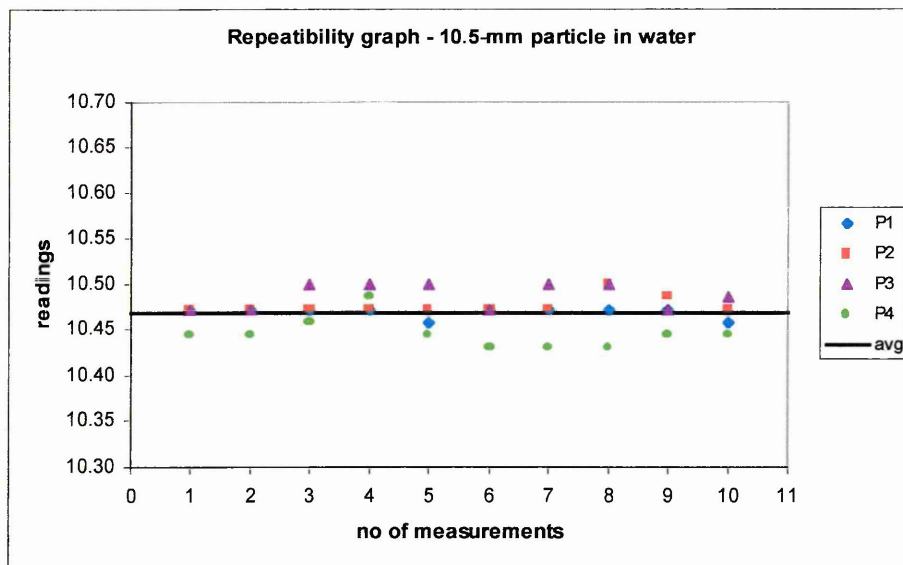


Figure 6.6. Repeatability graph for a 10.5 mm particle in water.

6.1.3 Repeatability in projections readings (consistency)

It is important to quantify how far the measurements between all four projections (projection 1, 2, 3 and 4) are consistent with each other, as the projections should have identical responses. The consistency among the projections shows how far the measurements for each projection deviate from each other i.e. comparability of the projection readings (Table 6.2).

Table 6.2. Consistency in the projections.

	400 micron	2-mm	3.66-mm	10.47-mm
STD DEV P1 (mm)	0.013	0.007	0.017	0.006
STD DEV P2 (mm)	0.012	0.013	0.014	0.009
STD DEV P3 (mm)	0.015	0.014	0.012	0.014
STD DEV P4 (mm)	0.009	0.007	0.009	0.017
AVG (STD DEV P1-P4)	0.012	0.010	0.013	0.012
STD (STD DEV P1-P4)	0.0025	0.0038	0.0034	0.0049

From Table 6.6, the system has standard deviations less than 0.014 mm i.e. less than 1 pixel. The projection readings are consistent, which are expected, as the projection system is identical.

6.1.4 The tomographic images of the test pieces

Figure 6.7 shows the reconstructed images from the four projections using transpose and pseudo inverse sensitivity matrices. The maximum pixels per axis that can be processed for the image reconstruction is 101 pixels i.e. 1.414 mm. However, several adjacent sensor pixel measurements can be grouped together and an average calculated. These groups of pixels can be used to scale larger objects (Section 5). By clumping four adjacent pixels, the effective pixel size is increased from 0.014 mm up to 0.056 mm. The 101 pixels in the reconstruction then represent 5.656 mm. Figure 6.8 shows the results of combining four adjacent pixels and averaging for the 0.4 mm particle in water.

These results are discussed in Sections 6.4.

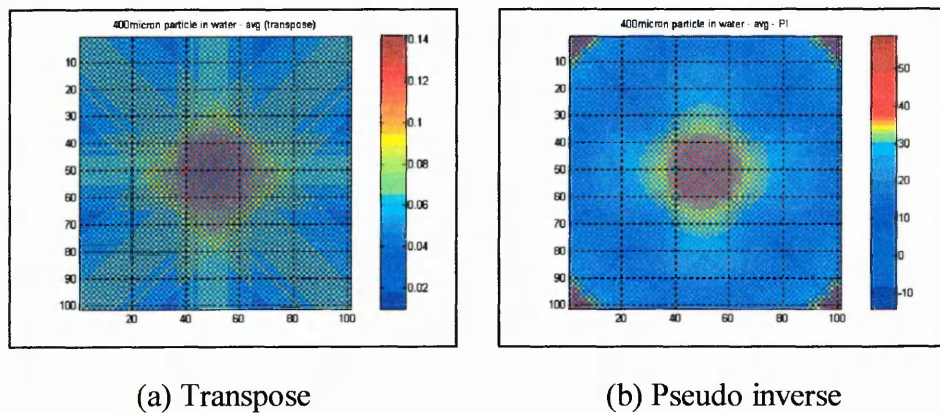


Figure 6.7. 400 micron particle in water.

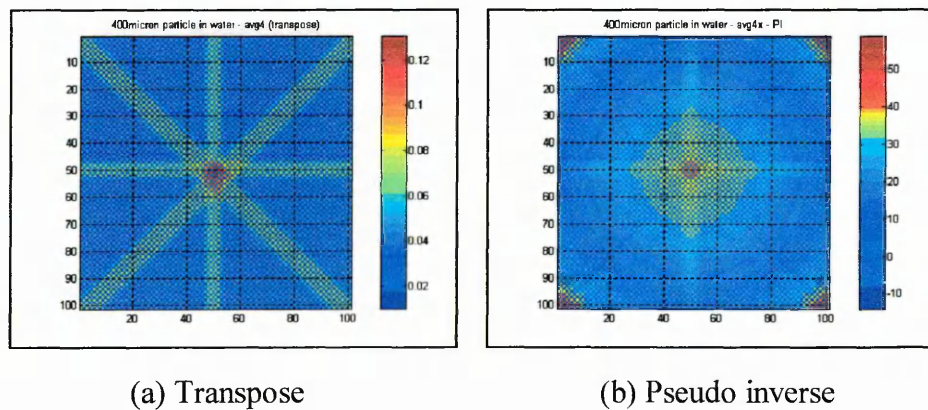


Figure 6.8. 400 micron particle in water (averaging 4-pixels).

6.2 Measurements of a 3 mm sphere bead

The calibrated tomographic instrumentation system was used to measure a 3 mm diameter bead. The bead is made of plastic and black in colour. A micrometer system was designed to measure different positions of the bead as it was lowered down into the measurement cross-section. Figure 6.9 shows the schematic diagram of the micrometer level system, whilst Figure 6.10 shows a photograph of the system. The bead was lowered in steps of approximately 0.2 mm through the measurement section and the outputs from the four projections were monitored (Figure 6.11).

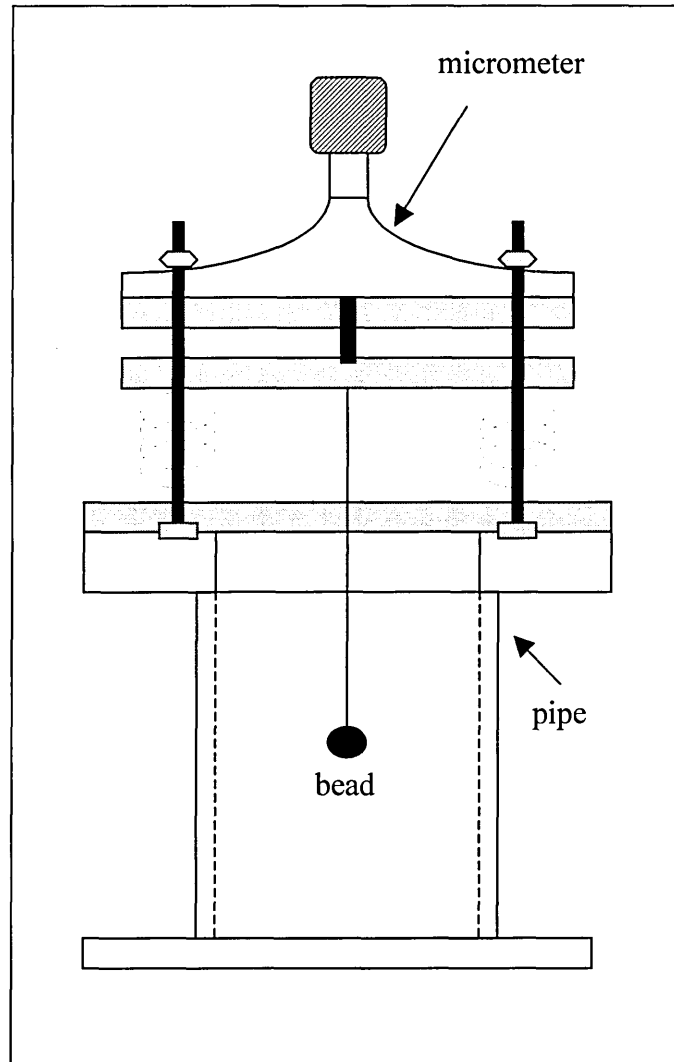


Figure 6.9. A micrometer level system.

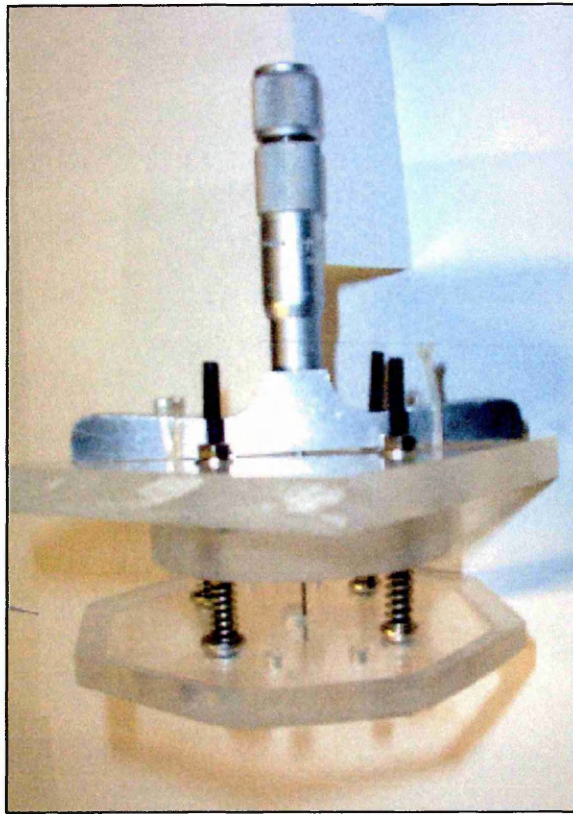


Figure 6.10. A photograph of the micrometer level system.

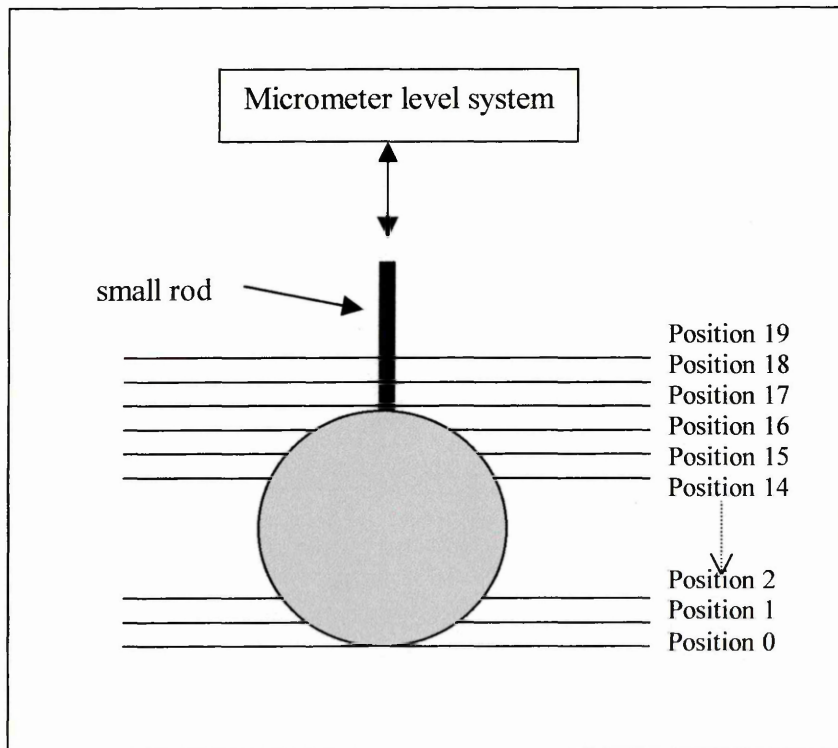


Figure 6.11. Different positions in monitoring bead's diameter.

The bead has the shape of a sphere. Hence all four projections view the same diameter due to the symmetry of the sphere. Therefore, the average diameters of all four projections are used in the diameter distribution graph (Table 6.3). Figure 6.12 and Figure 6.13 show the diameter distribution in pixels and millimetres, respectively.

These results are discussed in Section 6.4.

Table 6.3. Measurements of each transition in the 3 mm bead movement.

4 PROJECTIONS (AVERAGE)				
Position	pixel	pixel	mm	mm
19	28.88	-28.88	0.40	-0.40
18	29.38	-29.38	0.41	-0.41
17	29.75	-29.75	0.42	-0.42
16	33.38	-33.38	0.47	-0.47
15	42.50	-42.50	0.60	-0.60
14	72.25	-72.25	1.01	-1.01
13	86.38	-86.38	1.21	-1.21
12	98.50	-98.50	1.38	-1.38
11	103.00	-103.00	1.44	-1.44
10	105.75	-105.75	1.48	-1.48
9	104.50	-104.50	1.46	-1.46
8	104.13	-104.13	1.46	-1.46
7	102.88	-102.88	1.44	-1.44
6	98.88	-98.88	1.38	-1.38
5	91.75	-91.75	1.28	-1.28
4	82.00	-82.00	1.15	-1.15
3	70.13	-70.13	0.98	-0.98
2	36.25	-36.25	0.51	-0.51
1	0	0	0	0

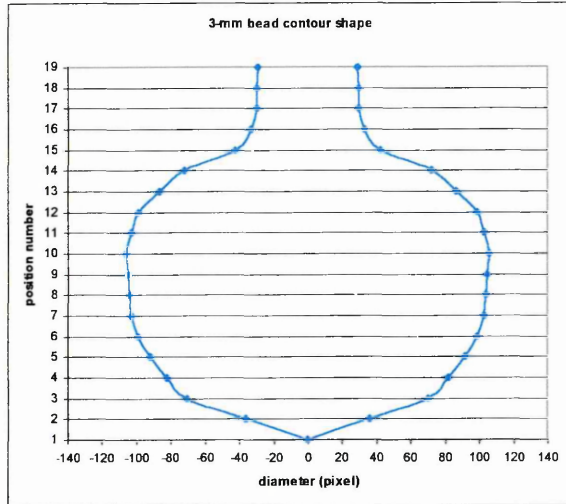


Figure 6.12. The diameter distribution of the bead in pixels.

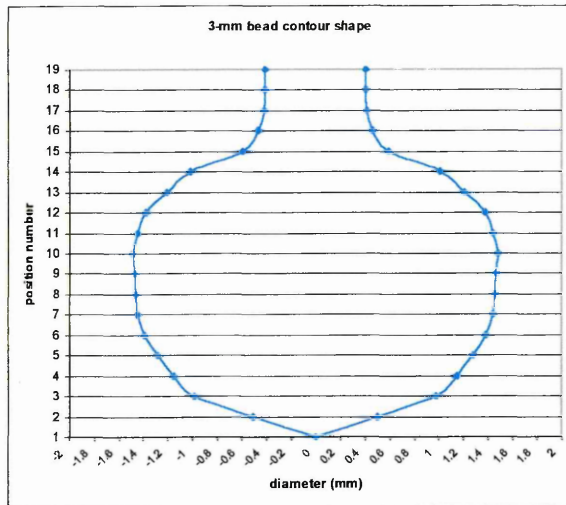


Figure 6.13. The diameter distribution of the bead in millimetres.

6.2.1 The tomographic images of the bead

The tomographic image reconstruction of the bead was performed using the four projections measurements of each position of the bead. Figure 6.14 to Figure 6.15 are the reconstructed images of the bead by means of transpose sensitivity matrix. Figure 6.16 to Figure 6.17 show the reconstructed images of the bead using pseudo inverse sensitivity matrix.

The time taken for the image reconstruction process using the transpose is approximately 40 seconds per operation, whilst the reconstruction process using pseudo inverse took approximately one hour per operation.

These results are discussed in Section 6.4.

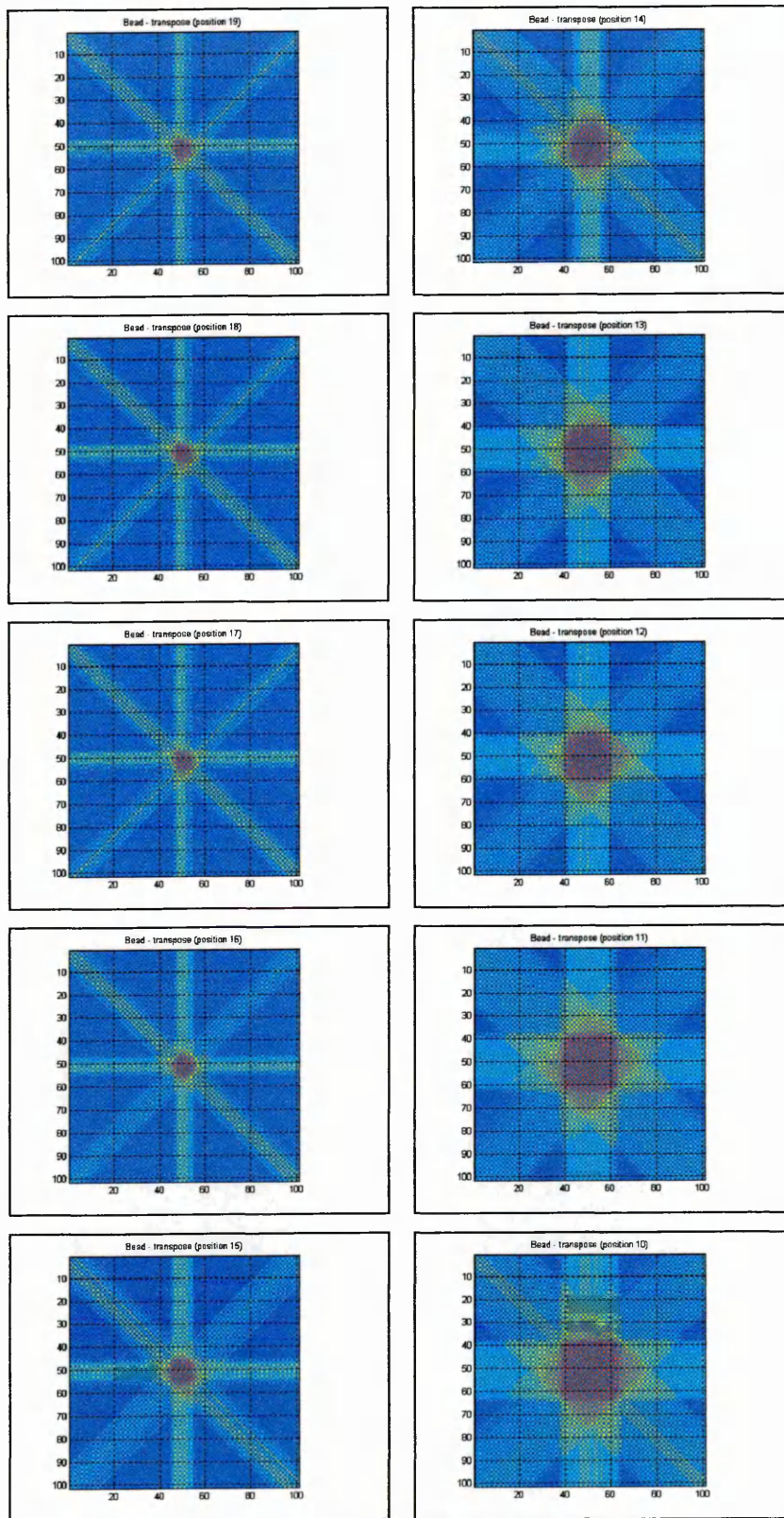


Figure 6.14. Images of the bead (transpose) – position 19 – 10.

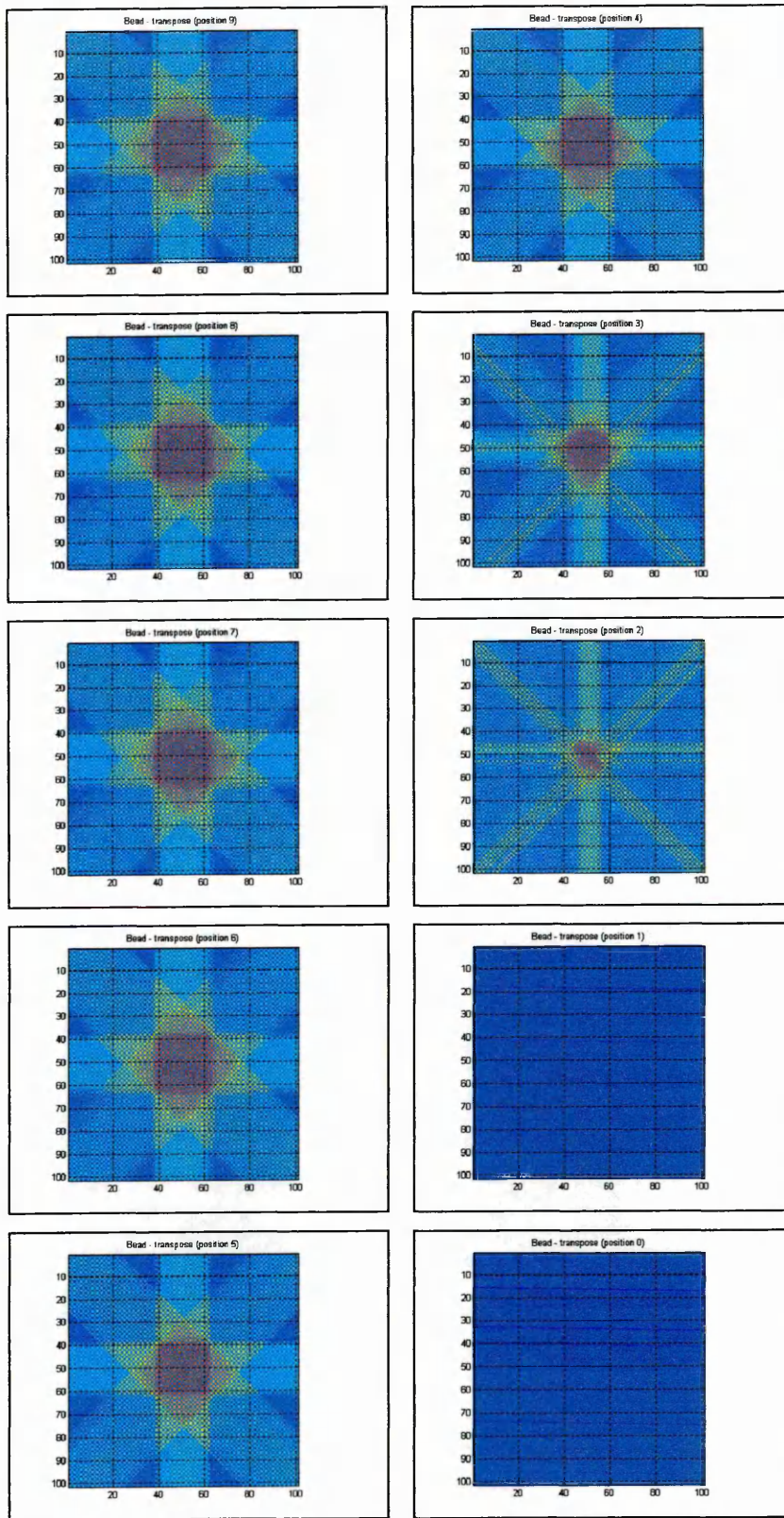


Figure 6.15. Images of the bead (transpose) – position 9 – 0.

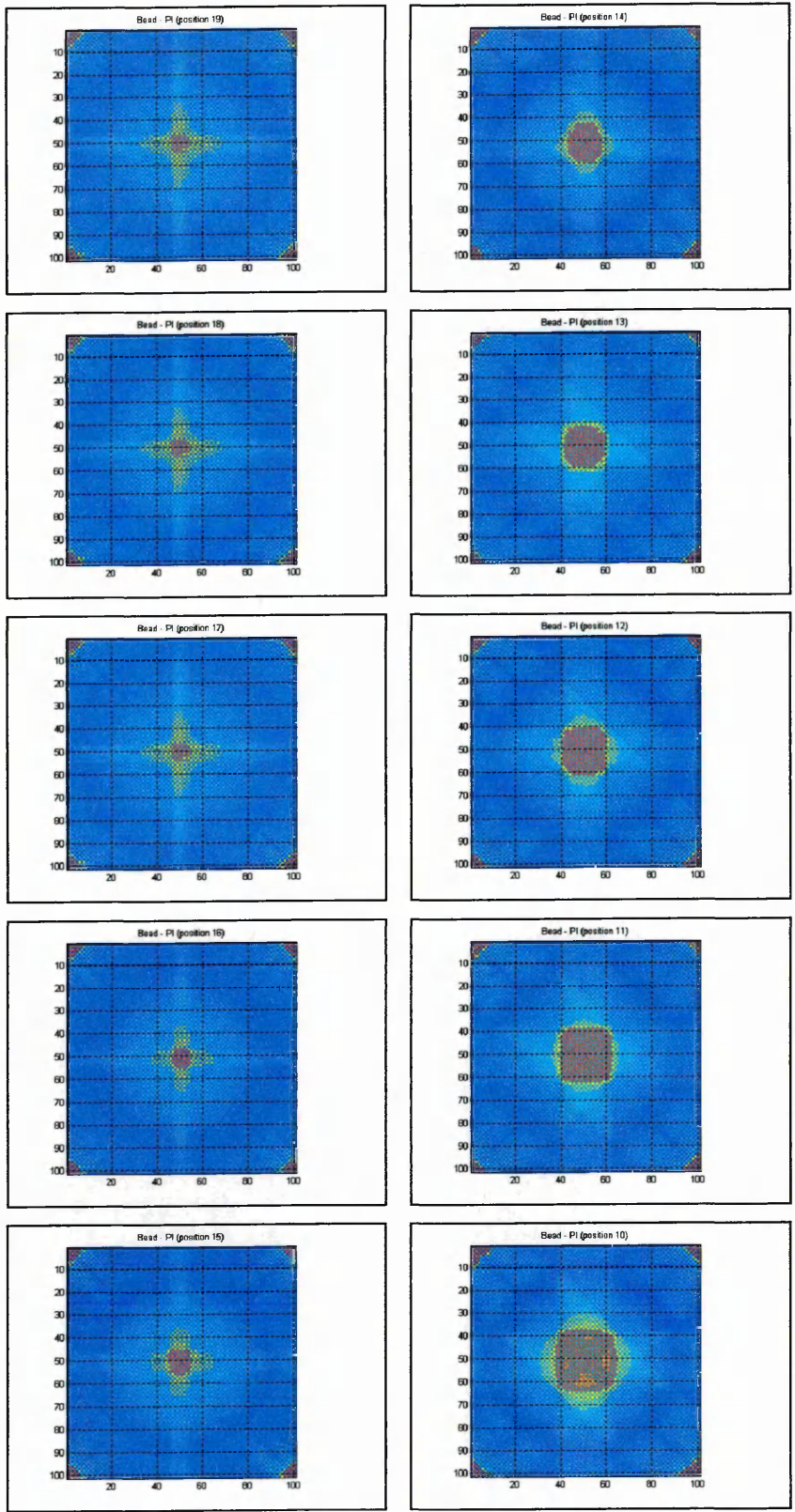


Figure 6.16. Images of the bead (pseudoinverse) – position 19 – 10.

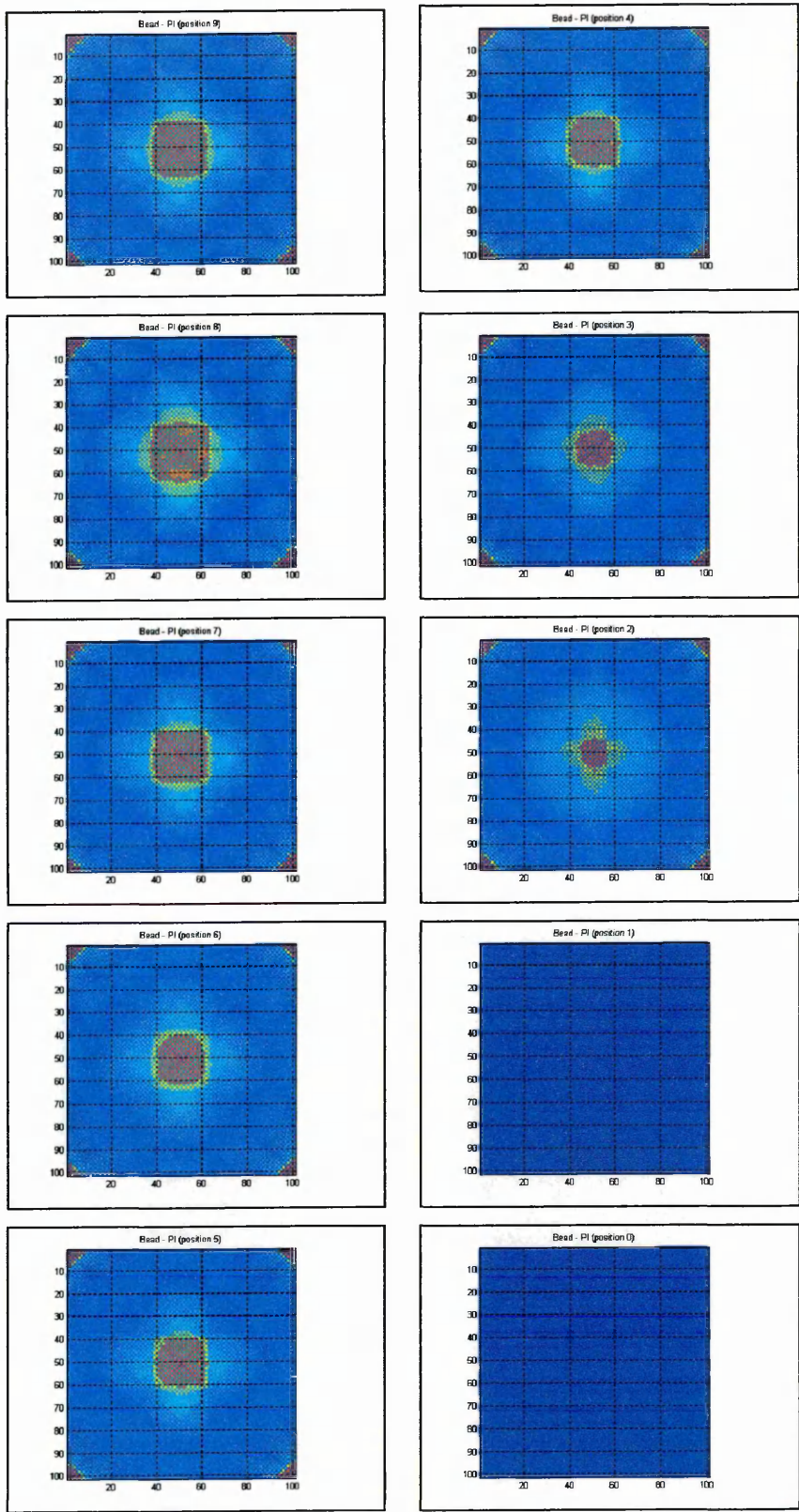


Figure 6.17. Images of the bead (pseudoinverse) – position 9 – 0.

6.2.2 Filtered tomographic images of the bead

Both the transpose and pseudo inverse have ‘smeared’ images, which make visualisation of the target difficult. To improve the image quality, filtering, in the form of thresholding is applied.

The images are filtered by thresholding at an attenuation coefficient value of 25 mm^{-1} . The values of the pixels in the tomographically reconstructed images represent optical linear attenuation coefficients. The linear attenuation coefficient of air is 0.00142 mm^{-1} whilst the linear attenuation coefficient of opaque solid particles is infinity (in this case a large value). The threshold value of 25 mm^{-1} is chosen to minimise the effect of smearing in the filtered image compared to other values, and still retain information about the particle.

All the individual tomographic slices are shown as a contoured slice plane. The contoured slice plane of the bead using pseudo inverse sensitivity matrix at all twenty position is shown in Figures 6.18. Further discussions on these results are discussed in Section 6.4.

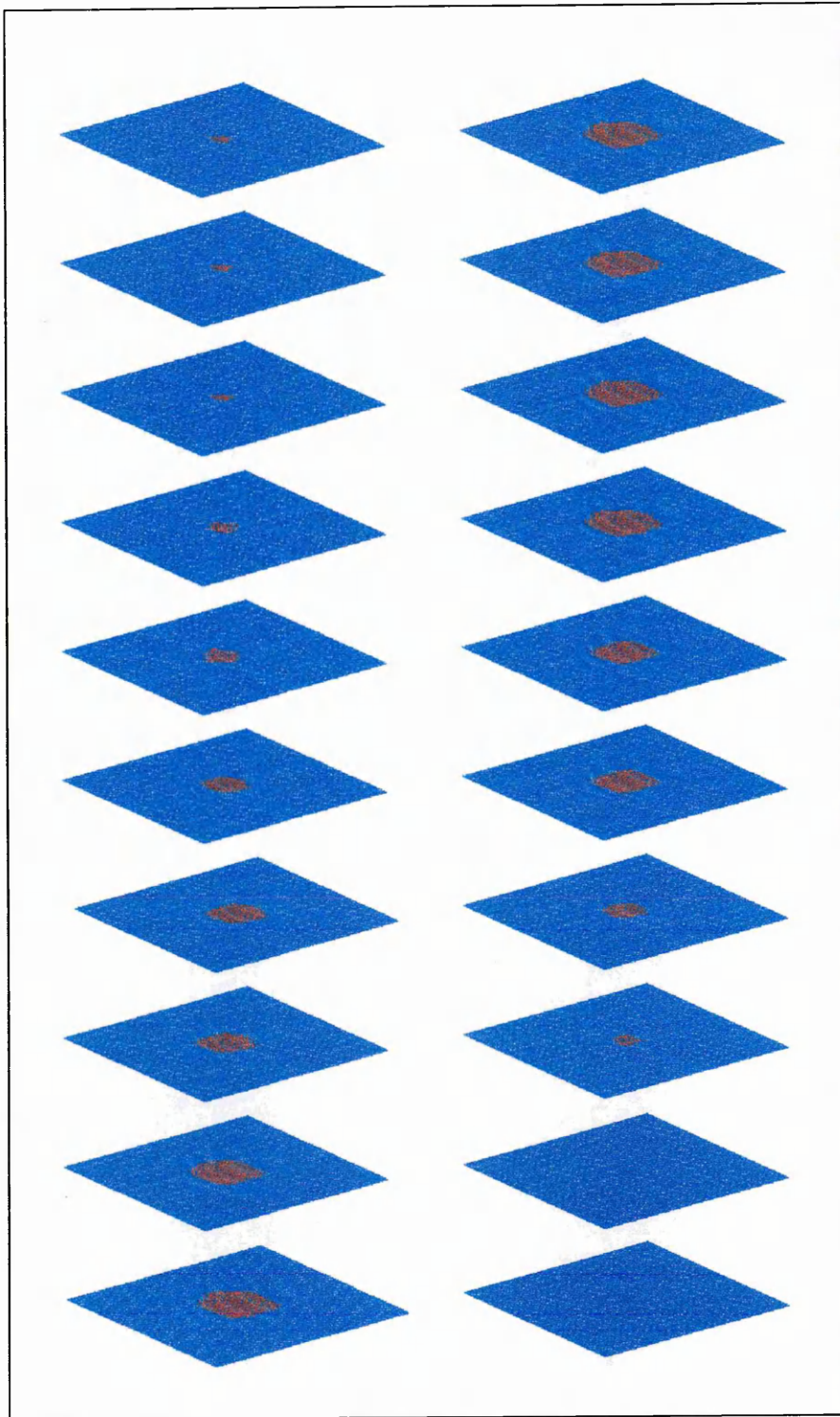


Figure 6.18. Contoured slice planes of the bead for all positions (pseudo inverse).

6.3 The measurements of an irregular shaped nut

The tomographic instrumentation system was used to measure diameters of an irregular shaped nut. Twenty steps (approximately 0.20 mm per step) of measurements were taken as the nut was lowered down into the pipe using the micrometer level system (Section 6.2), which is shown in Figure 6.19. Due to the irregularities in the nut's shape, all four projections result in different images of the nut i.e. the shape is not symmetrical. Hence, the distribution of the diameter is different for each of the four projections. Table 6.4 to Table 6.7 tabulate the measurements obtained from each of the four projections. Figures 6.20 to Figure 6.23 show the diameter distribution of the nut for projection 1, 2, 3, and 4 respectively. The measurements are then used in the image reconstruction process using the transpose and pseudo inverse sensitivity matrix.

These results are discussed in Section 6.4.

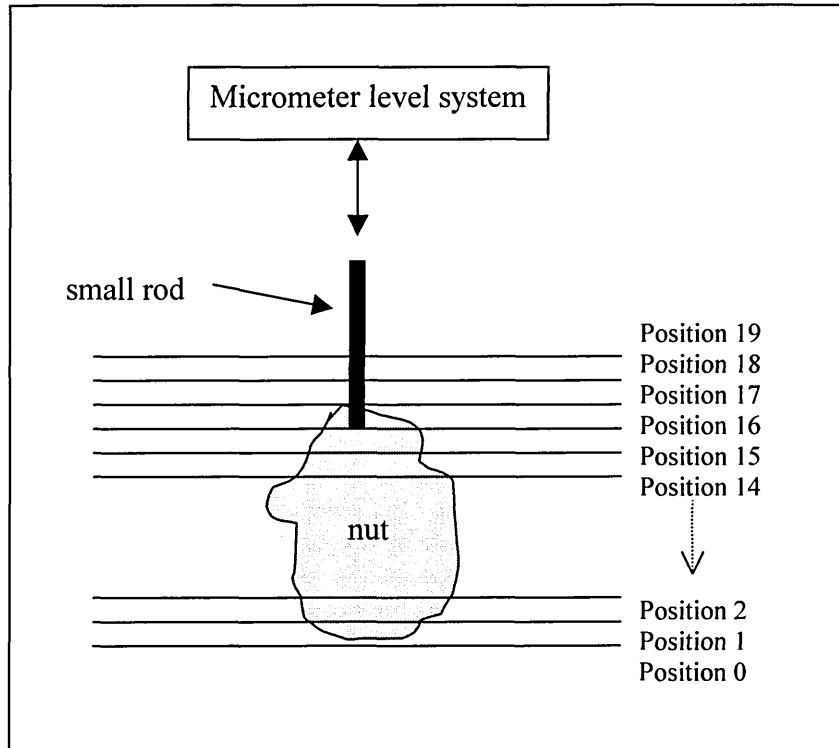


Figure 6.19. Twenty positions in monitoring nut diameter.

Table 6.4. Measurements of transitions in the irregular-shaped nut movement (P1).

PROJECTION 1				
Position	pixel	pixel	mm	mm
19	29.5	-29.5	0.413	-0.413
18	31	-31	0.434	-0.434
17	30.5	-30.5	0.427	-0.427
16	31	-31	0.434	-0.434
15	30.5	-30.5	0.427	-0.427
14	43.5	-43.5	0.609	-0.609
13	55.5	-55.5	0.777	-0.777
12	60	-60	0.84	-0.84
11	67	-67	0.938	-0.938
10	76	-76	1.064	-1.064
9	88.5	-88.5	1.239	-1.239
8	93.5	-93.5	1.309	-1.309
7	99.5	-99.5	1.393	-1.393
6	94.5	-94.5	1.323	-1.323
5	94.5	-94.5	1.323	-1.323
4	91.5	-91.5	1.281	-1.281
3	87	-87	1.218	-1.218
2	79	-79	1.106	-1.106
1	65.5	-65.5	0.917	-0.917
0	0	0	0	0

Table 6.5. Measurements of transitions in the irregular-shaped nut movement (P2).

PROJECTION 2				
Position	pixel	pixel	mm	mm
19	29.5	-29.5	0.413	-0.413
18	31	-31	0.434	-0.434
17	30.5	-30.5	0.427	-0.427
16	29.5	-29.5	0.413	-0.413
15	35	-35	0.49	-0.49
14	36.5	-36.5	0.511	-0.511
13	45.5	-45.5	0.637	-0.637
12	70.5	-70.5	0.987	-0.987
11	76.5	-76.5	1.071	-1.071
10	80.5	-80.5	1.127	-1.127
9	83	-83	1.162	-1.162
8	92	-92	1.288	-1.288
7	97	-97	1.358	-1.358
6	96.5	-96.5	1.351	-1.351
5	86	-86	1.204	-1.204
4	85.5	-85.5	1.197	-1.197
3	79	-79	1.106	-1.106
2	78	-78	1.092	-1.092
1	36.5	-36.5	0.511	-0.511
0	0	0	0	0

Table 6.6. Measurements of transitions in the irregular-shaped nut movement (P3).

PROJECTION 3				
Position	pixel	pixel	mm	mm
19	29.5	-29.5	0.413	-0.413
18	31	-31	0.434	-0.434
17	30.5	-30.5	0.427	-0.427
16	37	-37	0.518	-0.518
15	67	-67	0.938	-0.938
14	68.5	-68.5	0.959	-0.959
13	71.5	-71.5	1.001	-1.001
12	74	-74	1.036	-1.036
11	70	-70	0.98	-0.98
10	69.5	-69.5	0.973	-0.973
9	70	-70	0.98	-0.98
8	71	-71	0.994	-0.994
7	67	-67	0.938	-0.938
6	60.5	-60.5	0.847	-0.847
5	52.5	-52.5	0.735	-0.735
4	50	-50	0.7	-0.7
3	43	-43	0.602	-0.602
2	32	-32	0.448	-0.448
1	68	-68	0.952	-0.952
0	0	0	0	0

Table 6.7. Measurements of transitions in the irregular-shaped nut movement (P4).

PROJECTION 4				
Position	pixel	pixel	mm	mm
19	29.5	-29.5	0.413	-0.413
18	30.5	-30.5	0.427	-0.427
17	30.5	-30.5	0.427	-0.427
16	31	-31	0.434	-0.434
15	40	-40	0.56	-0.56
14	42.5	-42.5	0.595	-0.595
13	48	-48	0.672	-0.672
12	53.5	-53.5	0.749	-0.749
11	54.5	-54.5	0.763	-0.763
10	61	-61	0.854	-0.854
9	61.5	-61.5	0.861	-0.861
8	71.5	-71.5	1.001	-1.001
7	70	-70	0.98	-0.98
6	73	-73	1.022	-1.022
5	70.5	-70.5	0.987	-0.987
4	64.5	-64.5	0.903	-0.903
3	55	-55	0.77	-0.77
2	40.5	-40.5	0.567	-0.567
1	42.5	-42.5	0.595	-0.595
0	0	0	0	0

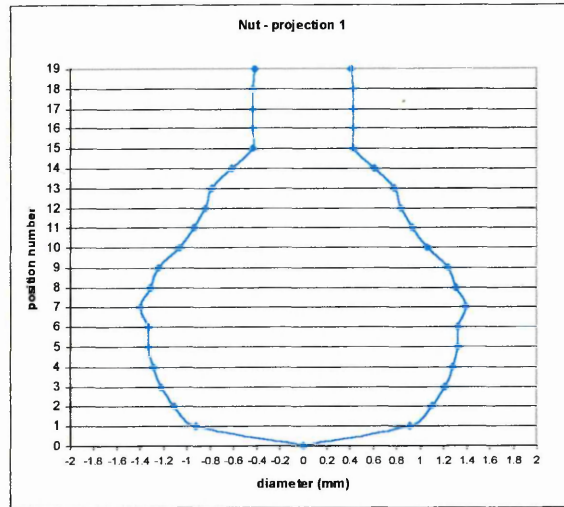


Figure 6.20. Diameter distributions of the irregular shaped nut (projection 1)

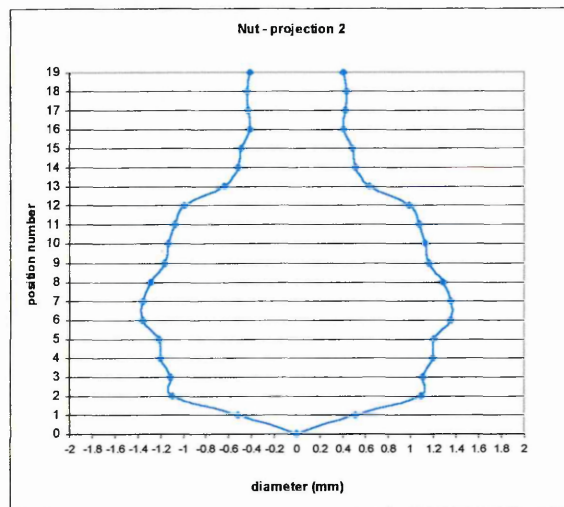


Figure 6.21. Diameter distributions of the irregular shaped nut (projection 2)

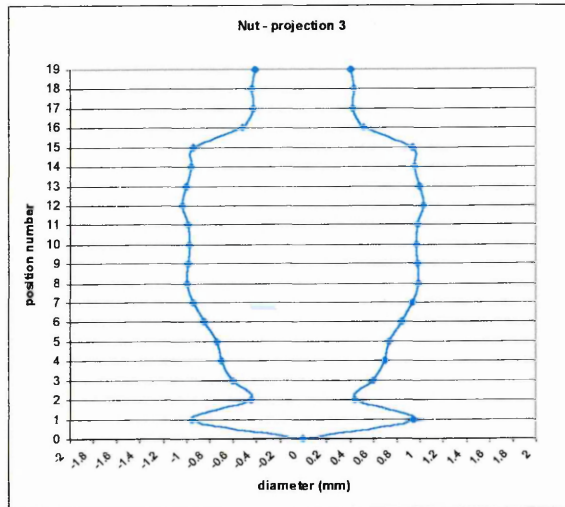


Figure 6.22. Diameter distributions of the irregular shaped nut (projection 3)

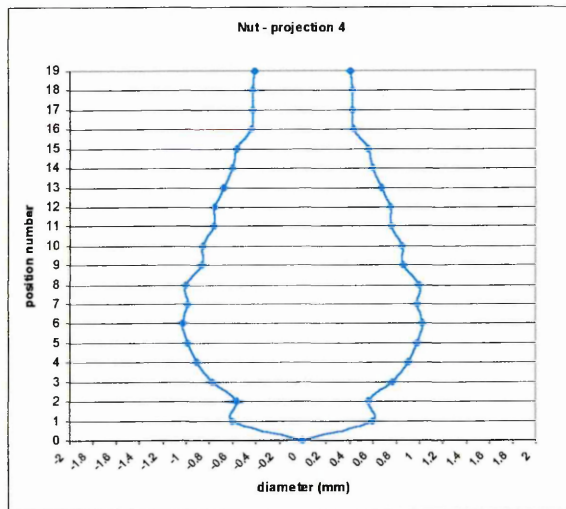


Figure 6.23. Diameter distributions of the irregular shaped nut (projection 4)

6.3.1 The tomographic images of the nut

Images of the nut, for each position, are obtained through the reconstruction process using both the transpose and pseudo inverse sensitivity matrices. All the reconstructed images of the nut are based on averaging eight voltages on the output measurements.

Figures 6.24 to 6.25 show the reconstructed images of the nut using the transpose (position 19 down to position 0), whilst Figures 6.26 to 6.27 show the reconstructed images of the nut using the pseudo inverse.

These results are discussed in Section 6.4.

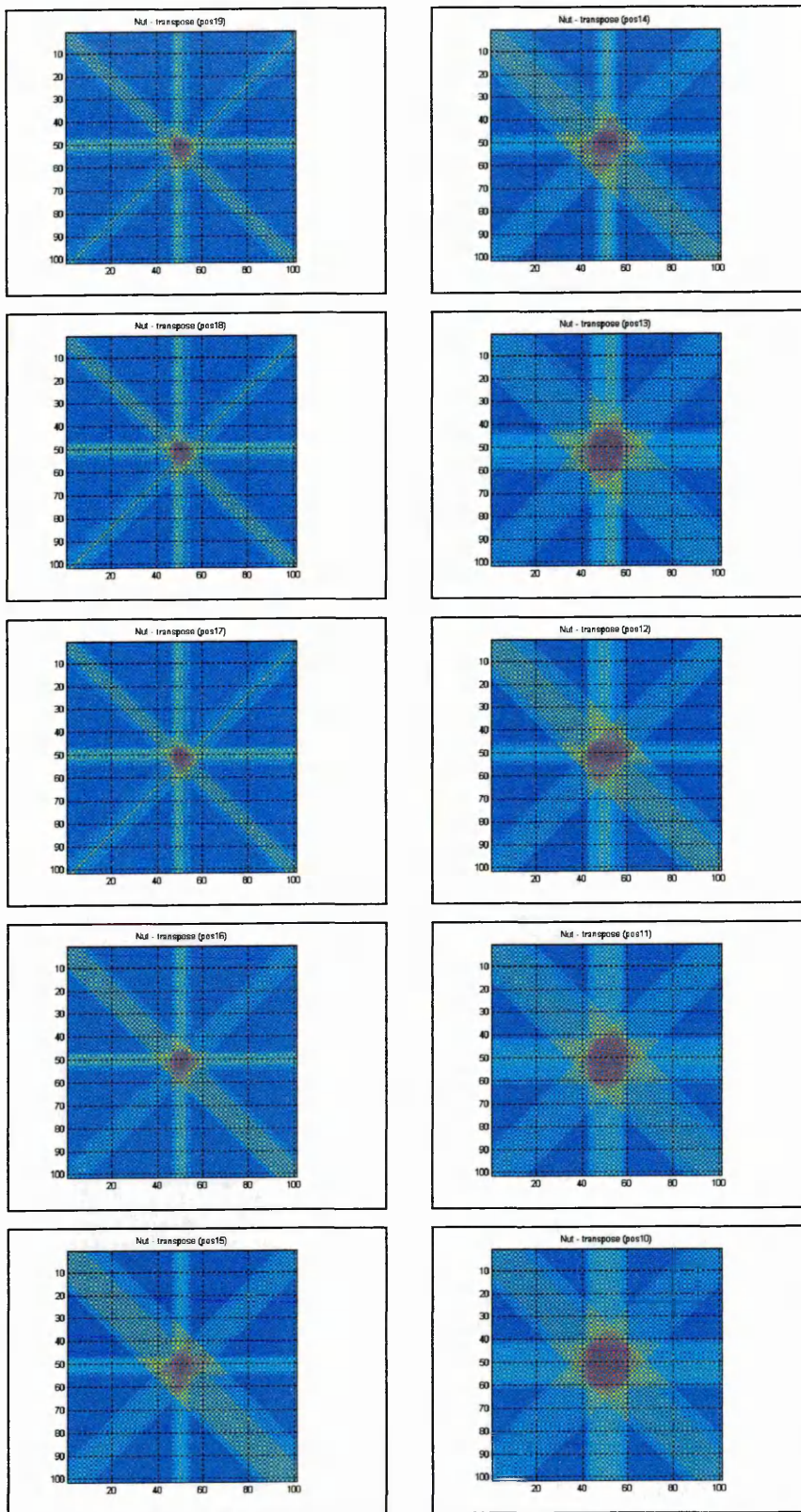


Figure 6.24. Images of the nut (transpose) – position 19 – 10.

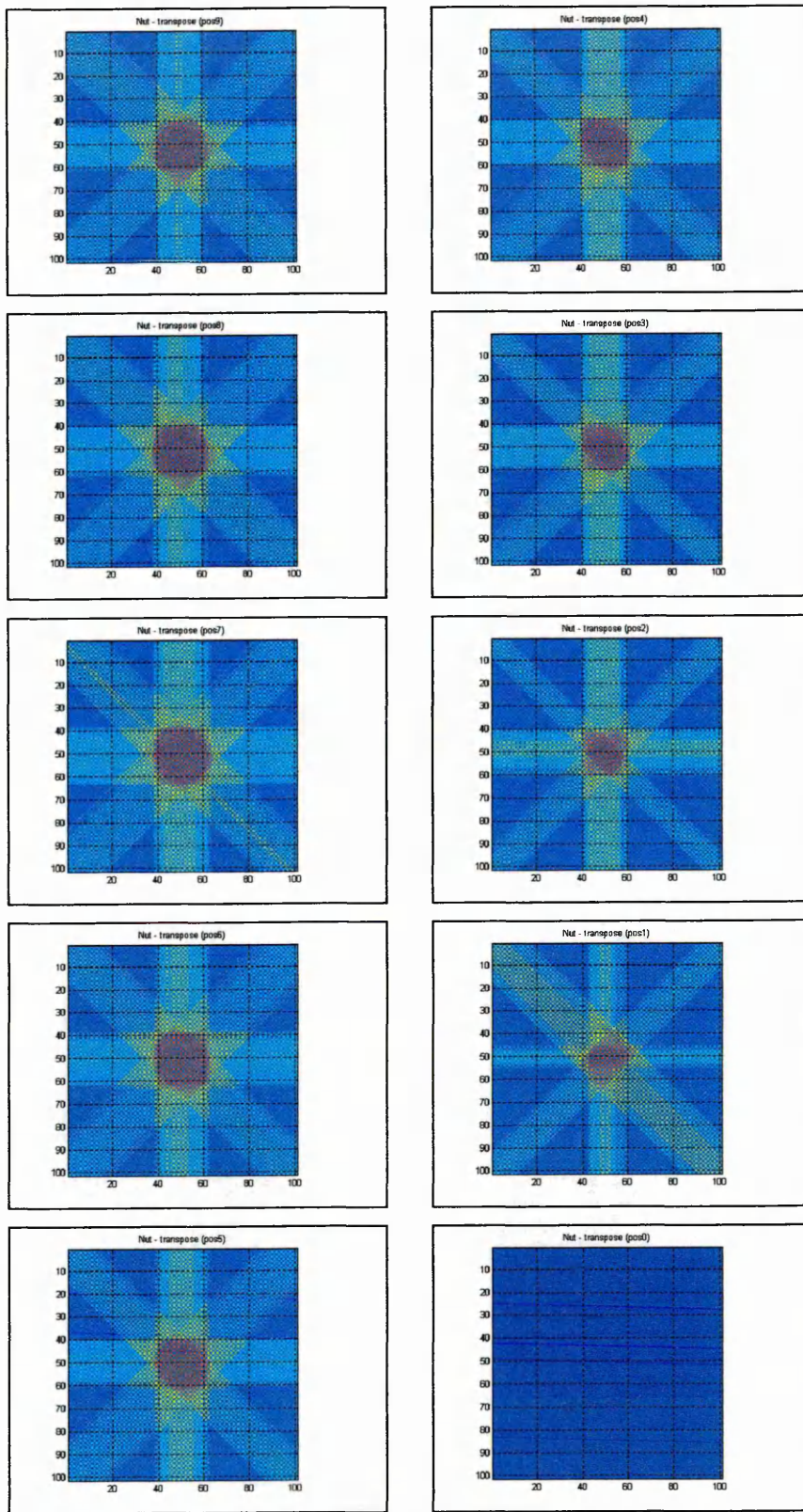


Figure 6.25. Images of the nut (transpose) – position 9 – 0.

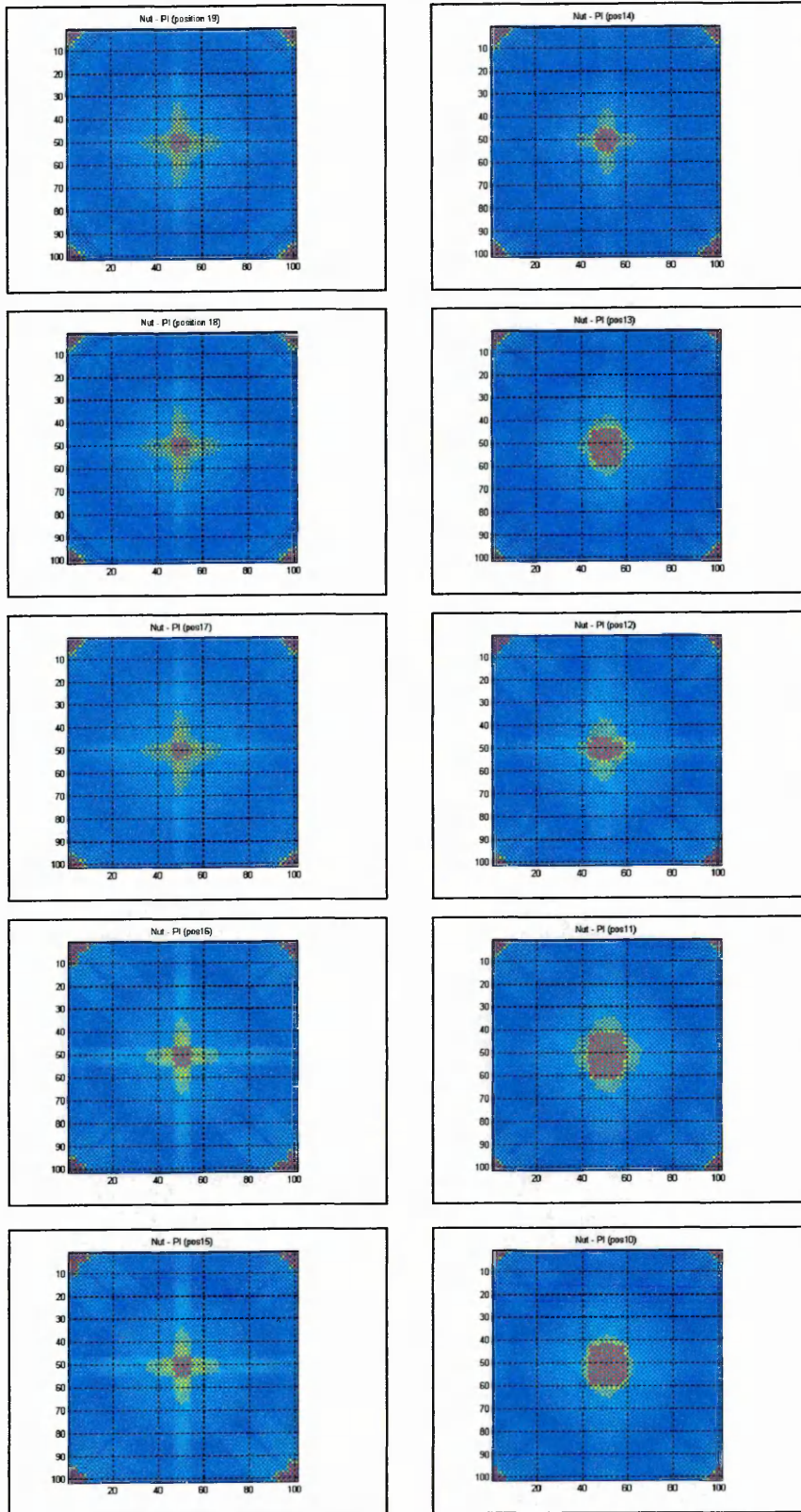


Figure 6.26. Images of the nut (pseudoinverse) – position 19 – 10.

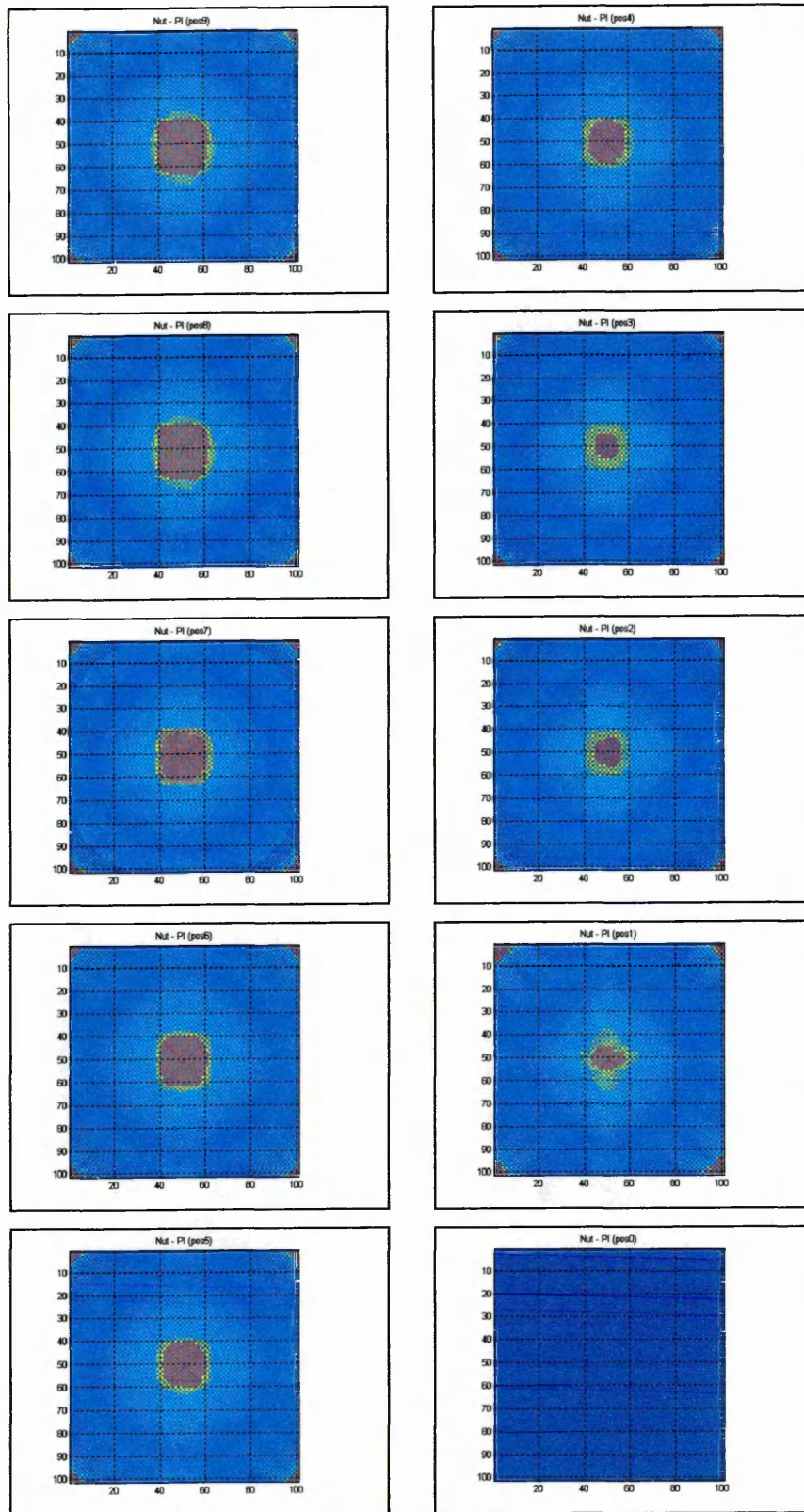


Figure 6.27. Images of the nut (pseudoinverse) – position 9 – 0.

6.3.2 Filtered tomographic images of the nut

Filtering (Section 6.2.2) is applied to the images obtained using the pseudo inverse matrix. The filtered images of the nut use a threshold optical attenuation coefficient value of 25 mm^{-1} . Any value of the pixel greater than the threshold value is retained, whilst the rest of the values are set to zero. The filtering process reduces the smearing effects on the reconstructed images, hence producing more sharply defined images of the particle.

The contoured slice plane of the nut at every position is shown in Figure 6.28. These results are discussed in Section 6.4.

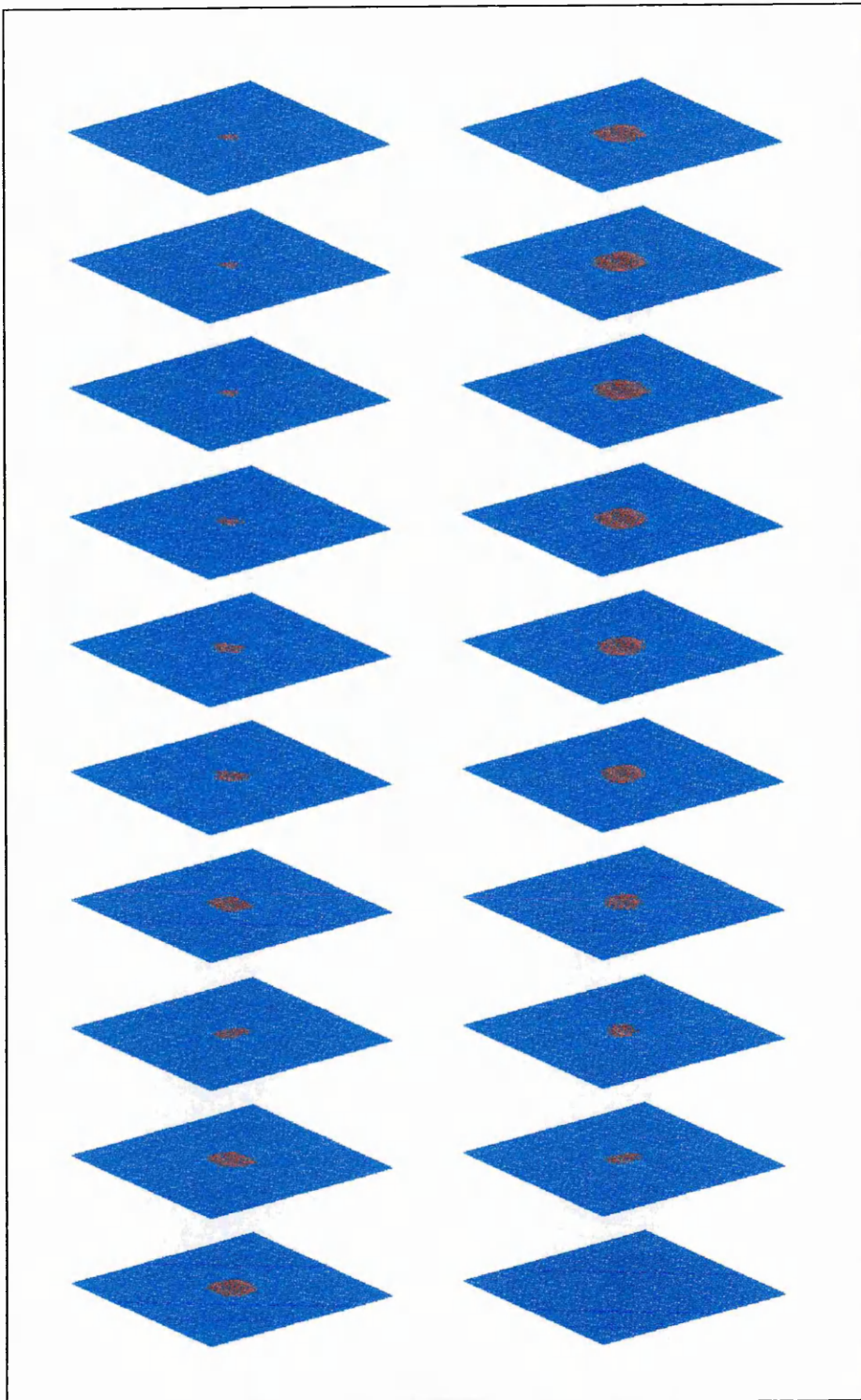


Figure 6.28. Contoured slice planes of the nut for all positions.

6.4 Analysis of the results on tomographic reconstructed images

The CCD-based optical tomography system is capable of measuring particle size to within ± 1 pixel (± 0.014 mm). The tomographically reconstructed images, based on the measurements of the particle of interest have been processed successfully by means of both the transpose and pseudo inverse sensitivity matrices.

The image reconstruction process for the CCD-based optical tomography system is possible using novel arrangements of the pixels. The combination of octagonal-square shaped pixels enables all four projections to pass through all cells normal to the cell walls. Although some of the pixels experience two projections, whilst adjacent pixels experience four projections, the overall reconstructed images are better than with two projections i.e. *aliasing* effects are reduced. In addition, the tomographically reconstructed images are high-resolution images with image pixel sizes down to 14 micron by 14 micron.

The main drawbacks of the image reconstruction process for the CCD-based optical tomography system are the processing time and the required computational memory. The processing time is one hour for the reconstruction process based on the pseudoinverse (for 101 pixels by 101 pixels output image). More memory is required for the image reconstruction for images in excess of 101x101 (Chapter 5).

The actual reconstructed images of the system are limited to 1.414 mm by 1.414 mm (101 pixels by 101 pixels). Therefore, the measurements for a larger particle need to be pre-processed by grouping two or more measurement pixels together and averaging them prior to the reconstruction process in order to visualize the whole image of the particle. Examples can be seen of this approach in the reconstructed images of the 3 mm bead and the irregular shaped nut.

6.4.1 Without filtering

Filtering an image in this case is defined as thresholding the image at a specific value. It can be seen that the reconstructed images, without any filtering process, have smearing effects. This effect is common in linear backprojection images. The images are found to have intermediate values of linear attenuation coefficients, neither the linear attenuation coefficient of the particle nor its surroundings (water or air). The value of the pixels in

the reconstructed images represents the linear attenuation coefficients of the medium. However, the linear coefficient of the particle (i.e. solid) has been quantified by the computation at approximately 25 mm^{-1} after the process, whereas it should be infinity, but it has a distinctively high value compared to the linear attenuation coefficient of water (0.00287 mm^{-1}) or air (0.0014 mm^{-1}).

6.4.2 With filtering

The contrast of the tomographically reconstructed images is improved by the filtering process. The reconstructed images are filtered at a threshold value of 25 mm^{-1} . The value of 25 mm^{-1} is chosen because this image looked the best compared to other images obtained with different threshold values, in terms of retaining the information about the particle and reducing the smearing effects. In this case, any value greater than 25 mm^{-1} is retained, whilst all lower values are made equal to optical attenuation of water. The results show that the filtered images are cleaner and represent better the actual object. For example the image of the bead in air, where the linear attenuation coefficient of the particle has a distinctively higher value compared to the linear attenuation coefficient of air (0.00142 mm^{-1}).

The filtering process is only performed on the image reconstructed by means of the pseudo inverse sensitivity matrix, because the image has quantitative information about the linear attenuation coefficients, which are of the correct order of magnitude for transparent materials. The reconstructed image obtained using the transpose has qualitative information about the particle with no information relating to the linear attenuation coefficient.

From Section 3.3 the 25% illumination level (75% on the shadow image of the CCD linear sensor) should coincide with the edge of the object. Therefore using a threshold value of 75% of the difference between the maximum voltage and the mean minimum voltage is approximate.

6.5 Discussions

The optical tomography system based on CCD linear image sensor is capable of measuring particle diameter within 1 pixel i.e. 0.014 mm, which is relatively small. The readings of all four projections are also consistent. However, the diffraction effect is less than calculated as the CCD linear image sensors operated slightly above saturation level.

The reconstructed images based on the transpose and pseudo inverse matrices are able to display the particle, where the filtering process reduces smearing effects.

CHAPTER 7

CONCLUSIONS AND RECOMMENDATIONS FOR FUTURE WORK

7.1 Conclusions

Particle size in many chemical processes is of great importance. Most of the techniques used in measuring particle size are based on sampling measurements, which may not represent the actual process flow. The optical tomographic instrumentation system based on the CCD linear image sensor is capable of performing particle size measurement over the full cross section of the 30 mm diameter pipe.

The specifications of the CCD-based optical tomographic system are described in Section 6.1 and can be summarised as follows:

Accuracy: $\pm 1.46\%$ of full scale

Absolute accuracy: ± 0.0085 mm (0.6 pixel)

Repeatability: ± 0.017 mm (1.25 pixel)

Consistency in measurements (4 projections): 0.013 mm ± 0.0034 standard deviation

Range of particle sizes: 0.18 mm to 11 mm

Image reconstructions of the measured particles based on solving the inverse problem using both the transpose and pseudo inverse matrices are shown in Chapter 5. The novel arrangement of the pixels, where the octagon-shaped pixel is coupled with a square-shaped pixel is used to model the forward problem (Section 5.2). It provides a useful matrix for the image reconstruction process. The unique pixel-arrangement ensures normal transmission through all the cells for all four projections and permits a reasonable approximation to a mathematical model of inverse problem.

The specific conclusions of the research objectives are highlighted in the next section.

7.2 Research objectives

The aim and the main objectives of this research as outlined in Section 1.3 have been met. The specific conclusions arising from the research objectives are as follows.

1. The use of a CCD linear image sensor in particle size measurement.

The CCD linear image sensor is very sensitive to light. It is also capable of producing a high resolution output based on the size and number of pixels - 2048 pixels with a size of 0.014 mm by 0.014 mm (Section 4.2.2). Therefore, the CCD linear image sensor is feasible for use in particle sizing. The CCD linear image sensor is capable of scanning a line of an object.

The linear image sensor is relatively low cost (approximately £7) and produces a high definition, line scan which is readily transferred to a computer. The CCD linear image sensor ILX551A is a 22-pin DIP interline image scanner with a built-in timing generator and clock-drivers to ensure direct drive at 5V logic for easy use.

2. Modelling of the system.

Mathematical modelling is important in simulating the actual process. Models of the system are described in Chapter 3, and look at the effects due to particles (Section 3.2), light source (Section 3.3), diffraction (Section 3.4), and scan rate (Section 3.5).

Related mathematical models help to predict the expected outputs of the system in order to understand errors and limitations of the system.

3. Design a light projection system based on the models in Objective 2.

The light projection system or 'raybox' is described in detail in Section 4.2.1. The design of the light projector is important, as it is a major component in the overall design. It is monochromatic and fairly well collimated (Section 3.3b). These qualities minimise measurement errors which would exist if the source was white light or not well collimated (Section 3.3a).

4. Design four CCD linear image sensors that will be configured in four projections around the pipe.

The sensor-detection unit of the system is configured in an octagonal measurement section of the flow pipe, as described in Chapter 4. The arrangement of the four similar projection systems is equal in terms of the distance of the 'raybox' to the CCD linear image sensor. A complete measurement system based on Objectives 1 to 5 has been built and tested to determine its limitations (Chapter 6).

5. Calibrate the four projections instrumentation system for measuring particle sizes using known diameters between 0.4 mm and 10.5 mm.

The results are shown in Section 6.1.1 where different sizes of standard objects are measured in a single projection, ranging from 0.400 mm to 10.5 mm. The errors found in the measurement vary from 0.0008 mm to 0.0085 mm (0.1 pixel to 0.6 pixel), with the maximum percentage of error of 1.4%. Ensuring the light is better collimated and has uniform intensities along the CCD linear sensor could reduce the errors.

6. Design, implement and test a linear back projection algorithm based on four projections to produce tomographic images. Two methods of solving the inverse problem based on transpose and pseudo inverse sensitivity matrices are used and compared.

The background of the tomographic image reconstruction is discussed in detail in Chapter 5, where two methods of solving the inverse problem are used – transpose and pseudo inverse matrices. The reconstructed images of the measured particles are shown in Chapter 6. The overall conclusion is the tomographic reconstructed image based on the transpose matrix has qualitative information whilst the reconstructed image based on the pseudo inverse matrix has quantitative information. Moreover, the images obtained using the pseudo inverse transform have less smearing than the transpose transform.

7. Test the four projections instrumentation system for measuring a sphere particle and an irregular shaped particle.

The calibrated optical tomography system is tested using a spherical bead and an irregular shaped nut (Sections 6.2 and 6.3). The system is capable of measuring the diameter of the sphere, and the minimum and the maximum diameters of the nut. The measurements of the particle are confirmed by the tomographic reconstructed images of the bead and the nut.

7.3 Suggestions for future work

The project has achieved its main objective - measuring the size of particles by means of CCD-based optical tomography system. However, the instrumentation and the image reconstruction processing system can be optimised or upgraded to a better system in future. Recommendations for future work are divided into two sections. The first section aims to improve the existing system. The second section suggests further applications to which the system may be applied.

7.3.1 Improvements of the existing system

1. The lighting system

a) Use of a high power laser.

The existing system uses low power laser diodes and the laser diode needs to be illuminated for 6 milliseconds in a single projection system. Using a higher power of laser will reduce the illumination time. This will have several advantages - it will improve signal to noise ratios, because CCD devices can leak charge between sensors. This leakage increases with time. Reduced leakage will improve image contrast. A short pulse of illumination is required if the system is used in monitoring dynamic behaviour of the particle, as the system measurement needs to be fast to prevent image blur.

2. The detection or sensing system

a) Use of a CCD area image sensor.

The CCD linear image sensor is capable of scanning only a line of an object compared to the area image sensor, which can capture or scan a specific area of the object depending on the size of the image sensor. A CCD area image sensor has a pixel size as small as 7 micron with a wide selection of image area. Moreover, the CCD area image sensor can capture in colour, which can represent the actual body-colour of the object. A sequence of images will enable particle velocities to be measured.

b) Use of a digital camera with video facilities.

A video camera has interlaced frames. This interlacing requires frame separation before any real analysis can begin. Also at present video cameras are relatively expensive and so are not being considered at present. However, the use of a digital camera with video facilities may enable monitoring and detecting fast-moving particles in the pipe.

The possible advantages of the digital camera over the CCD linear image sensor need to be worked out from its technical specifications, for example to use a known frame rate and cross-correlation of images to determine particle velocity.

The camera would have a complete optical system which may enable larger pipes to be imaged. The pulsed lighting and other features are exactly the same, except that there will be no slit but a circular aperture in the ray box.

3. The flow pipe material

a) Use of an optically flat glass or quartz window

The measurement section should be changed from the perspex material in the existing system to optically flat glass or quartz windows in future. The use of optically flat material would reduce distortion of light coming from the ray box. Physically these materials are more scratch resistant than perspex.

4. Data acquisition system

The data acquisition system should be able to acquire data for a real-time, on-line measurement system, which is more practical in industrial applications. A high computing power should be used in future so that the tomographically reconstructed image can be processed very quickly and in real-time mode.

5. Image reconstruction system

a) The arrangement of model cells

The existing arrangement of the model cells lets the square and the octagonal cells experience two projections and four projections, respectively. However, the views of the two projections at 45° to the horizontal pass through different numbers of cells (Figure 5.1). In future, a different arrangement should be used which enables all views in a projection to pass through the same number of cells (Figure 7.1). This will make areas in the reconstructed image more uniform and hence have the correct values of linear attenuation coefficients, especially in the case of solving the inverse problem using the pseudo inverse matrix.

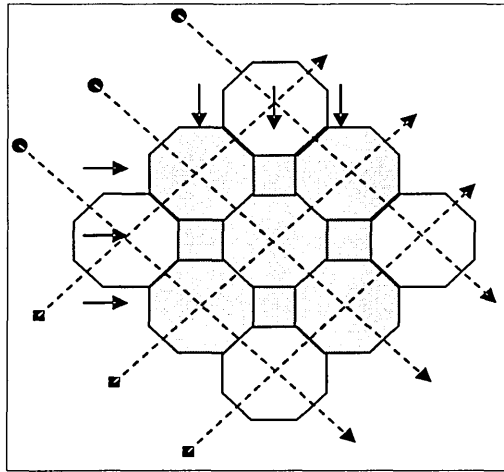


Figure 7.1. Arrangement of model cells.

b) Faster PC

A high computing power PC in terms of its speed and memory capabilities should be used in future, as it is very critical in real-time applications. Larger memory enables the tomographic image reconstruction process over a greater area of the cross-section of the pipe.

7.3.2 Future applications of the system

1. Iterative image reconstruction based on the pseudo inverse solutions.

Iterations on the tomographic reconstructed images are usually performed on the transpose solution due to its simplicity. A similar method should be used on the pseudo inverse solution as the reconstructed image based on the pseudo inverse has quantitative information. The overall result can be compared with other iterative image reconstruction techniques.

2. Investigation of shape or surface roughness of a particle.

The existing system should be upgraded to enable monitoring of particle shape and surface roughness. These two factors are important in particle characterisation. Different switching modes between having the emitters enabled and the receivers enabled may be related to other particle characterisations. All the sensors could be monitored each time a laser is enabled. Particle shape and surface finish (roughness) may be related to scattering.

3. Investigation of the linear attenuation coefficient of unknown particle.

The system should be investigated to determine if with near spherical, translucent particles the linear attenuation coefficient of the particle could be determined based on the model in Chapter 3.

4. Investigation of the dynamic behaviour of a particle.

The existing system should be made more practical for industrial applications by monitoring the dynamic behaviour of a particle. This can be done using cross-correlation techniques, where two CCD linear image sensors are axially spaced on the top and bottom of the measurement section of the flow pipe (Figure 7.2).

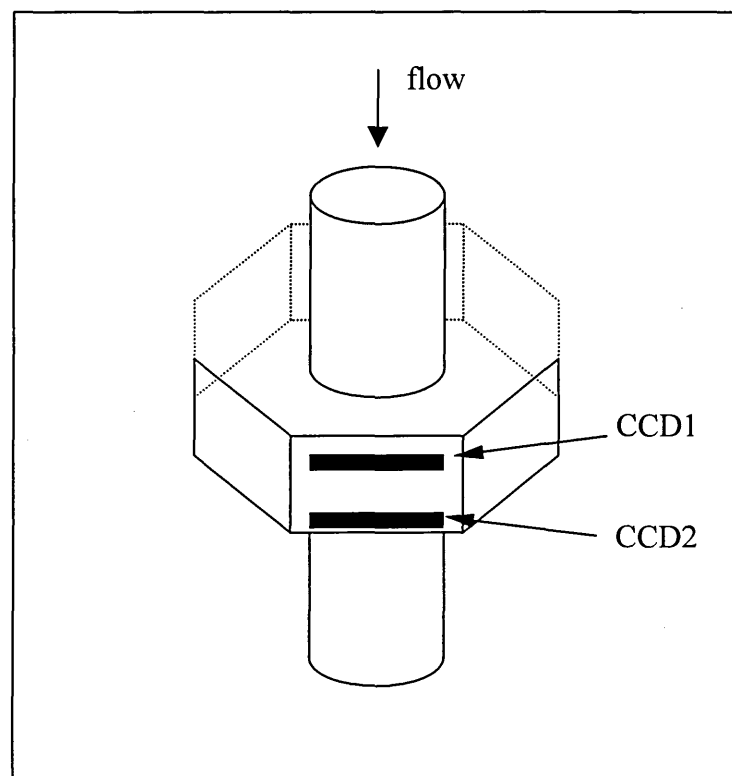


Figure 7.2. Layout for the dynamic measurement.

REFERENCES

Abdul Rahim R. *A tomographic imaging system for pneumatic conveyors using optical fibres*. PhD Thesis. Sheffield Hallam University. 1996.

Allen T. *Particle Size Measurement*. 4th Edition. Chapman and Hall, New York. 1990.

Beck MS and Williams RA. Sensor design and selection. In Scott DM and Williams RA (editors), *Frontiers in Industrial Process Tomography*. New York. 1995.

Beck MS and Williams RA. Process Tomography: a European innovation and its applications. *Meas. Sci. Technol.* Vol 7, pp 215-224. 1996.

Black DL, McQuay MQ, Bonin MP. Laser-based techniques for particle-size measurement: A review of sizing methods and their industrial applications. *Prog. Energy Combust. Sci.* Vol 22, pp 267-306. 1996.

Coufal H. Optical tomography? *Journal of Molecular Structure*. Vol 347, pp 285-292. 1995.

Coulson JM and Richardson JF. *Chemical Engineering Volume 2: Unit operations*. Pergamon Press. 1991.

Daniels AR. *An investigation into the use of dualmodality tomography for the measurement of constituent volumes in multi component flows*. PhD Thesis. 1995.

Dugdale P, Green RG, Hartley AJ, Jackson RG and Landauro J. Characterisation of single bubbles by an optical tomographic system. In Beck MS *et al* (editors), *A Strategy for Industrial Exploitation*. Brite Euram. 1994.

Driscoll WG and Vaughan W. *Handbook of Optics, Optical Society of America*. McGraw Hill, 1978.

Elliot KH and Mayhew CA. The use of commercial CCD cameras as linear detectors in physics undergraduate teaching laboratory. *Eur. J.Phys.* Vol 19, pp 107-117. 1998.

Fischer J, Haasz V and Radil T. Simple device for small dimension measurement using CCD sensor. *12th IMEKO TC4 International Symposium.* 25-27 September 2002. Zagreb, Croatia.

Green RG, Thorn R. Sensor system for lightly loaded pneumatic conveyor. *Powder Technology.* Vol 95, pp 79-92. 1998.

Hecht E. *Optics.* 2nd Edition. Addison-Wesley. 1987.

Herman GT. *Image reconstruction from projections: the fundamentals of computerised tomography.* Academic Press, New York. 1980.

Horbury NM, Abdul Rahim R, Dickin FJ, Green RG, Naylor BD and Pridmore TP. Tomographic imaging of transparent slurries with particle sizing using optical fibres. In Scotts DM and Williams RA, *Frontiers in Industrial Process Tomography.* New York. 1995a.

Horbury NM, Abdul Rahim R, Dickin FJ, Green RG, Naylor BD and Pridmore TP. An investigation into the use of optical fibres to produce on-line particle size information and tomographic images for hydraulic processes. In Beck MS *et al* (editors), *Process Tomography – Implementation for Industrial Processes.* 1995b.

Ibrahim S. *Measurement of gas bubbles in a vertical water column using optical tomography.* PhD Thesis. Sheffield Hallam University. 1999.

Isaksen O and Nordtvedt JE. Capacitance tomography: Reconstruction based on optimisation theory. *ECAPT 1992.* pp 178-189.

Jenkins FA and White HE. *Fundamental of Optics.* 3rd Edition. McGraw-Hill Book Company, Novato-Mexico. 1957.

Kostov Y and Rao G. Low-cost optical instrumentation for biomedical measurements. *Review of Sci. Instruments*. Vol 71, pp4361-4371. 2000.

Lech M, Polednia E, Werszler A. Measurement of solid mean particle size using tomography. *Powder Technology*. Vol11, pp 186-191. 1998.

Leutwyler K. Optical Tomography. *Scientific American*. pp 147-9. 1994.

Longhurst RS. *Geometrical and physical optics*. 2nd Edition. Longman. 1967.

McKee SL, Williams RA and Boxman A. Development of solid-liquid mixing models using tomographic techniques. In Beck MS *et al* (editors), *Process tomography: A strategy for industrial exploitation*. 1994.

McKee SL, Parker DJ, Williams RA. Visualisation of size-dependent segregation in solid-liquid mixers using PET. In Scotts DM and Williams RA (editors), *Frontiers in Industrial Process Tomography*. 1995.

Morikita H, Hishida K and Maeda M. Simultaneous measurement of velocity and equivalent diameter of non-spherical particles. *Particle and Particle System Characterisation: Measurement and Description of Particle Properties and Behaviour in Powders and other Disperse Systems*. Vol 11, pp227-234. 1994.

Morton EJ and Simons SJR. The role of X-ray microtomography in understanding chemical process behaviour. In Beck MS *et al* (editors), *Process tomography: A strategy for industrial exploitation*. 1994.

Peyton AJ, Yu ZZ, Al-Zeibak S *et al*. An overview of electromagnetic inductance tomography: description of three different systems. *Meas. Sci. Technol*. Vol 7. 1996.

Ramli N, Green RG, Abdul Rahim R, Evans K. Fibre optic lens modelling for optical tomography. *Proceedings of 1st World Congress on Industrial Process Tomography*. China. April 1999.

Reinecke N and Mewes D. Resolution enhancement for multi-electrode capacitance sensors. In Beck MS *et al* (editors), *Process tomography: A strategy for industrial exploitation*. 1994.

Salkeld J. *Process tomography for the measurement and analysis of two phase oil based flows*. PhD Thesis. University of Manchester. 1991.

Scott DM. Introduction to process tomography. In Scotts DM and Williams RA (editors), *Frontier in Industrial Process Tomography*. New York. 1995.

Simon SJR. Imaging techniques for fluidised bed systems: a review. In Beck MS *et al* (editors), *Process tomography: A strategy for industrial exploitation*. 1994.

Smith FG and Thomson JH. *Optics*. 2nd Edition. Wiley. 1988.

Snowsill WL. Particle sizing. In Noltingk BE (editor), *Instrumentation Reference Book*. Butterworth-Heinemann. 1995.

Wedberg TC and Stamnes JJ. Recent results in quantitative optical diffraction tomography. In Beck MS *et al* (editors), *Process tomography: Implementation for Industrial Process*. 1995.

West R. In industry, seeing is believing. *Physics World*. Vol 16 No 6, pp 27-30. 2003.

Williams RA, Dyakowski T, Xie CG, Luke SP, Gregory PJ, Edwards RB, Dickin FJ and Gate LF. Industrial measurement and control of particulate processes using electrical tomography. In Beck MS *et al* (editors), *Process tomography: Implementation for Industrial Process*. 1995.

Xie CG, Plaskowski AJ and Beck MS. Eighth electrode capacitance system for two component flow identification. *IEE Proceeding A*. Vol. 136, p173. 1989.

Xie CG, Huang SM, Hoyle BS, Thorn R, Lenn C, Snowden D and Beck MS. Electrical capacitance tomography for flow imaging: system model for development of image

reconstruction algorithms and design of primary sensors. *IEE Proceedings G*. Vol.139 pp89-97. 1992.

Xie CG. Electrical capacitance tomography. *ECAPT93 Conference*. Germany. 1993.

Xie CG. Image reconstruction. In Beck MS *et al* (editors), *Process tomography: Implementation for Industrial Process*. 1995.

Yang WQ, Spink DM, York TA and McCann H. An image-reconstruction algorithm based on Landweber's iteration method for electrical capacitance tomography. *Meas. Sci. Technol.* **10** No 11 (November 1999) pp 1065-1069, 1999.

PUBLICATIONS OF THE RESEARCH

A list of publications produced during the period of this research is as follows:

Idroas M, Green RG and Dutton K. Application of optical tomography in particle sizing. *PREP 2002 Conference*. Exeter, United Kingdom. 2002.

Idroas M, Green RG and Dutton K, Evans K. Application of optical tomography system in particle sizing. *3rd International Conference on Advances in Strategic Technologies*. Kuala Lumpur, Malaysia. 12-14 August 2003.

Idroas M, Green RG, Dutton K and Evans K. Particle size measurement of small diameters by optical tomography. *Engineering and Technology Conference*. Kuching, Sarawak. August, 2003.

Idroas M, Green RG and Dutton K. Tomographic image reconstruction in particle sizing. *MRG Conference*. Manchester. 2003.

APPENDIX A

CALCULATION ON RATIO OF INTENSITY I_4''/I_i

(SECTION 3.2.2)

Considering the effects of light attenuation (due to absorption) and light reflectance on the particle, I_4' obtained from Section 3.2.1 (when there is no particle) is further reduced to I_4'' . The particle, assumed spherical with radius R , has its diameter on the principal axis through the centre of the CCD detection. The light beam along the principal axis strikes the particle normally (Figure A.1) and loses its intensity due to reflection. Beams parallel to the principal axis but not on it will lose more intensity by reflection. A similar operation as in Section 3.2.1 is performed in the calculation of I_4''/I_i .

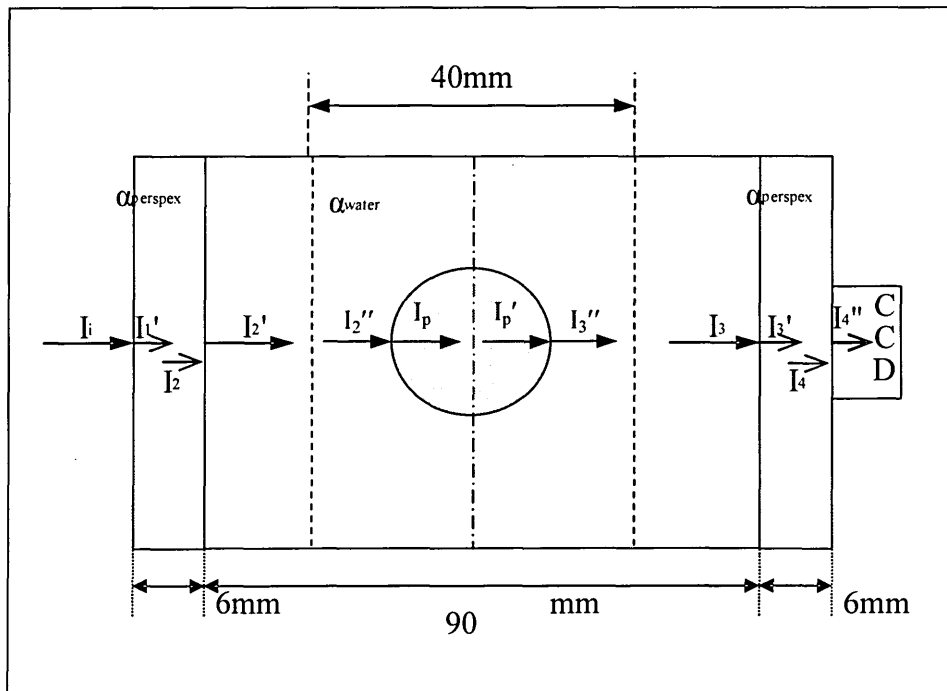


Figure A.1. A light striking a particle in the middle of the pipe.

I_2' obtained from Section 3.2.1 is equal to $0.939I_i$ and further reduced to I_2'' due to attenuation by water.

$$I_2'' = I_2' e^{-(\alpha_{water})(45-R)} = 0.939I_i e^{-(\alpha_{water})(45-R)} \quad (A.1)$$

Then I_p is reduced by reflection at the water/particle interface:

$$I_p = I_2'' - I_{reflection} = I_2'' - \left[I_2'' \left(\frac{n_{particle} - n_{water}}{n_{particle} + n_{water}} \right)^2 \right]$$

$$I_p = I_2'' - \left[I_2'' \left(\frac{1.5 - 1.33}{1.5 + 1.33} \right)^2 \right] = 0.996I_2'' \quad (A.2)$$

Substitute equation (A.1) into equation (A.2):

$$I_p = 0.996I_2'' = (0.996)(0.939)I_i e^{-(\alpha_{water})(45-R)} = 0.935I_i e^{-(\alpha_{water})(45-R)} \quad (A.3)$$

I_p is further being attenuated by the particle.

$$I_p' = I_p e^{-(\alpha_{particle} \times 2R)} = 0.935I_i e^{-(\alpha_{water})(45-R)} e^{-(\alpha_{particle} \times 2R)} \quad (A.4)$$

$$I_p' = 0.935I_i e^{-(\alpha_{water})(45-R) + (\alpha_{particle} \times 2R)} \quad (A.5)$$

I_p' is reduced by reflection at the water/particle interface:

$$I_3'' = I_p' - I_{reflection} = I_p' - \left[I_p' \left(\frac{n_{water} - n_{particle}}{n_{water} + n_{particle}} \right)^2 \right] = 0.996I_p' \quad (A.6)$$

Substituting equation (A.5) into equation (A.6):

$$I_3'' = 0.996I_p' = (0.996)(0.935)I_i e^{-(\alpha_{water})(45-R) + (\alpha_{particle} \times 2R)}$$

$$I_3'' = 0.931I_i e^{-(\alpha_{water})(45-R) + (\alpha_{particle} \times 2R)} \quad (A.7)$$

I_3'' traverses the cell being attenuated by water.

$$I_3 = I_3'' e^{-(\alpha_{water})(45-R)} = 0.931I_i e^{-(\alpha_{water})(45-R)} e^{-(\alpha_{water})(45-R) + (\alpha_{particle} \times 2R)} \quad (A.8)$$

Simplifying equation (A.8):

$$I_3 = 0.931I_i e^{-[\alpha_{water}(90-2R) + (\alpha_{particle} \times 2R)]} = 0.931I_i e^{-[(0.00287 \times 90) - (\alpha_{water} \times 2R) + (\alpha_{particle} \times 2R)]}$$

$$I_3 = 0.931I_i e^{-[(0.00287 \times 90) + 2R(\alpha_{particle} - \alpha_{water})]} = 0.931I_i e^{-[(0.258) + 2R(\alpha_{particle} - \alpha_{water})]}$$

$$I_3 = 0.931I_i e^{-[(0.258)+2R(\alpha_{particle})]} \quad (A.9)$$

I_3 is further reduced by the reflection at the water/perspex interface:

$$I_3' = I_3 - I_{reflection} = I_3 - \left[I_3 \left(\frac{n_{perspex} - n_{water}}{n_{perspex} + n_{water}} \right)^2 \right] = 0.996I_3 \quad (A.10)$$

Substitute equation (A.9) into equation (A.10):

$$I_3' = 0.996I_3 = (0.996)(0.931)I_i e^{-(0.258+2R\alpha_{particle})} = 0.927I_i e^{-(0.258+2R\alpha_{particle})} \quad (A.11)$$

I_3' is then attenuated by the perspex.

$$I_4 = I_3' e^{-[\alpha_{perspex}(6mm)]} = 0.927I_i e^{-(0.003 \times 6)} e^{-(0.258+2R\alpha_{particle})} = 0.927I_i e^{-(0.27+2R\alpha_{particle})} \quad (A.12)$$

I_4'' is incident on the CCD linear image sensor after I_4 is reduced due to reflection at the perspex/air interface.

$$I_4'' = I_4 - I_{reflection} = I_4 - \left[I_4 \left(\frac{n_{air} - n_{perspex}}{n_{air} + n_{perspex}} \right)^2 \right] = 0.96I_4 \quad (A.13)$$

Substitute equation (A.12) into equation (A.13):

$$I_4'' = 0.96I_4 = (0.96)(0.927)I_i e^{-(0.27+2R\alpha_{particle})}$$

$$\boxed{I_4'' = 0.96I_4 = 0.89I_i e^{-(0.27+2R\alpha_{particle})}} \quad (A.14)$$

APPENDIX B

CALCULATION ON RATIO OF INTENSITY I_o'/I_i'

(SECTION 3.2.3)

Figure B.1 shows the measurement section of the system with the dimension of 30 mm i.e. size of the CCD linear image sensor. The output-input ratio of the measurement section is I_o'/I_i' which is used in the image reconstruction process.

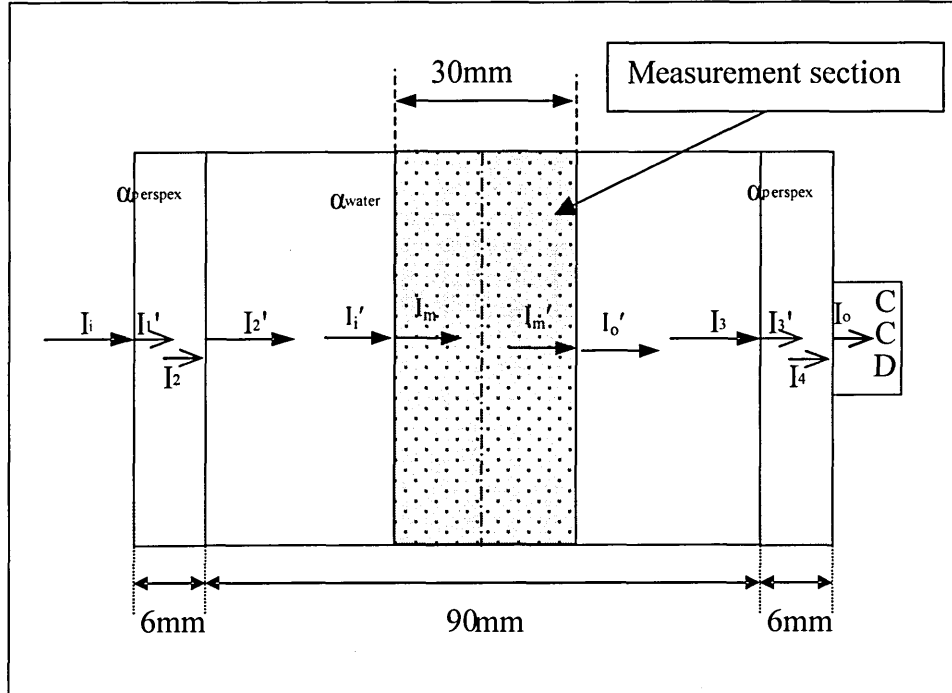


Figure B.1. Layout of the measurement section.

I_2' obtained from Section 3.2.1 is equal to $0.939I_i$ and further reduced to I_i' due to attenuation by water.

$$I_i' = I_2' e^{-(\alpha_{water} \times 30mm)} = 0.939I_i e^{-(0.00287 \times 30)} = 0.861I_i \quad (B.1)$$

$$\therefore \frac{I_i'}{I_i} = 0.861 \quad (B.2)$$

From Equation 3.26 in Section 3.2.1:

$$\boxed{\therefore \frac{I_i}{I_o} = \frac{3}{0.68(4.7 - v)}} \quad (\text{B.3})$$

In Section 3.2.1:

$$\frac{I_o}{I_3} = \frac{I_o}{I_4} \times \frac{I_4}{I_3} \times \frac{I_3'}{I_3} = (0.96)(0.982)(0.996) \quad (\text{B.4})$$

$$\boxed{\therefore \frac{I_o}{I_3} = 0.939} \quad (\text{B.5})$$

From Figure B.1, I_o' traverses the cell being attenuated by water.

$$\boxed{\frac{I_3'}{I_o'} = e^{-(\alpha_{\text{water}} \times 30 \text{ mm})} = e^{-(0.00287 \times 30)} = 0.917} \quad (\text{B.6})$$

Therefore, I_o'/I_i' is equal to:

$$\frac{I_o'}{I_i'} = \frac{I_o'}{I_3'} \times \frac{I_3'}{I_o} \times \frac{I_o}{I_i} \times \frac{I_i}{I_i'} \quad (\text{B.7})$$

$$\frac{I_o'}{I_i'} = \left(\frac{1}{0.917} \right) \left(\frac{1}{0.939} \right) \left(\frac{0.68(4.7 - v)}{3} \right) \left(\frac{1}{0.861} \right)$$

$$\therefore \frac{I_o'}{I_i'} = \frac{1}{0.74} \left[\frac{(0.68)(4.7 - v)}{3} \right] \quad (\text{B.8})$$

Re-arrange Equation B.8:

$$\frac{I_i'}{I_o'} = 0.74 \left[\frac{3}{(0.68)(4.7 - v)} \right] \quad (\text{B.9})$$

Taking natural logarithm on both sides:

$$\boxed{\ln \left[\frac{I_i'}{I_o'} \right] = \ln(0.74) + \ln(3) - \ln[(0.68)(4.7 - v)]} \quad (\text{B.10})$$

APPENDIX C

TRANSPOSE AND PSEUDO INVERSE MATRICES

Transpose matrix

The transpose of a matrix is an operation where the values of the columns of the matrix are replaced by the values of the rows. There is no significant mathematics involved in the transpose operation but it does however make the tomographic image reconstruction based on the backprojection possible. Hence, the reconstructed image using transpose has unphysical pixel values i.e. the values of the pixels do not represent the optical attenuation coefficients.

Figure C.1 shows the image reconstructed using the transpose (R_T) for one-particle in water, with the linear attenuation coefficient of water (α_w) assumed to be 0.00287 mm^{-1} and the linear attenuation coefficient of the particle (α_p) is 10 mm^{-1} .

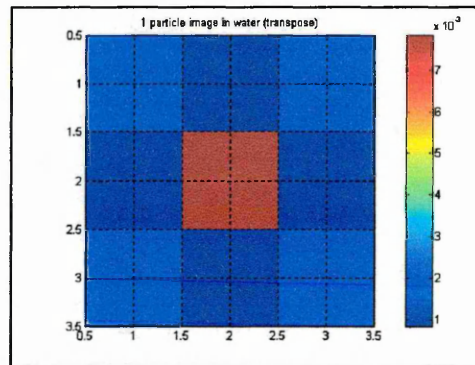


Figure C.1. One-particle in water (transpose).

Values of the matrix, R_T , which represents the reconstructed image pixels using the transpose are as follows:

$$R_T = \begin{bmatrix} 0.0020 & 0.0008 & 0.0020 \\ 0.0008 & 0.0078 & 0.0008 \\ 0.0020 & 0.0008 & 0.0020 \end{bmatrix}$$

Comparing the reconstructed image produced using the transpose with the one using pseudo inverse, the values of the pixels in the reconstructed image using pseudo inverse are much closer to the actual optical attenuation coefficients. This can be seen in the values of R_{PI} compared to R_T . Figure C.2 shows the one particle image in water obtained using the pseudo inverse.

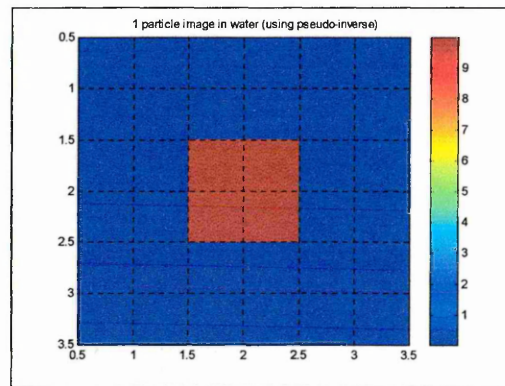


Figure C.2. One particle in water (pseudo inverse).

$$R_{PI} = \begin{bmatrix} 0.00287 & 0.00287 & 0.00287 \\ 0.00287 & 10.000 & 0.00287 \\ 0.00287 & 0.00287 & 0.00287 \end{bmatrix}$$

Pseudo inverse matrix

The inverse of a matrix A exists only if A is square. In this case, if

$$A.x = b \quad (C.1)$$

Therefore, the solution of x is a multiplication of inverse matrix A (A^{-1}) and b.

$$x = A^{-1}.b \quad (C.2)$$

The pseudo inverse of a matrix A or abbreviated as A^+ is actually a generalization of the inverse. It exists for any matrix. The pseudo inverse can be defined as follows.

$$A^+ = \lim_{\delta \rightarrow 0^+} [A^T A + \delta^2 I]^{-1} \approx [A^T A]^{-1} A^T \quad (C.3)$$

where A^T is the transpose of matrix A.

From the mathematics point of view, if the number of equations is equal to the number of unknowns, the solution is *determined*. However, if the number of equations is greater than the number of unknowns, the solution is *overdetermined*. In this case we have more information than what is needed. On the other hand if the number of unknowns is greater than the number of equations, the solution will be *underdetermined*. This is the case involved in the optical tomographic image reconstruction process where the solution obtained using the pseudo inverse minimises the error between the calculated and the real values.

Determined solution (number of equations = number of unknowns)

Suppose there are two equations with two unknowns x_1 and x_2 .

$$3x_1 + 2x_2 = 6 \quad (C.4)$$

$$x_1 + 4x_2 = 9 \quad (C.5)$$

Multiply equation (C.4) with 2: $6x_1 + 4x_2 = 12$ (C.6)

Subtract equation (C.6) to the equation (C.5): $5x_1 = 3$ and hence $x_1 = 0.6$

Substitute the value of x_1 into the equation (C.4) gives the value of $x_2 = 2.1$.

The equations can be solved in a matrix form as follows:

$$[A][x] = [b]$$

The solution: $[x] = [A]^{-1}[b]$ where $[A]^{-1}$ is the inverse matrix of A. The values of the matrix A and matrix b in this case represent the following values.

$$A = \begin{bmatrix} 3 & 2 \\ 1 & 4 \end{bmatrix}, \quad x = \begin{bmatrix} x_1 \\ x_2 \end{bmatrix}, \quad b = \begin{bmatrix} 6 \\ 9 \end{bmatrix}$$

$$x = A^{-1}b = \begin{bmatrix} 3 & 2 \\ 1 & 4 \end{bmatrix}^{-1} \begin{bmatrix} 6 \\ 9 \end{bmatrix} = \begin{bmatrix} 0.6 \\ 2.1 \end{bmatrix} \quad (\text{C.7})$$

The solution is *determined* i.e. there is only one solution for the problem. In terms of optical tomographic image reconstruction, the output image represents the exact values of the optical attenuation coefficient.

Overdetermined solution (number of equations > number of unknowns)

In the case of *overdetermined* solution, there are more equations compared to unknowns. The example of an *overdetermined* solution in tomographic image reconstruction is when the number of projections is greater than the number of pixels in the image. An example of this situation is the image reconstructed from four projections on 3 by 3 cells. However, this phenomenon is very rare in the backprojection image reconstruction.

Underdetermined solution (number of unknowns > number of equations)

In the case of *underdetermined* solution, there are more unknowns compared to the number of equations. This phenomenon is common in the backprojection image reconstruction. The CCD-based optical tomographic image reconstruction has an *underdetermined* solution, where the equations obtained from the four projections are 8192 equations (4 times 2048 pixels) whereas the unknowns are 4,194,304 (2048^2). The problem cannot be solved using the inverse matrix, as the matrix is not square. Thus the pseudo inverse matrix is used as an approximation of the inverse.

APPENDIX D

DIAMETER MEASUREMENTS FOR FOUR PROJECTIONS

(400 micron, 2 mm, 3.7 mm and 10.5 mm)

Table 6.2. Ten measurements of a 400-micron particle in water.

400micron	1	2	3	4	5	6	7	8	9	10	AVG	SD	ERROR
P1 (pix)	28	29	28	28	30	28	30	28	28	30	28.7	0.95	0.5
P1 (mm)	0.392	0.406	0.392	0.392	0.420	0.392	0.420	0.392	0.392	0.420	0.402	0.013	0.007
P2 (pix)	28	26	27	26	28	28	28	28	28	28	27.5	0.85	0.7
P2 (mm)	0.392	0.364	0.378	0.364	0.392	0.392	0.392	0.392	0.392	0.392	0.385	0.012	0.010
P3 (pix)	30	30	30	28	28	30	30	28	30	31	29.5	1.08	1.3
P3 (mm)	0.420	0.420	0.420	0.392	0.392	0.420	0.420	0.392	0.420	0.434	0.413	0.015	0.018
P4 (pix)	29	29	30	28	28	28	29	29	29	29	28.8	0.63	0.6
P4 (mm)	0.406	0.406	0.420	0.392	0.392	0.392	0.406	0.406	0.406	0.406	0.403	0.009	0.008

Table 6.3. Ten measurements of a 2-mm particle in water.

2-mm	1	2	3	4	5	6	7	8	9	10	AVG	SD	ERROR
P1 (pix)	141	141	140	140	141	141	140	140	140	141	140.5	0.53	2.3
P1 (mm)	1.97	1.97	1.96	1.96	1.97	1.97	1.96	1.96	1.96	1.97	1.967	0.007	0.033
P2 (pix)	142	144	142	142	142	143	142	142	144	144	142.7	0.95	0.1
P2 (mm)	1.99	2.02	1.99	1.99	1.99	2.00	1.99	1.99	2.02	2.02	1.998	0.013	0.002
P3 (pix)	144	141	142	143	142	144	142	142	143	142	142.5	0.97	0.3
P3 (mm)	2.02	1.97	1.99	2.00	1.99	2.02	1.99	1.99	2.00	1.99	1.995	0.014	0.005
P4 (pix)	144	144	143	143	143	143	143	143	143	144	143.3	0.48	0.5
P4 (mm)	2.02	2.02	2.00	2.00	2.00	2.00	2.00	2.00	2.00	2.02	2.006	0.007	0.006

Table 6.4. Ten measurements of a 3.7-mm particle in water.

3.66mm	1	2	3	4	5	6	7	8	9	10	AVG	SD	ERROR
P1 (pix)	262	263	260	261	261	260	263	260	260	260	261.0	1.25	0.40
P1 (mm)	3.67	3.68	3.64	3.65	3.65	3.64	3.68	3.64	3.64	3.64	3.654	0.017	0.01
P2 (pix)	260	261	263	262	263	262	262	261	261	261	261.6	0.97	0.20
P2 (mm)	3.64	3.65	3.68	3.67	3.68	3.67	3.67	3.65	3.65	3.65	3.662	0.014	0.00
P3 (pix)	263	262	261	261	262	261	262	261	263	263	261.9	0.88	0.50
P3 (mm)	3.68	3.67	3.65	3.65	3.67	3.65	3.67	3.65	3.68	3.68	3.667	0.012	0.01
P4 (pix)	263	263	263	263	263	263	263	263	263	261	262.8	0.63	1.40
P4 (mm)	3.68	3.68	3.68	3.68	3.68	3.68	3.68	3.68	3.68	3.65	3.679	0.009	0.02

Table 6.5. Ten measurements of a 10.5-mm particle in water.

10.47-mm	1	2	3	4	5	6	7	8	9	10	AVG	SD	ERROR
P1 (pix)	748	748	748	748	747	748	748	748	748	747	747.8	0.42	0
P1 (mm)	10.47	10.47	10.47	10.47	10.46	10.47	10.47	10.47	10.47	10.46	10.469	0.006	0.001
P2 (pix)	748	748	748	748	748	748	748	750	749	748	748.3	0.67	0.5
P2 (mm)	10.47	10.47	10.47	10.47	10.47	10.47	10.47	10.50	10.49	10.47	10.476	0.009	0.006
P3 (pix)	748	748	750	750	750	748	750	750	748	749	749.1	0.99	1.3
P3 (mm)	10.47	10.47	10.50	10.50	10.50	10.47	10.50	10.50	10.47	10.49	10.487	0.014	0.017
P4 (pix)	746	746	747	749	746	745	745	745	746	746	746.1	1.20	1.7
P4 (mm)	10.44	10.44	10.46	10.49	10.44	10.43	10.43	10.43	10.44	10.44	10.445	0.017	0.025

2048-pixel CCD Linear Sensor (B/W)

Description

The ILX551A is a reduction type CCD linear sensor designed for facsimile, image scanner and OCR use. This sensor reads B4 size documents at a density of 200DPI (Dot Per Inch). A built-in timing generator and clock-drivers ensure direct drive at 5V logic for easy use.

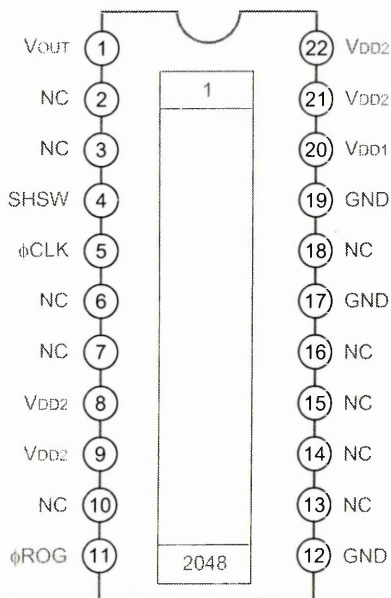
Features

- Number of effective pixels: 2048 pixels
- Pixel size: 14μm × 14μm (14μm pitch)
- Built-in timing generator and clock-drivers
- Ultra low lag
- Maximum clock frequency: 5MHz

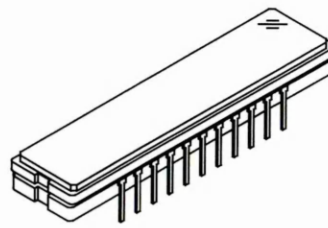
Absolute Maximum Ratings

- Supply voltage V_{DD1} 11 V
- V_{DD2} 6 V
- Operating temperature -10 to +55 °C
- Storage temperature -30 to +80 °C

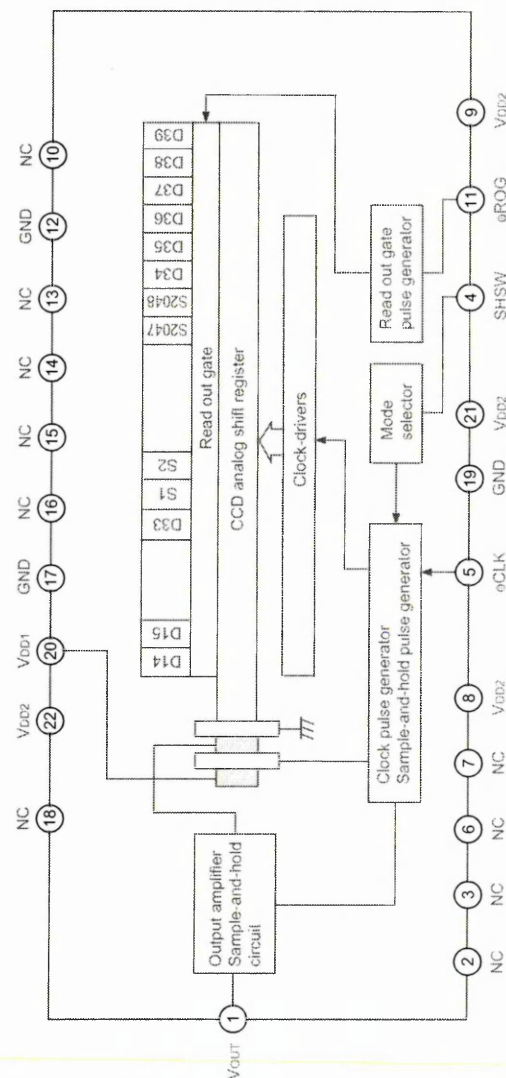
Pin Configuration (Top View)



22 pin DIP (Cer-DIP)



Block Diagram



Sony reserves the right to change products and specifications without prior notice. This information does not convey any license by any implication or otherwise under any patents or other right. Application circuits shown, if any, are typical examples illustrating the operation of the devices. Sony cannot assume responsibility for any problems arising out of the use of these circuits.

Pin Description

Pin No.	Symbol	Description	Pin No.	Symbol	Description
1	V _{OUT}	Signal output	12	GND	GND
2	NC	NC	13	NC	NC
3	NC	NC	14	NC	NC
4	SHSW	Switch { with S/H → GND without S/H → V _{DD2}	15	NC	NC
5	φCLK	Clock pulse	16	NC	NC
6	NC	NC	17	GND	GND
7	NC	NC	18	NC	NC
8	V _{DD2}	5V power supply	19	GND	GND
9	V _{DD2}	5V power supply	20	V _{DD1}	9V power supply
10	NC	NC	21	V _{DD2}	5V power supply
11	φROG	Clock pulse	22	V _{DD2}	5V power supply

Recommended Supply Voltage

Item	Min.	Typ.	Max.	Unit
V _{DD1}	8.5	9.0	9.5	V
V _{DD2}	4.75	5.0	5.25	V

Note) Rules for raising and lowering power supply voltage

To raise power supply voltage, first raise V_{DD1} (9V) and then V_{DD2} (5V).

To lower voltage, first lower V_{DD2} (5V) and then V_{DD1} (9V).

Mode Description

Mode in use	Pin condition
S/H	Pin 4 SHSW
Yes	GND
No	V _{DD2}

Input Capacity of Pins

Item	Symbol	Min.	Typ.	Max.	Unit
Input capacity of φCLK pin	C _{φCLK}	—	10	—	pF
Input capacity of φROG pin	C _{φROG}	—	10	—	pF

Recommended Input Pulse Voltage

Item	Min.	Typ.	Max.	Unit
Input clock high level	4.5	5.0	5.5	V
Input clock low level	0.0	—	0.5	V

Electrooptical Characteristics

(Ta = 25°C, VDD1 = 9V, VDD2 = 5V, Clock frequency = 1MHz, Light source = 3200K, IR cut filter: CM-500S (t = 1.0mm))

Item	Symbol	Min.	Typ.	Max.	Unit	Remarks
Sensitivity	R	30	40	50	V/(lx · s)	Note 1
Sensitivity nonuniformity	PRNU	—	2.0	8.0	%	Note 2
Saturation output voltage	VSAT	1.5	1.8	—	V	—
Dark voltage average	VDRK	—	0.3	2.0	mV	Note 3
Dark signal nonuniformity	DSNU	—	0.5	3.0	mV	Note 3
Image lag	IL	—	0.02	—	%	Note 4
Dynamic range	DR	—	6000	—	—	Note 5
Saturation exposure	SE	—	0.045	—	lx · s	Note 6
9V supply current	IVDD1	—	4.0	8.0	mA	—
5V supply current	IVDD2	—	1.8	5.0	mA	—
Total transfer efficiency	TTE	92.0	97.0	—	%	—
Output impedance	Zo	—	600	—	Ω	—
Offset level	Vos	—	4.0	—	V	Note 7

Notes)

1. For the sensitivity test light is applied with a uniform intensity of illumination.
2. PRNU is defined as indicated below. Ray incidence conditions are the same as for Note 1.

$$PRNU = \frac{(V_{MAX} - V_{MIN})/2}{V_{AVE}} \times 100 [\%]$$

The maximum output is set to VMAX, the minimum output to VMIN and the average output to VAVE.

3. Integration time is 10ms.
4. VOUT = 500mV

$$5. DR = \frac{VSAT}{VDRK}$$

When optical accumulated time is shorter, the dynamic range gets wider because dark voltage is in proportion to optical accumulated time.

$$6. SE = \frac{VSAT}{R}$$

7. Vos is defined as indicated below.

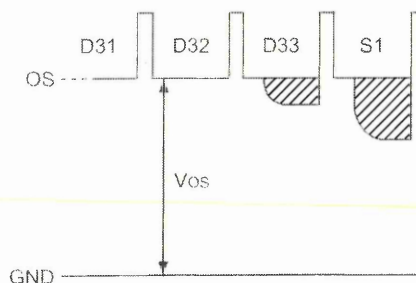


Fig. 1. Clock Timing Diagram (without S/H mode)

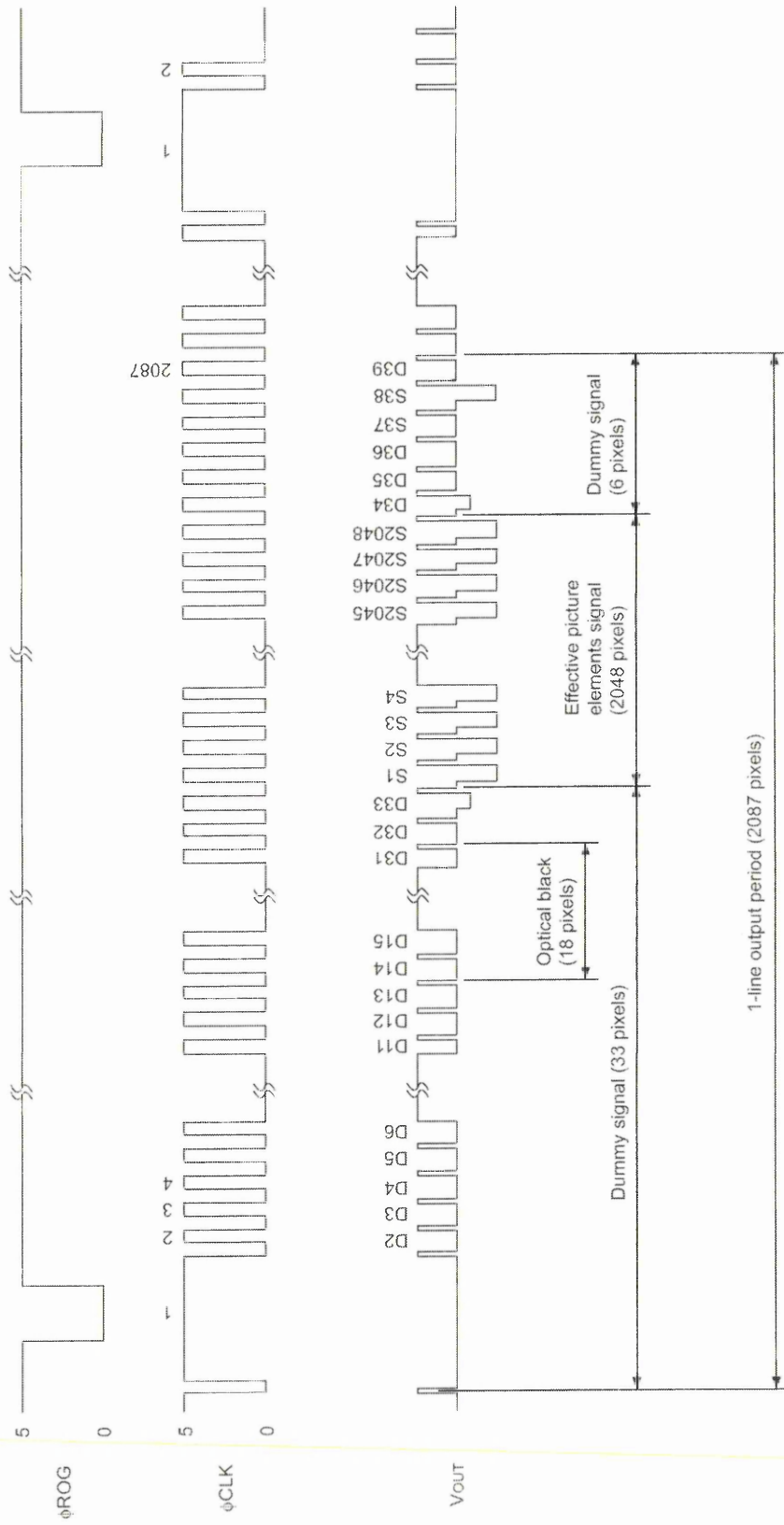
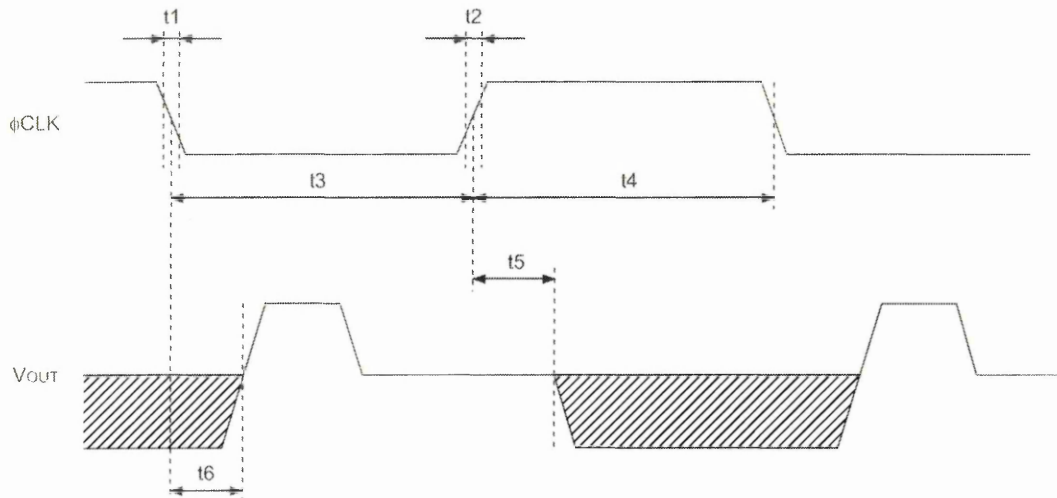


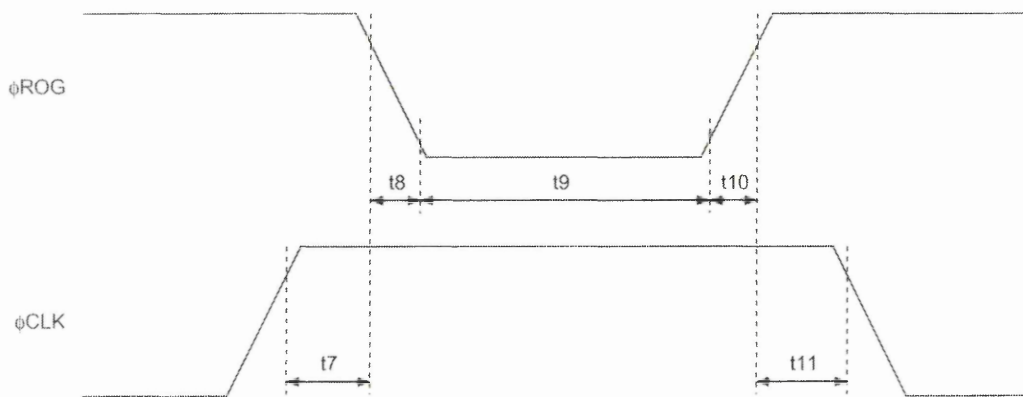
Fig. 2. ϕ CLK, V_{OUT} Timing



Item	Symbol	Min.	Typ.	Max.	Unit
ϕ CLK pulse rise/fall time	t1, t2	0	10	—	ns
ϕ CLK pulse duty ^{*1}	—	40	50	60	%
ϕ CLK – V_{OUT} 1	t5	50	80	110	ns
ϕ CLK – V_{OUT} 2	t6	30	75	120	ns

*1 $100 \times t3 / (t3 + t4)$

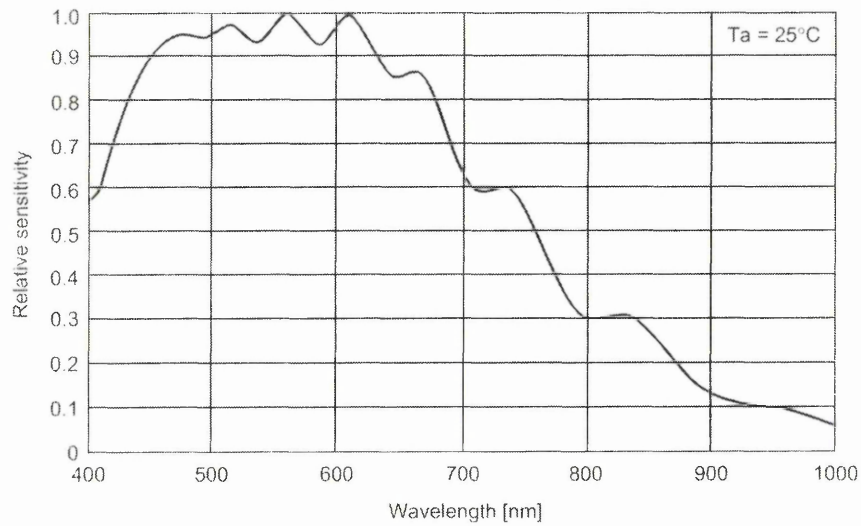
Fig. 3. ϕ ROG, ϕ CLK Timing



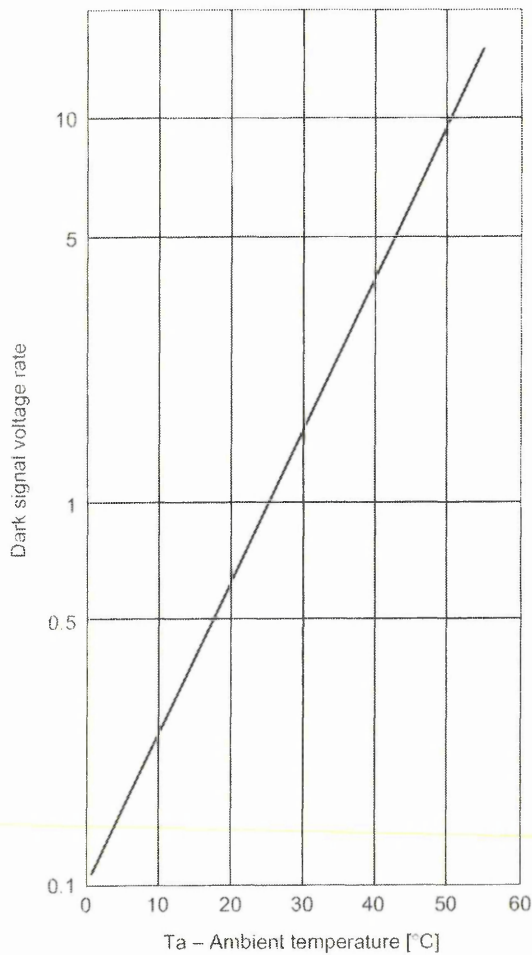
Item	Symbol	Min.	Typ.	Max.	Unit
ϕ ROG, ϕ CLK pulse timing	t7, t11	500	1000	—	ns
ϕ ROG pulse rise/fall time	t8, t10	0	10	—	ns
ϕ ROG pulse period	t9	500	1000	—	ns

Example of Representative Characteristics

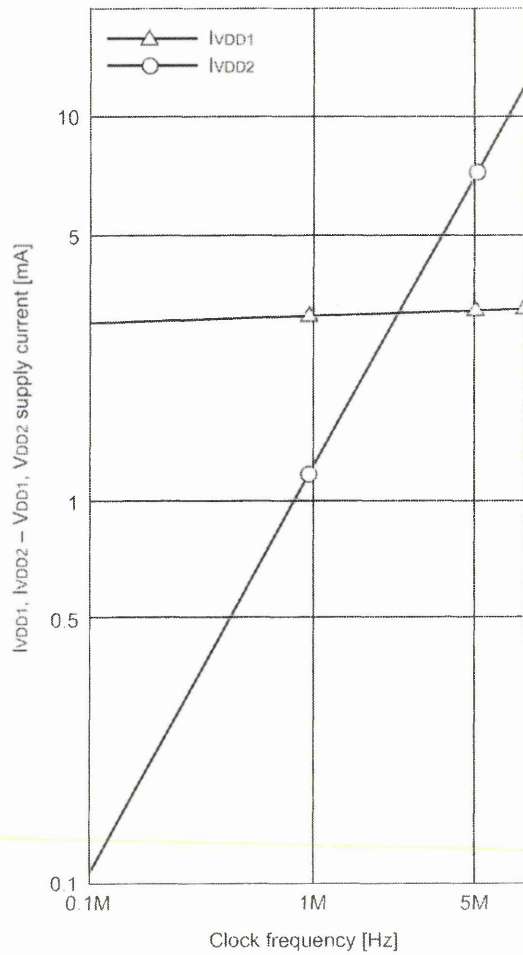
Spectral sensitivity characteristics
(Standard characteristics)



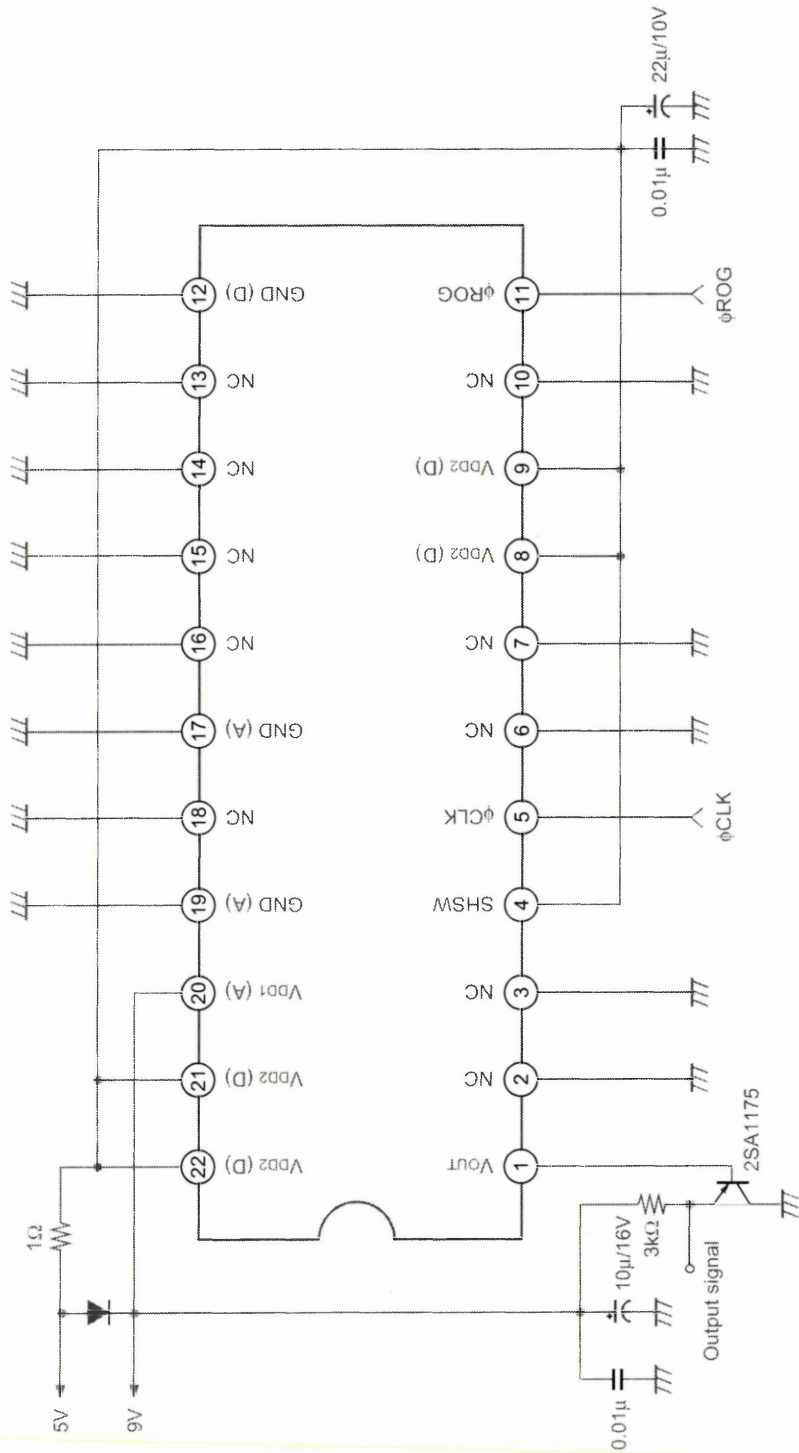
Dark signal voltage rate vs. Ambient temperature
(Standard characteristics)



VDD1, VDD2 supply current vs. Clock frequency
(Standard characteristics)



Application Circuit



Application circuits shown are typical examples illustrating the operation of the devices. Sony cannot assume responsibility for any problems arising out of the use of these circuits or for any infringement of third party patent and other right due to same.

Notes of Handling

1) Static charge prevention

CCD image sensors are easily damaged by static discharge. Before handling be sure to take the following protective measures.

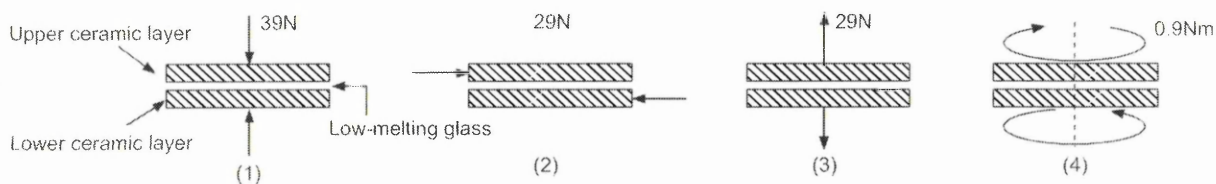
- Either handle bare handed or use non chargeable gloves, clothes or material. Also use conductive shoes.
- When handling directly use an earth band.
- Install a conductive mat on the floor or working table to prevent the generation of static electricity.
- Ionized air is recommended for discharge when handling CCD image sensor.
- For the shipment of mounted substrates, use boxes treated for prevention of static charges.

2) Notes on Handling CCD Cer-DIP Packages

The following points should be observed when handling and installing cer DIP packages.

a) Remain within the following limits when applying static load to the ceramic portion of the package:

- Compressive strength: 39N/surface
(Do not apply load more than 0.7mm inside the outer perimeter of the glass portion.)
- Shearing strength: 29N/surface
- Tensile strength: 29N/surface
- Torsional strength: 0.9Nm



b) In addition, if a load is applied to the entire surface by a hard component, bending stress may be generated and the package may fracture, etc., depending on the flatness of the ceramic portion. Therefore, for installation, either use an elastic load, such as a spring plate, or an adhesive.

c) Be aware that any of the following can cause the glass to crack: because the upper and lower ceramic layers are shielded by low-melting glass,

- Applying repetitive bending stress to the external leads.
- Applying heat to the external leads for an extended period of time with soldering iron.
- Rapid cooling or heating.
- Rapid cooling or impact to a limited portion of the low-melting glass with a small-tipped tool such as tweezers.
- Prying the upper or lower ceramic layers away at a support point of the low-melting glass.

Note that the preceding notes should also be observed when removing a component from a board after it has already been soldered.

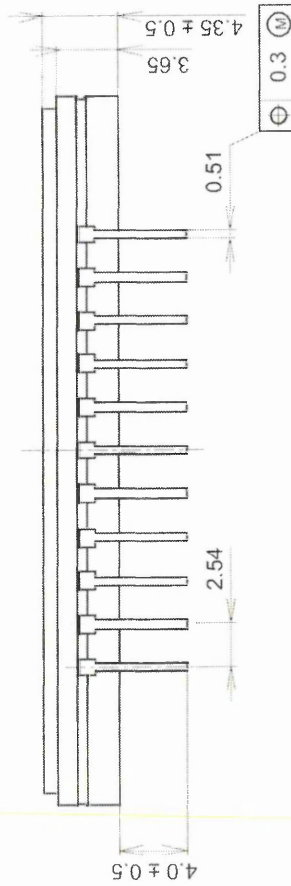
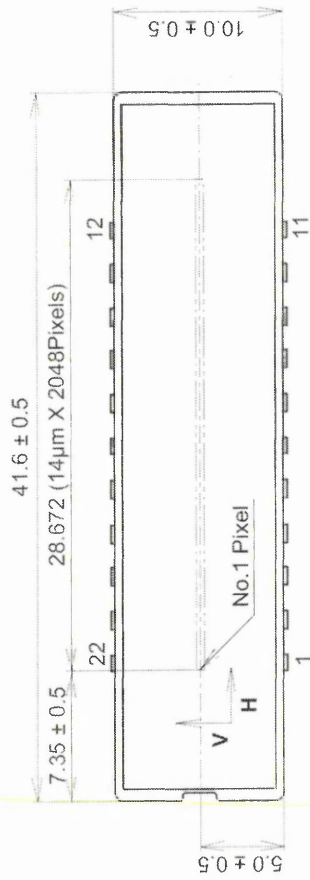
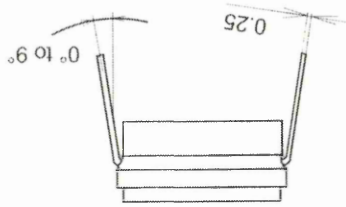
3) Soldering

- Make sure the package temperature does not exceed 80°C.
- Solder dipping in a mounting furnace causes damage to the glass and other defects. Use a grounded 30W soldering iron and solder each pin in less than 2 seconds. For repairs and remount, cool sufficiently.
- To dismount an imaging device, do not use a solder suction equipment. When using an electric desoldering tool, ground the controller. For the control system, use a zero cross type.

- 4) Dust and dirt protection
 - a) Operate in clean environments.
 - b) Do not either touch glass plates by hand or have any object come in contact with glass surfaces. Should dirt stick to a glass surface, blow it off with an air blower. (For dirt stuck through static electricity ionized air is recommended.)
 - c) Clean with a cotton bud and ethyl alcohol if the glass surface is grease stained. Be careful not to scratch the glass.
 - d) Keep in a case to protect from dust and dirt. To prevent dew condensation, preheat or precool when moving to a room with great temperature differences.
- 5) Exposure to high temperatures or humidity will affect the characteristics. Accordingly avoid storage or usage in such conditions.
- 6) CCD image sensors are precise optical equipment that should not be subject to mechanical shocks.

Package Outline Unit: mm

22pin DIP (400mil)



1. The height from the bottom to the sensor surface is 2.45 ± 0.3 mm.
2. The thickness of the cover glass is 0.7mm, and the refractive index is 1.5.

PACKAGE STRUCTURE

PACKAGE MATERIAL	Cer-DIP
LEAD TREATMENT	TIN PLATING
LEAD MATERIAL	42 ALLOY
PACKAGE MASS	5.20g
DRAWING NUMBER	LS-A18-01(E)